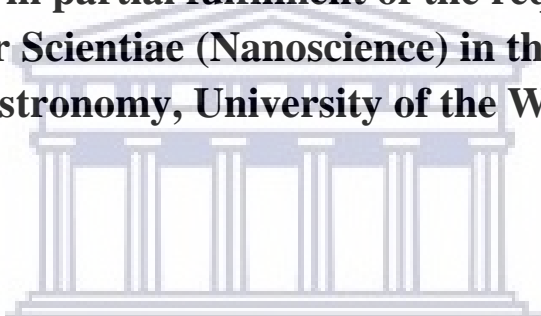


TIN-OXIDE THIN FILMS BY THERMAL OXIDATION

BY

AMY FRANCES JAMES

A thesis submitted in partial fulfilment of the requirement for the degree of Magister Scientiae (Nanoscience) in the Department of Physics and Astronomy, University of the Western Cape

The logo of the University of the Western Cape, featuring a classical building facade with six columns and a pediment, rendered in a light blue color.

Supervisor: Prof CJ Arendse (UWC)

Co-supervisor: Dr L Kotsedi (iThemba LABS)

Co-supervisor: Prof CJ Oliphant (NMISA)

April 2021

I. DEDICATIONS

This thesis is dedicated to my parents Clyde James and Sandra James for their support, guidance, encouragement and unconditional love throughout my studying career.



UNIVERSITY *of the*
WESTERN CAPE

II. KEYWORDS

Photovoltaics

Perovskite

Oxidation

Tin oxide

Semiconductor

Diffusion

Adatoms

Crystal Lattice

Coble Creep

Volmer-Weber growth



UNIVERSITY *of the*
WESTERN CAPE



UNIVERSITY *of the*
WESTERN CAPE

IV. ACKNOWLEDGEMENTS

I would like to express my deepest and heartfelt gratitude's to the following people and organisations without whose assistance and support, the completion of this study would not have been possible.

- First and foremost, I would like to give thanks to my Lord and God, Jesus Christ. It is only through His grace and mercy that I have had the unbounded strength which not only aided me in the completion of this thesis, but groomed me into the person I am today.
- I am incessantly grateful to Prof Christopher Arendse (Department of Physics and Astronomy, UWC) who played a pivotal role at each stage of writing my thesis. It has been a great privilege to work alongside someone with such impressive and impactful expertise and experience. His continuous guidance, inspiration, support and patience is something I will always value, not to mention the general contribution towards every aspect of writing this thesis as well his unending encouragement for growth in my personal career.
- Co – supervisors Prof. C. J. Oliphant from NMISA and Dr. L. Kotsedi from iThemba labs, for the use of their resources and guidance in implementation of characterization techniques.
- UWC department of Physics and Astronomy and Department of Nanoscience including their staff members such as the EMU unit. Especially, Dr. Cummings who was always willing to share his knowledge and expertise on microscopy and this study. In Addition, the secretaries Mrs A. Adams and Mrs V. Jamalie for their continuous assistance.
- To my mentors namely: Siphelo Ngqoloda, Siphesihle Magubane and Norman Bowers who unknowingly has exposed me to horizons which I would never have been able to conquer without his support. I thank you for that. Their perpetual ability to show patience and assistance for preparation of this thesis has given me insight which I will carry with me forever. I want to express my immense gratitude towards them not only for the journey, but for sharing his knowledge and experience with me.

- My colleagues Lionel Fourier, Stephen Klue , Floyd Mabiala, Ian Cupido and Lerato Mohlao for providing friendship, assistance, advisement, moral support and encouragement when needed.
- To my family, for their ceaselessness in encouraging me to persevere in all I do, no matter how tough the road may have gotten. For believing in me when believing in myself wasn't easy. My education is a gift I was given the opportunity to carry with me for days unending.
- To my friend Nigel Simons for his continuous support and patience.
- To University of the Western Cape (UWC, I will forever be grateful for providing the opportunity to reach new horizons in my academic career.
- Armscor and the Department of Science and Technology (DST) for granting myself with financial support throughout the duration of completing this degree.



V. ABSTRACT

Tin dioxide (SnO₂) thin films are a worthy candidate for an electron transport layer (ETL) in perovskite solar cells, due to its suitable energy level, high electron mobility of 240 cm² v⁻¹ s⁻¹, desirable band gap of 3.6 - 4.0 eV, and ultimately proves to be suited for a low temperature thermal oxidation technique for ETL production. A variety of methods are available to prepare SnO₂ thin films such as spin and dip coating and chemical bath deposition. However, the customary solid-state method, which incorporates thermal decomposition and oxidation of a metallic Sn precursor compound in an oxygen abundant atmosphere prevails to be low in cost, is repeatable and allows for large-scale processing.

In this project, we propose to prepare Sn_xO_y thin films by thermal oxidation of a Sn thin film, deposited by ultra-high vacuum thermal evaporation. To induce oxidation, the Sn thin film was annealed in ambient air for 2 hours at temperatures ranging from 200 - 400 °C. The effect of annealing temperature on the evolution of the structural, vibrational and morphological properties of the Sn thin film were investigated. The crystallinity and vibrational properties of the samples were probed by x-ray diffraction and infrared absorption spectroscopy, respectively. The morphological evolution, elemental composition and the optical properties were investigated using high-resolution electron microscopy, Rutherford backscattering spectrometry and UV-VIS spectroscopy, respectively. The oxidation of metallic Sn films lead to a polycrystalline Sn_xO_y structure containing phases of both SnO and SnO₂, with SnO being the dominant crystalline phase. The diffusion flux within the oxidation process was dominated by that of cation Sn⁺² diffusion resulting in oxide growth to mainly form at the

oxide/gas interface. The analytical techniques reveal that the ideal film formed within this study was the film annealed at 400 °C.

By Amy Frances James

April 2021



VI. CONTENTS

I. DEDICATIONS.....	2
II. KEYWORDS.....	3
III. DECLARATION.....	4
IV. ACKNOWLEDGEMENTS.....	5
V. ABSTRACT.....	7
VI. CONTENTS.....	9
VII. LIST OF FIGURES AND TABLES.....	13
CHAPTER 1.....	18
INTRODUCTION.....	18
1.1 The Global Energy Crisis and Renewable Energy.....	18
1.2 Photovoltaic Cells.....	24
1.2.1 Working Principle.....	25
1.2.2 Photovoltaic Solar Cell Classes.....	29
1.2.2.1 First Generation Solar Cells.....	29
1.2.2.2 Second Generation Solar Cells.....	30
1.2.2.3 Third Generation Solar Cells.....	30
1.3 Perovskite Solar Cells.....	31
1.3.1 Perovskite Structure.....	31
1.3.2 Structure of Perovskite Devices.....	34
1.3.3 Instability and Degradation factors in Perovskite solar cells.....	36
1.3.4 Transport layers and their influence on stability.....	36
1.3.4.1 Electron Transport layer.....	37
1.3.4.2 Hole transport layer.....	37
1.3.5 SnO ₂ as an ETL for Perovskite solar cells.....	38
1.3.5.1 Modifications of Perovskite solar cells by the implementation of SnO ₂	39
1.4 Properties of SnO and SnO ₂ materials.....	41
1.4.1 Crystal Properties.....	42
1.4.2 Electronic Properties.....	44
1.4.3 Electrical Properties.....	49
1.4.4 Optical Properties.....	51
1.5 Thermal Oxidation of Metals.....	52

1.5.1	Mechanisms of Oxidation	53
1.5.2	Kinetics of Oxidation in metals.....	56
1.5.2.1	The diffusion rate of an oxide scale	59
1.6	Aim	61
1.7	Outline of thesis	61
	References.....	64
CHAPTER 2		70
EXPERIMENTAL TECHNIQUES		70
2.1	Introduction.....	70
2.2	Sample Preparation	70
2.2.1	Substrate Preparation	70
2.2.2	The Thermal Evaporation Deposition Chamber	71
2.2.3	Deposition of Sn thin films	73
2.2.4	The Single Tube Furnace System	74
2.2.5	Thermal Oxidation of Sn thin films	76
2.3	Analytical Techniques.....	78
2.3.1	Scanning Electron Microscopy	78
2.3.1.1	Introduction.....	78
2.3.1.2	Fundamental Principle and Instrumentation	79
2.3.1.3	Sample Interaction	82
2.3.1.4	Type of Signals	84
2.3.1.4.1	Backscattered Electrons	84
2.3.1.4.2	Secondary Electrons.....	84
2.3.1.4.3	Characteristic X-rays	85
2.3.1.4.4	Auger Electrons	85
2.3.1.4.5	Cathodoluminescence	86
2.3.1.4.6	Transmission of Electrons.....	86
2.3.1.5	Resolution and Abbe's Equation.....	87
2.3.1.6	Aperture	89
2.3.1.7	Depth of Field and Working Distance	90
2.3.1.8	Sample Preparation	91
2.3.1.9	Data Acquisition	92
2.3.2	X-ray Diffraction.....	93
2.3.2.1	Introduction.....	93
2.3.2.1.1	Characteristic X-rays.....	94

2.3.1.2	Geometry of Crystals	96
2.3.1.2.1	Lattice Planes and Directions.....	100
2.3.1.2.2	Interplanar Spacing	101
2.3.1.3	Diffraction from Crystals	102
2.3.1.3.1	The Bragg Law	103
2.3.1.4	The X-ray Diffractometer	104
2.3.1.5	Data Acquisition	106
2.3.3	Fourier Transform Infrared Spectroscopy.....	107
2.3.3.1	Introduction.....	107
2.3.3.2	The Electromagnetic spectrum.....	107
2.3.3.3	Infrared Absorption.....	110
2.3.3.4	Normal Modes of Vibrations	111
2.3.3.4.1	Stretching Vibration.....	114
2.3.3.4.2	Bending Vibrations.....	115
2.3.3.5	IR Analysis.....	117
2.3.3.5.1	Qualitative Analysis.....	117
2.3.3.5.2	Quantitative Analysis.....	118
2.3.3.5.3	Organic Compound Interpretation	118
2.3.3.6	Working Principle.....	119
2.3.3.7	Instrumentation of an FTIR Spectrometer	120
2.3.3.7.1	Michelson Interferometer.....	122
2.3.3.7.2	IR Sources.....	123
2.3.3.7.3	Detectors.....	124
2.3.3.7.4	Fourier – Transformation.....	124
2.3.3.7.5	Computers.....	125
2.3.3.8	Data Acquisition	125
2.3.4	Rutherford Backscattering Spectrometry.....	126
2.3.4.1	Introduction.....	126
2.3.4.2	Theory	126
2.3.4.3	Instrumentation	128
2.3.4.4	Spectral Information	130
2.3.4.5	Quantification.....	131
2.3.4.6	Data Acquisition	132
2.3.5	UV-Visible Spectroscopy	133
2.3.5.1	Introduction.....	133

2.3.5.2	Transmittance and Absorbance	134
2.3.5.3	UV-Vis mechanism.....	135
2.3.5.4	Instrumentation	137
2.3.5.5	Data Acquisition	138
	References.....	139
CHAPTER 3		144
RESULTS AND DISCUSSION		144
3.1	Introduction.....	144
3.2	Experimental Results	146
3.2.1	Morphology.....	146
3.2.2	Phase Transitions	159
3.2.3	Compositional Properties.....	167
3.2.3.1	Fourier Transform Infrared Spectroscopy (FTIR)	167
3.2.3.2	Rutherford Backscattering Spectroscopy	176
3.2.4	Optical Properties.....	181
3.3	Overview and Discussion.....	187
3.4	Conclusion	190
	References.....	192
CHAPTER 4		200
CONCLUSION AND FUTURE WORK		200



VII. LIST OF FIGURES AND TABLES

Figures:

Figure 1.1: Schematic of the world energy balance of various energy sources and their contribution to the global energy demand predictions and alternative energy consumption scenarios [1.7]. 19

Figure 1.2: Amount of solar radiation at the Earth's surface [1.34]. 23

Figure 1.3: Tally of global installations performed globally from 2003 - 2012 [1.8]. 24

Figure 1.4: Formation of the p-n junction within a PSC [1.13]. 28

Figure 1.5: Schematic of how the absorption of light induces a voltage that drives current through a circuit [1.13]. 28

Figure 1.6: Generational classes of available PSC device designs [1.39]. 29

Figure 1.7: (a) Ball and stick model of a basic perovskite crystal structure and (b) illustration of an extended perovskite crystal structure connected via a corner- octahedra [1.26]. 32

Figure 1.8: 2D Structure of an organic-inorganic perovskite structure with a) bilayer and b) a single layer of organic molecules. [1.26]. 34

Figure 1.9: (a) Mesoporous n-i-p structured perovskite device, (b) planar n-i-p structured perovskite device and (c) planar p-i-n structured (inverted planar) perovskite device [1.44]. 35

Figure 1.10: Phase diagram of Sn-O [1.3]. 42

Figure 1.11: Ball and stick model of SnO₂ crystal structure [1.3]. 43

Figure 1.12: Ball and stick model of SnO crystal structure [1.3]. 44

Figure 1.13: DFT calculations for a) density of states (DOS) and b) electronic band structure of SnO₂ [1.37]. 46

Figure 1.14: Photoelectron spectra of the Sn 4d core level chemical shift of 0.5 eV SnO and two SnO₂ samples given by Batzille et al. [1.3, 1.37]. 47

<i>Figure 1.15: DFT calculations for a) density of states (DOS) and b) electronic band structure of SnO provided by Orlandi et al., while c) total density of states given by Batzille et al. illustrating the 4 structures (A, B, C, D) by which SnO can be distinguished from SnO₂ [1.3, 1. 29].</i>	48
<i>Figure 1.16: An oversimplified illustration of the metal, metal oxide and oxygen gas interfaces [1.4].</i>	53
<i>Figure 1.17: Illustration of metal oxide semiconductors [1.31].</i>	56
<i>Figure 1.18: Diagram showing the dominant molar flux for a diffusion controlled oxidation process [1.31].</i>	57
<i>Figure 2.1: Simplified illustration of a thermal evaporation deposition chamber [2.14].</i>	73
<i>Figure 2.2: Single tube furnace situated in a laboratory at the Physics and Astronomy department (UWC).</i>	75
<i>Figure 2.3: Yudian temperature controller with a description of its various settings [2.16].</i>	75
<i>Figure 2.4: Temperature profiles from (a) - (e) for Sn thin films annealed at temperatures of 200, 250, 300, 350 and 400 °C, respectively.</i>	77
<i>Figure 2.5: Full diagram of the SEM instrument [2.33].</i>	80
<i>Figure 2.6: Demonstration of a self-biased thermionic electron gun [2.33].</i>	81
<i>Figure 2.7: Example of the compartments used to form an image in the SEM [2.33].</i>	82
<i>Figure 2.8: Impact of accelerating voltage and atomic number on the primary excitation volume. (a) low atomic number and (b) high atomic number [2.33].</i>	83
<i>Figure 2.9: Interaction with the electron beam with a sample [2.9].</i>	87
<i>Figure 2.10: Primary excitation volume and the signals generated as a result of the sample and electron beam interaction [2.9].</i>	87
<i>Figure 2.11: Schematic depiction of resolution, where (a) airy disks and (b) wavefronts [2.33].</i>	89
<i>Figure 2.12: Illustration of the effects of a small and large aperture presented by (a) and (b) respectively [2.33].</i>	90

<i>Figure 2.13: Representative model of the relationship between the depth of field and working distance. (a) Short working distance with a decreased depth of field. (b) long working distance with an enhanced depth of field [2.33].</i>	91
<i>Figure 2.14: Schematic of the electronic transitions within an atom, where the type of characteristic emissions are illustrated by the arrows [2.2].</i>	95
<i>Figure 2.15: Assortment of crystals and how they are classed [2.31].</i>	96
<i>Figure 2.16: (a) Illustration of a three-point lattice. (b) Schematic representation of a unit cell and its lattice parameters [2.2, 2.31].</i>	97
<i>Figure 2.17: The 14 type of Bravais lattices [2.31].</i>	99
<i>Figure 2.18: Schematic diagram of the diffraction of x-rays by a crystal under conditions of the Bragg law [2.31].</i>	102
<i>Figure 2.19: The fundamental layout of an x-ray diffractometer and para-focusing geometry [2.31].</i>	105
<i>Figure 2.20: The Empyrean XRD system from PANalytical at the National Metrology Institute of South Africa (NMISA) in Pretoria [2.23].</i>	106
<i>Figure 2.21: Schematic display of vibrational and electronic transitions. It should be noted that distance between electronic states have been reduced by a factor of at least 10 in comparison to the distance between the vibrational states. Such that fund: fundamental; harm: overtone; fluo: fluorescence and Phospho: Phosphorescence [2.28].</i>	110
<i>Figure 2.22: Water and carbon dioxide molecules [2.24].</i>	112
<i>Figure 2.23: Symmetric and asymmetric stretching of the CH₃ and NH₂ molecules, where the asymmetric stretch is found at a higher energy than the symmetric stretching bond [2.11].</i>	115
<i>Figure 2.24: The various forms of bending vibrations in the CH₂ group [2.11].</i>	116
<i>Figure 2.25: Main constituents of an FTIR spectrometer [2.24].</i>	121
<i>Figure 2.26: Illustration of the operation if a Thermo Nicolet FTIR Instrument. Produced by Thermo Fisher Scientific (Madison, WI, USA) [2.12].</i>	121
<i>Figure 2.27: Schematic representation of a Michelson interferometer [2.24].</i>	123

<i>Figure 2.28: Conventional layout of an RBS instrument whilst performing an experiment [2.6].....</i>	<i>129</i>
<i>Figure 2.29: Electronic transitions and their relative energy [2.32].</i>	<i>136</i>
<i>Figure 2.30: Simplified illustration of a UV-Visible spectrometer [2.32].</i>	<i>137</i>
<i>Figure 3.1: SEM planar micrographs of the deposited metallic Sn thin films on Si (100) substrates. (a) As-deposited , b) film annealed at 200 °C(c) film annealed at 250 °C, (d) film annealed at 300 °C, (e) film annealed at 350 °C and (f) film annealed at 400 °C.....</i>	<i>148</i>
<i>Figure 3.2: (a) and (c) EDS spot analysis of lighter grains on sample annealed at 300 °C, while (b) and (d) EDS spot analysis of lighter grains on sample annealed at 300 °C. From (e) - (f) Sn_xO_y phase grain size distribution for the thin film deposited on Si (100) and annealed at 300 °C.....</i>	<i>149</i>
<i>Figure 3.3: EDS elemental analysis (right) of selected grains belonging to various Sn_xO_y films (left), where (a) - (f) represent that annealed temperatures of the thin films such that: (a) as-deposited metallic Sn film, (b) 200 °C, (c) 250 °C, (d) 300 °C,(e) 350 °C and (f) 400 °C.....</i>	<i>152</i>
<i>Figure 3.4: Presence of O and Sn atoms within Sn_xO_y grains as a function of the increasing temperature.....</i>	<i>153</i>
<i>Figure 3.5: SEM planar micrographs of the deposited metallic Sn thin films on FTO substrates. (a) As – deposited , b) film annealed at 200 °C(c) film annealed at 250 °C, (d) film annealed at 300 °C, (e) film annealed at 350 °C and (f) film annealed at 400 °C.....</i>	<i>154</i>
<i>Figure 3.6: Sn_xO_y phase grain size distribution for the thin film deposited on FTO and annealed at 250 °C.....</i>	<i>155</i>
<i>Figure 3.7: Thickness of all thin films deposited on Si(100) as a function of annealing temperature.</i>	<i>156</i>
<i>Figure 3.8: The average surface roughness of the thin films deposited on Si (100) as a function of annealing temperature.....</i>	<i>157</i>
<i>Figure 3.9: XRD of the as-deposited thin film and the annealed samples from 200 – 400 °C.....</i>	<i>161</i>
<i>Figure 3.10: (a) Formation of SnO₂ crystallite sizes along the (101) direction residing in 300, 350 and 400 °C annealed Sn_xO_y films. (b) - (d) Arrhenius fit on crystallite sizes for diffusion mechanisms m = 2, 3, and 4.....</i>	<i>166</i>

<i>Figure 3.11: Overall FTIR spectra for as-deposited and annealed Sn_xO_y samples from 200 – 400 °C.</i>	173
<i>Figure 3.12: Overall FTIR spectra for as –deposited and annealed Sn_xO_y samples from 200 - 400 °C.</i>	174
<i>Figure 3.13: Baseline corrected Gaussian fits for samples annealed from 200 - 400 °C.</i>	175
<i>Figure 3.14: RBS spectra for as -deposited and annealed Sn_xO_y samples from 200 - 400 °C.</i>	180
<i>Figure 3.15: Atomic O/Sn ratio and with film thickness evolution as a function of annealing temperature.</i>	181
<i>Figure 3.16: Transmission spectra for Sn thin films annealed 200 - 400 °C.</i>	183
<i>Figure 3.17: (a) - (e) Tauc plots for Sn_xO_y thin films oxidized from 200 – 400 °C, respectively.</i>	186
<i>Table 1.1: General Properties of SnO₂ and SnO [1.29].</i>	41
<i>Table 2.1: Summary of the 7 crystal systems and Bravais lattices [2.31].</i>	99
<i>Table 2.2: The interplanar spacing for the 7 different crystal systems [2.31].</i>	101
<i>Table 2.3: Degrees of freedom for polyatomic molecules [2.24].</i>	112
<i>Table 2.4: Characteristic absorption bands and their corresponding frequencies [2.2].</i>	119
<i>Table 3.1: Sn_xO_y phase lattice parameters present in thin film samples.</i>	162
<i>Table 3.2: SnO₂ crystallite (101) orientated diffraction peak properties.</i>	164
<i>Table 3.3: Arrhenius equation fit parameters for the formation so SnO₂ (100) crystallites.</i>	165
<i>Table 3.4: Vibrational properties of Sn_xO_y films.</i>	172
<i>Table 3.5: Simulated RBS ion beam depth analysis of Sn_xO_y thin film samples.</i>	179

CHAPTER 1

INTRODUCTION

1.1 The Global Energy Crisis and Renewable Energy

Throughout the course of history mankind has always relied on the utilization of energy in some form or manner to aid in their survival. Over the years, even though the dependence on various energy sources may have altered, some patterns have still remained constant as the demand and energy usage increased [1.40].

When comparing the present global energy consumption trends to that of long-term historical ones, it would seem as if the last 150 years have been remarkable especially in the way energy has been used to upscale comfort and the standard of living. According to Jean-Marie Chevalier, “from the 19th century until today, the world’s population has increased by a factor of six, and GDP by a factor of sixty” [1.7]. At present, due to the ever growing population size and usage of electronic gadgets, the demand for energy has triggered a global energy crisis. As a consequence in fulfilling these demands, unsustainable climate change has become more prominent during this period [1.16, 1.28].

Fossils, non-renewables and other polluting energy sources such as coal, oil and natural gas supplies more than 80% (25% coal, 35% oil and 21% natural gas) of the world’s energy and until recently have been accessed relatively easily, is inexpensive and abundant [1.40, 1.23,1.7]. Nevertheless, it has slowly been discovered that by exploiting these resources that

further aggravation of pollutants have severely harmed the planet. Figure 1.1 illustrates the various energy resources employed to appease the global energy demand. In addition, the global trend in energy resources from the past to the present i.e. 2005 - 2030 and ideal alternatives to battle of the energy crisis for the future may also be studied [1.7].

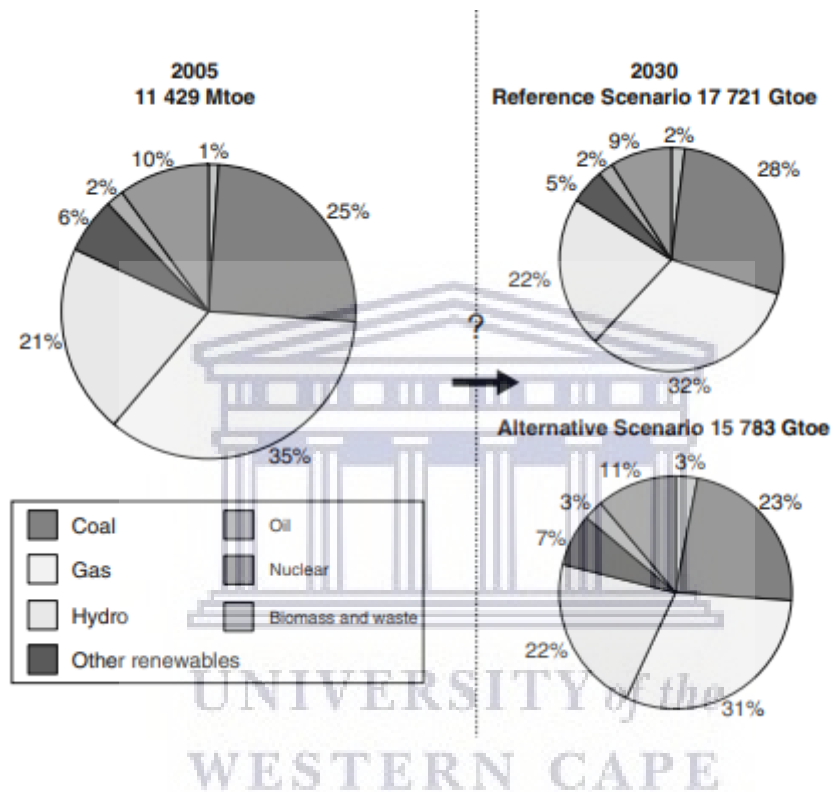


Figure 1.1: Schematic of the world energy balance of various energy sources and their contribution to the global energy demand predictions and alternative energy consumption scenarios [1.7].

The energy crisis and climate change are two separate terms with their own distinctive definitions but are still highly relatable to one another in some way [1.16]. It is known that the Earth’s atmosphere is composed of combination of gases which eventually has an impact on climate stability. When solar radiation passes through the atmosphere, it heats the Earth’s surface. Once the radiation reaches the Earth’s surface, some energy is returned to the

atmosphere in the form of heat, whilst other parts of the incident solar radiation is retained by a layer of gases and the remainder is passed into space. This is known as the greenhouse effect. When fossil fuels are burnt or combust in order to generate energy, they emit vast amounts of harmful greenhouse gases (GHG's) which warms the Earth's surface through heat retention, which subsequently instigates global warming and climate change [1.23, 1.40]. A few of the most forthcoming greenhouse gases in the atmosphere are carbon dioxide (CO₂) contributing an excessive 71.4%, while methane (CH₄) accounts for 17.5% and nitrous oxide (N₂O) for 10% [1.7].

Between the years from 1850 - 1899 and 2001 - 2005, the global average surface temperature had advanced by 0.57 °C and 0.95 °C, respectively [1.16]. In addition, Levy, R. has founded possible scenarios, where models have predicted that these temperatures may rise between 2 - 6 °C by the end of the 21st century [1.19]. Mishra et al. has concurred that in the late 1980s, the World Meteorological Organization/ International Council of Scientific Unions/ UN Environment Programme Advisory Group of Greenhouse Gases had projected that if these threshold temperatures were reached, it would instigate risks of grave damage to ecosystems. Such irreparable damage triggers grave threats to endangered species and unique systems [1.25]. These threats are executed by the increase of precipitation frequency, thus resulting in floods, rising sea levels, acid rain, intense frequent heat waves causing droughts, a decrease in both snow cover and sea ice, and even an increase in water-borne diseases implicating the standard of health for the human population [1.25, 1.41].

By 2006, it seemed as though the seriousness of the situation had finally been grasped by a number of countries globally. Within the same year, the G8 leaders (Canada, France, Germany, Italy, Japan, Russia, the United States of America and the United Kingdom) met

with the leaders of major developing countries (China, India, Brazil, South Africa and Mexico) now known as the 'Plus five' (+5), had come to a consensus with regards to the International Energy Agency's (IEA) concerns listed by the World Energy Outlook (2006). Through advisement of the IEA, the G8+5 leaders agreed to pursue alternative energy scenarios and strategies aimed at a clean, clever and competitive energy future. This decision has caused leaders to place an emphasis on renewable energy resources as it seems to be the most effective and efficient solution to the crisis at hand [1.7].

At present, there are a list of renewable energy resources available on earth such as solar, biomass, wind and geothermal [1.6, 1.2, 1.16, 1.28]. Nevertheless, even though continuous efforts have been formulated to expand the use of such renewable energy sources, not more than a mere 20% of these resources are used for electricity generation. Amongst all the viable renewable energy sources, solar energy proves to be a feasible answer to the consumption and ever dwindling amounts of fossil fuels problem [1.1, 1.16]. The concept of reaping the sun's energy (green energy) as a means of providing electricity seems the most appealing as it is the most inexhaustible renewable source of energy due to the sun's 4 - 5 billion year lifespan. It has formerly been mentioned by Psomopoulos et al. that the amount of solar energy that eventually reaches the earth is estimated to be 173×10^{12} kW which is more than what is required to support the energy needs by humankind if harvested correctly. Of sun's total energy 7% is attributed to ultraviolet (UV) radiation which causes damage to materials but is considerably filtered out by the ozone layer and upper atmosphere. Visible radiation contributes 47%, and 46% is supplied by infrared (heat) radiation, and are both mainly used for energy creation in the earth's surface by humans and nature [1.34].

Although the amount of solar energy reaching the earth's fairly high, the amount which is accessible, however, is dependent on a number of factors such as the change latitude, elevation, shape of the surface, season of the year coupled with the time of day. Based on these influential factors, it is evident that the potential amount of energy availability and implementation of the renewable source varies according to weather conditions and geographical properties of the area. Figure 1.2 illustrates a mapping of suitable regions for the theoretical amount of solar radiation available to the earth's surface. The map displays an indication of appropriate areas with the best potential for solar energy utilisation technologies may be applied globally. Furthermore, by observing these mapping, it is quite clear that majority of the developing and some of the developed countries situated along the tropical belt of the world exhibits the most promise for the application of solar radiation devices. For countries situated along the "Sun Belt" of the world, these regions receive the sun's radiation for approximately 3000 - 4000 h/year. This translates to an excessive 2000 kWh/m² per year in terms of power density and is few thousand times greater than what the estimated global energy demand of 4.40×10^9 kWh/year for the year 2040 will be. [1.33, 1.34] .Studies performed by the EPIA- Greenpeace in 2011, Luque and Hegedus in 2003, Sen in 2008, and Šúri et al. in 2007 have all been listed by Psomopoulos et al. who mentioned that "the earth is exposed to enough sunlight to generate annually, using current available technology, electricity with an average value equal to 1700 kWh/m² of land" [1.34].

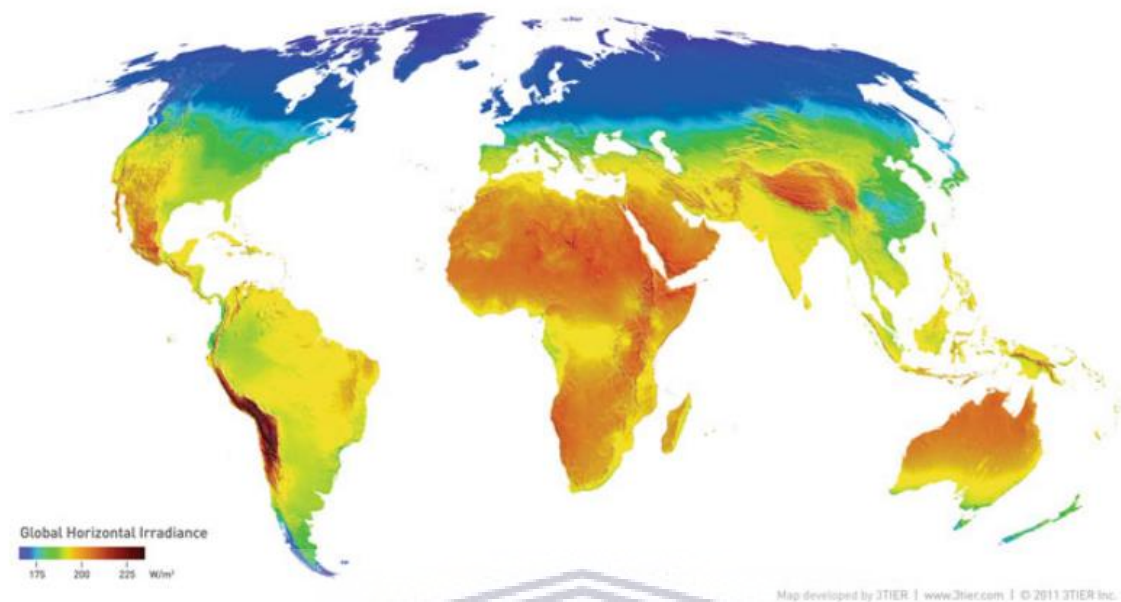


Figure 1.2: Amount of solar radiation at the Earth's surface [1.34].

Photovoltaic solar cell (PSC) devices have the ability to convert solar energy directly into electricity [1.1, 1.34, 1.43, 1.15, 1.24]. In recent years, photovoltaics (PVs) has become one of the solar powered technologies to have received immense popularity and is one of the fastest growing renewable energy sources worldwide. This is based on the amount of installations over the past few years. Figure 1.3 shows the global cumulative capacity of solar PV installations from the year 1996 - 2019 [1.30]. Since (PSC) devices function on what is considered a natural unlimited resource, it therefore provides the potential of creating a cleaner, more reliable and affordable electrical system [1.16, 1.29]. In addition to these favourable attributes, PSC devices consists of a rugged yet simplistic design, requires minimal upkeep, and has a stand-alone assembly system that providing outputs in the range from microwatts to megawatts [1.6]. These are basic reasons why governments all over the world supporting the development and employment of solar PV technology [1.11, 1.40].

However, as appealing as what these features may seem, PSC devices still faces several challenges such as contact shadowing, parasitic resistances or non-radiative recombination, and consequently has a negative impact on the efficiency. Due to continuous research, numerous ideas have been investigated and proposed to overcome these issues in order to fully take advantage of the radiation that the sun provides [1.18].

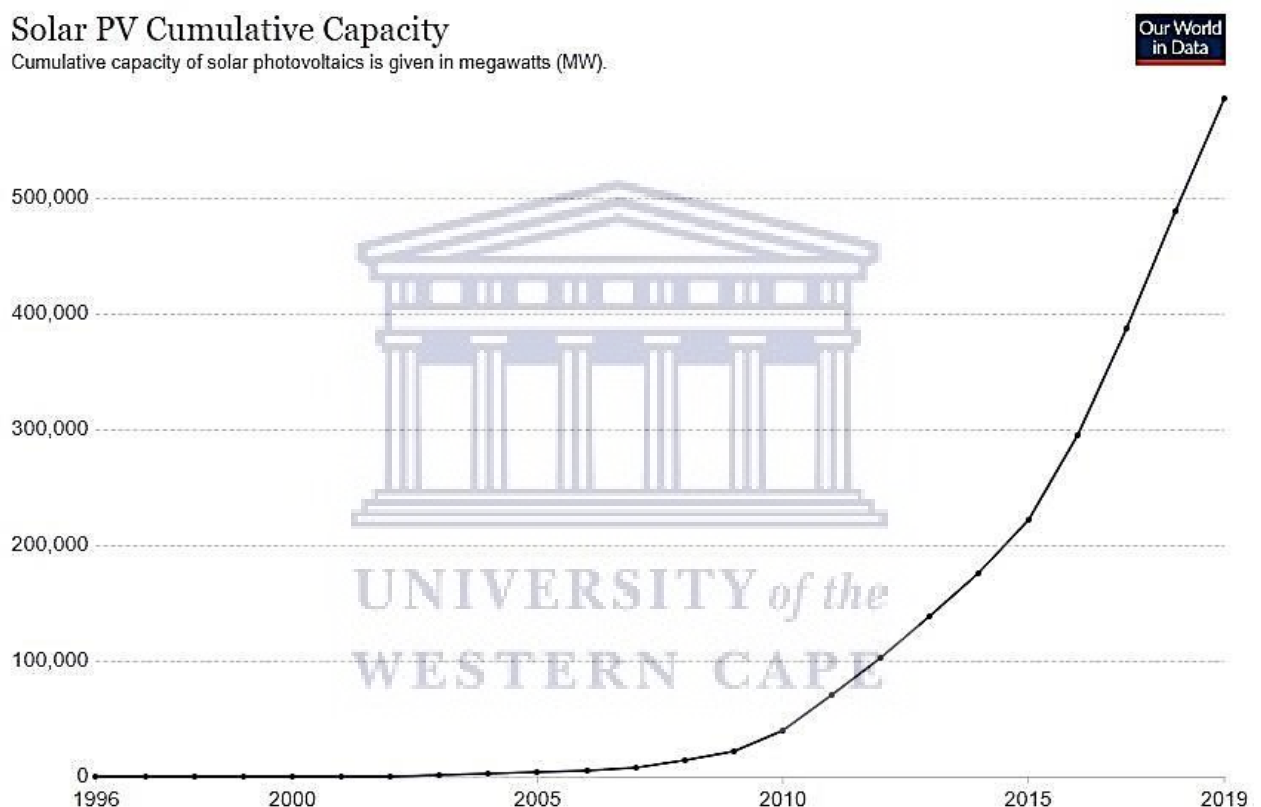


Figure 1.3: Tally of PV installations performed globally from 1996 - 2019 [1.30].

1.2 Photovoltaic Cells

The term “photovoltaic” is a combination of the Greek word “phos” meaning light, and “volt” being the unit measurement of the electro-motive force. Photovoltaic solar cell (PSC) devices are primarily based photovoltaic effect discovered by the French physicist

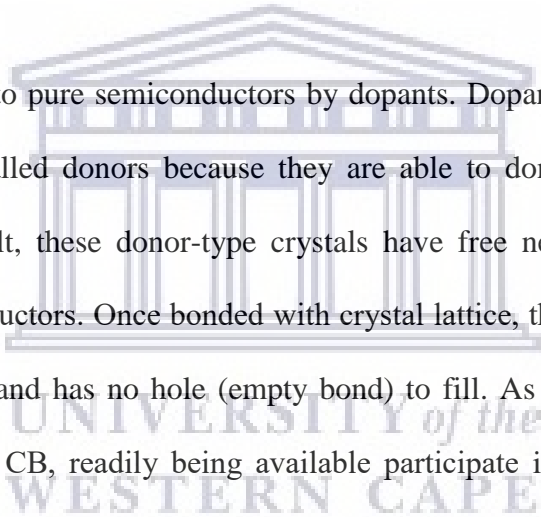
Alexander-Edmond Becquerel. In the year 1839, at the tender age of 19, Alexander managed to invent the first photovoltaic solar cell [1.32, 1.43]. By illuminating silver chloride based in an acidic solution, he noticed a voltage on the connected platinum electrodes [1.43].

The definition for the photovoltaic effect described by Miles et al., where they define it as “the direct conversion of incident light into electricity by a p-n semiconductor junction device” [1.24].

1.2.1 Working Principle

When incoming photons of energy ($h\nu$) interacts with the active area of the PSC, they have the ability to be absorbed if the requirement of $h\nu \geq E_g$ is met. E_g represents the band gap of the depletion region. Once the requirement of $h\nu \geq E_g$ is fulfilled, these photons possess the potential to free an electron from its bound state within a crystal. [1.1, 1.36]. Once an electron is freed, it is allowed to move throughout the crystal in the conduction band (CB), where it subsequently leaves behind a missing electron bond also known as a hole within the valence band (VB). Since a hole is now available within the VB, a bound electron that is in a close proximity to the hole can thus easily jump into the hole, and in doing so, forms another incomplete bond i.e. a new hole. This continuous process of nearby electrons exchanging positions with holes ultimately causes the random appearance of holes throughout the solid. The production of these freely moving electrons and holes is the fundamental procedure outlined by the PV effect and is also responsible for the generation of electron-hole pairs. This procedure however, is not capable of generating an electric current as yet, and so further insight of how a PSC is able to generate such an electric current will be discussed shortly. [1.1, 1.13].

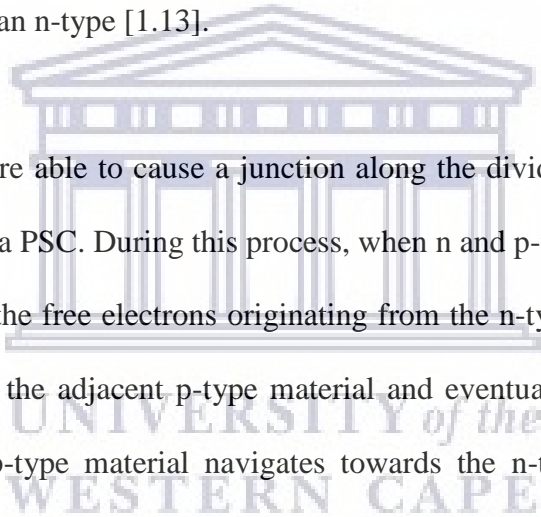
It is a noteworthy fact that at higher temperatures, the electrons and holes become more restless and move more frequently within the material. PSC devices all consist of a potential barrier that is formed by opposing electric charges facing one another on either side of a dividing line. This potential barrier selectively absorbs light and consequently generates free electrons and holes, by continuously transferring both electrons and holes to opposing sides. There is a multitude of ways in which this potential barrier can be created within a solar cell. Nonetheless, the most common practice is to alter a pure semiconducting crystal with impurities so that either side of the dividing line consists of a donor and acceptor semiconducting material, respectively [1.13].



Impurities are introduced to pure semiconductors by dopants. Dopants composing of one or more valence electrons called donors because they are able to donate electrons to a pure semiconductor. As a result, these donor-type crystals have free negative charges and are known as n-type semiconductors. Once bonded with crystal lattice, the impurity atom's extra electron is relatively free and has no hole (empty bond) to fill. As a consequence, the free electron remains crystal's CB, readily being available participate in an electric current. A crystal with a large amount of impurity dopants would have plenty free mobile electrons within the CB. In addition, the excess in free electrons has a similar amount of positive impurity ions bound to the crystals structure. Hence in this manner, the crystal as a whole will remain neutral since the number of electrons is approximately the same as the number of ions. However, these majority charge carries will alter the crystal's electrical properties immensely [1.13].

Accordingly, a pure semiconductor crystal can also be altered by substituting impurity atoms with one or less valence electrons. In doing so, the dopant atom with fewer valence electrons

would occupy position of the original crystals atom, however, one of the bonds will lack an electron, and hence a hole is created. As we know, holes are relatively mobile within the VB in the same way that free electrons are in the CB. Therefore, impurity atoms who have many holes act as if they were free mobile positive charges in the lattice. When pure semiconducting crystals are altered in this way, they are known as acceptors due to its capability to readily accept electrons coming from the rest of the crystal normally in the form of bonded valence electrons or CB electrons. Due to the presence of majority positive charge carriers (moving holes), these acceptor-doped materials are called p-type. In a material where majority charge carriers are negative (free mobile electrons), and the dopant has an excess of valence electrons is called an n-type [1.13].



N- and p- type materials are able to cause a junction along the dividing line responsible for the flow of free charges in a PSC. During this process, when n and p-type materials come into contact with one another, the free electrons originating from the n-type material makes their way to the many holes in the adjacent p-type material and eventually fill the holes. In the same way, holes in the p-type material navigates towards the n-type material side, thus causing an imbalance of charge. An electric field is configured by charged carriers that have already crossed over the junction and forms a barrier for charge carrier separation. This is achieved by the enlargement of the barrier which is triggered by increased amounts of carriers crossing over the junction. Due to the enlargement of the barrier, navigation of free carriers becomes more difficult, until finally equilibrium is reached and statistically speaking, no more electrons are allowed to traverse through the junction. This separation between electron and hole charges generates a potential difference (voltage) between the two terminals of the PSC. This can then be used to drive an electrical current to an external circuit. Schematic of the entire process may be observed in Figure 1.4 and 1.5, respectively, such that

Figure 1.4 illustrates the internal process within the crystal and Figure 1.5 shows the external features of how a PSC is employed for electric current production [1.13].

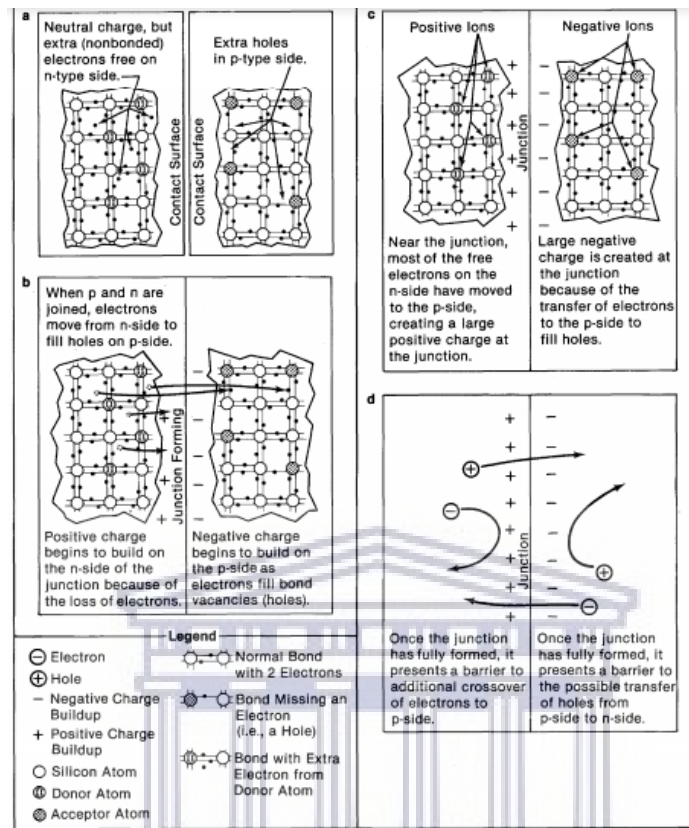


Figure 1.4: Formation of the p-n junction within a PSC [1.13].

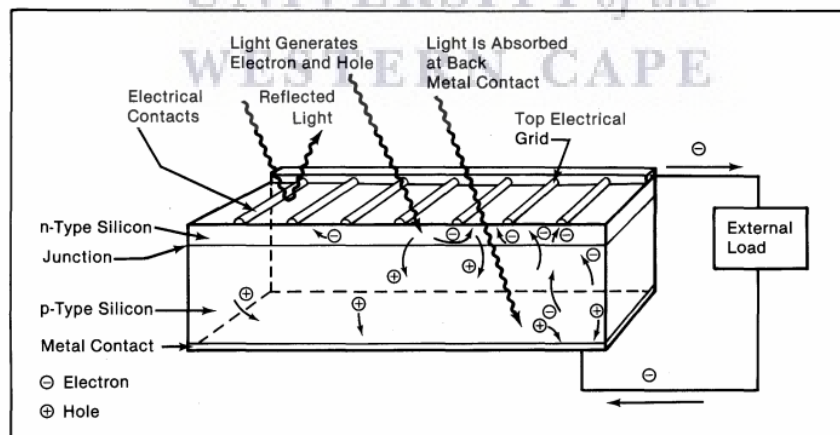


Figure 1.5: Schematic of how the absorption of light induces a voltage that drives current through a circuit [1.13].

1.2.2 Photovoltaic Solar Cell Classes

PV solar cell devices can be divided into three classes (generations) [1.36, 1.17].

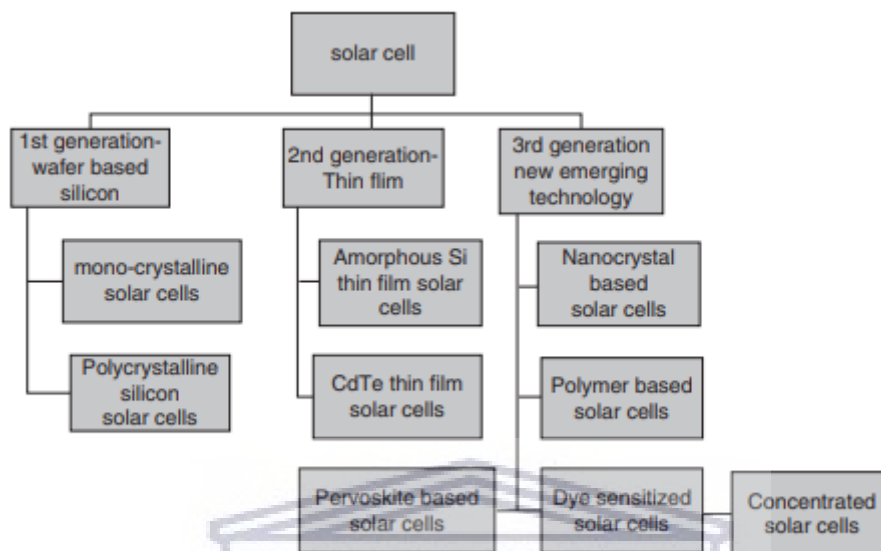


Figure 1.6: Generational classes of available PSC device designs [1.39].

1.2.2.1 First Generation Solar Cells

First generation solar cells essentially involves devices made up of monocrystalline silicon (m-Si), polycrystalline silicon (p-Si) wafers and gallium arsenide (GaAs) PSCs [1.22, 1.36, 1.11]. Being the most recognized and mature form of PV technological devices, these cells dominates above 80% of the solar cell market and reaches efficiencies of approximately 22 - 25% in the laboratory [1.17, 1.36]. Efficiencies in these types of PSCs are primarily restricted by the spectral response of a single-junction semiconductor [1.36].

1.2.2.2 Second Generation Solar Cells

Second generation solar cells are fundamentally centred around thin – film devices. The main purpose surrounding the manufacturing of these films is to aid in the reduction of high costs associated with first generation solar cell prices. Costs are often reduced by lessening the amount of production materials and by using a lower grade in materials deposited on more cost effective substrates. Popular materials employed in second generation PSCs include amorphous silicon (a-Si), cadmium telluride (CdTe), and copper indium gallium selenide (CIGS) [1.17, 1.22, 1.36].

1.2.2.3 Third Generation Solar Cells

Third generation solar cells involves the field of new emerging PV technologies. This class of PSCs was initially invented with the intention of manipulating novel materials in order to establish new innovative designs. Third generation PSCs are intended to assist in improving production costs as well as the enhancement of efficiencies compared to PSC devices that are already marketed today. Among the new developing PSCs are multi-junction solar cells (MJSCs), dye-sensitized solar cells (DSSCs), quantum dot-sensitized solar cells (QdSCs), organic and polymeric solar cells (OPSCs) and perovskite solar cells (PSCs). [1.17, 1.36]. All of the above mentioned third generation solar cells individually possesses their own benefits and limitations in terms of cost, stability, size, transparency, flexibility and efficiency. So far, 47% is the highest reported efficiency in MJSCs [1.36].

1.3 Perovskite Solar Cells

Perovskite solar cells (PVSCs) are one of the more popular up-and-coming forms of new generation photovoltaic technologies. Like most emerging PSCs, PVSCs offer more straightforward and inexpensive way of producing a PSC. In a period of less than 5 years PVSCs efficiencies have advanced from a mere 3.8% to a remarkable 20.2% [1.36]. Based on these advantageous attributes and its potential of producing high efficiencies, many scientists are invested in coming up with a more stable and reproducible cell as an alternative to other energy harvesting resource techniques [1.43].

1.3.1 Perovskite Structure

PVSCs are PSCs which are primarily based around the perovskite material, hence the name given to the PSC. Perovskite materials have a general formula of AMX_3 , such that A and M are cations which are different in size relative to one another. More specifically “M” is smaller in size than “A”. For a more direct understanding of the structural concept, the perovskite crystal may also be expressed in the more general AMX_3 formation, where the metal cation is given by M, and X represents either an oxide or halide anion. In the case of perovskite materials, MX_6 forms an octahedral arrangement, such that M is situated at the centre of the octahedron surrounded with X at the corners. Figure 1.8 displays an illustration of the octahedron perovskite crystal structure. [1.26]

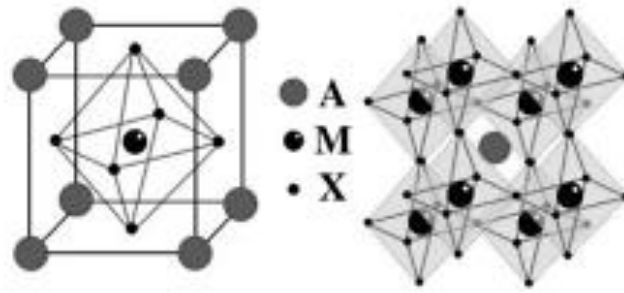


Figure 1.7: (a) Ball and stick model of a basic perovskite crystal structure and (b) illustration of an extended perovskite crystal structure connected via a corner – octahedra [1.26].

For a closed-packed perovskite crystal structure, the type of cation which assumes the value of A must meet a certain criterion. That is, that the cation A must fit in the hole that is situated between the eight corners of the octahedron. The types of elements that are capable of being the cation A are calcium (Ca), potassium (K), tin (Sn) and lead (Pb). The size of both the cation and anion are highly influential to the electronic and optical properties of the perovskite material. An ideal perovskite material obtains the crystal structure in the form of a cubic geometry. However, in nature this structure becomes distorted and pseudo – cubic forms are found. In a perfect perovskite structure, where atoms touch one another, the larger cation occupies a 12 co-ordinate position, the distance of M - X is equal to $a/2$ and the A - X distance is $\sqrt{2} (a/2)$. In this instance, the value of a denotes the cubes unit cell length. According to Rao et al., the radii of the ions can be related by the following expression:

$$R_A + R_X = \sqrt{2}(R_M + R_X) \quad (\text{Eq 1.1})$$

Furthermore, Goldschmidt had discovered a tolerance factor t , for perovskite structures in the form AMX_3 that did not follow the relation outlined by Eq.1.1, and thus deduced the following expression:

$$t = \frac{R_A + R_X}{\sqrt{2}(R_M + R_X)} \quad (\text{Eq. 1.2})$$

In an idyllic case, where the perovskite structure is cubic, the value of t is unity. In other instances where the value for t variates within the range of $\sim 0.75 < t \leq 1.0$, the perovskite structure then distorts to tetragonal, rhombohedral, or orthorhombic symmetry [1.20, 1.26, 1.35].

In two-dimensional (2D) perovskite structures, an appropriately employed cationic organic molecule is used as “A”. This is commonly known as the organic part of the structure, while octahedron MX_6 is the inorganic part. The inorganic part of the perovskite structure is found confined between the organic cationic molecules. Due to the cation features of the organic molecule, the placement of the organic and inorganic parts are situated at alternating locations leading to a 2D organic-inorganic layered perovskite. Figure 1.8 exhibits the structure of a 2D organic-inorganic perovskite where: a) consists of a bilayer and b) has a single layer of organic molecules. An example of this is given by perovskites consisting of the general form of $CH_3NH_3MX_3$ which are utilized in field effect transistors and electroluminescent technologies. The fairly wide direct band gap of the perovskite can be controlled by changing the alkyl group and the metal ion. It is for this reason that it can be deduced that size, structure, conformation and charge of the organic cation regulates the properties of the perovskite material [1.26].

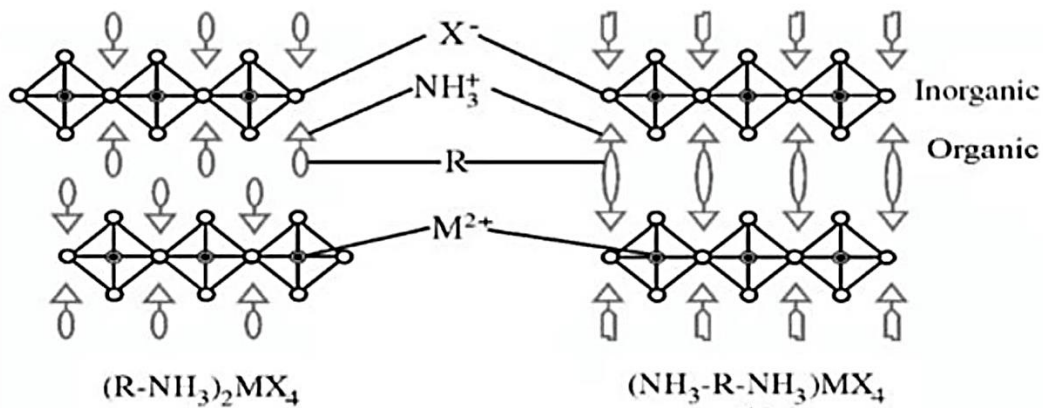


Figure 1.8: 2D Structure of an organic-inorganic perovskite structure with a) bilayer and b) a single layer of organic molecules. [1.26]

1.3.2 Structure of Perovskite Devices

The standard configuration of a PVSC generally consists of a perovskite structured compound employed as the light harvesting active layer [1.22]. Organic-inorganic lead or tin halide-based perovskites are often used to this purpose. Adjacent to this active layer, are transport layers more specifically an electron transport layer (ETL) either being a mesoporous or flat solid material, and a hole transport (HTL) placed on either side of the perovskite compound. Upon the ETL layer exists a TCO while the back of the HTL layer has a back contact electrode often made up of gold (Au) [1.22, 1.44]. When light passes through the TCO to the ETL layer an n-i-p type of cell is formed. The reverse of this cell layout is known as a p-i-n structures PVSC. In the p-i-n layered PVSC, the perovskite active layer is deposited onto transparent substrates which are shielded with an HTL like poly(3, 4-ethylene dioxythiophene): polystyrene sulfonic acid (PEDOT: PSS). Both forms of PVSC has demonstrated high performance and stability, but when comparing the two structures to one

another with regards stability, the results are still inconclusive as to which outperforms the other and is thus still under debate properties [1.44].

Figure 1.9 displays a diagram illustrating the layout of variant perovskite device designs available.

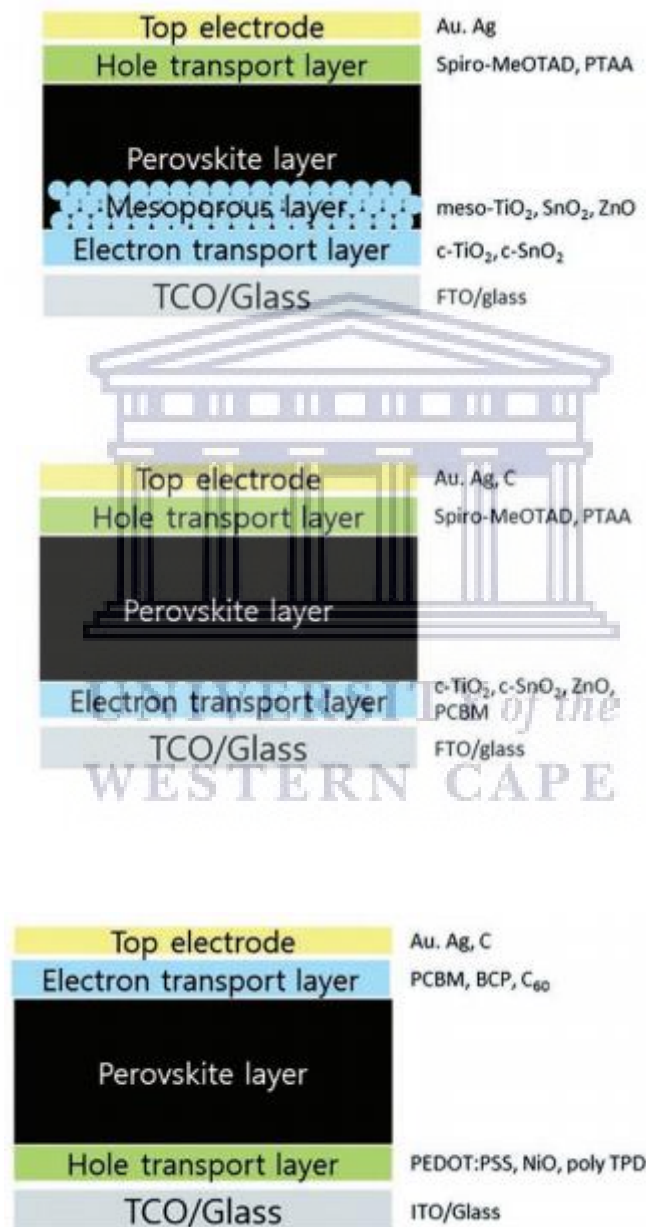


Figure 1.9: (a) Mesoporous n-i-p structured perovskite device, (b) planar n-i-p structured perovskite device and (c) planar p-i-n structured (inverted planar) perovskite device [1.44].

1.3.3 Instability and Degradation factors in Perovskite solar cells

Over the past few years PPSC's have become quite appealing to many researchers due to their many alluring attributes such as low material costs and overall simplistic manufacturing procedures. Nonetheless, as promising as what a successfully created PVSC may seem, they still experience a number of severe instabilities which prohibits them from being marketable. These limitations are influenced by two main factors; i.e. ambient humidity and UV light exposure. Moisture causes degradation in both $\text{MAPbI}_{3-x}\text{Cl}_x$ and MAPbI_3 which is triggered by the loss of the methylamine group through sublimation where PbI is then formed. When perovskites are subjected to UV radiation and dry air conditions, the perovskite decomposes into reaction products of methylamine, PbI and I_2 . Many researchers have made an immense amount of efforts to solve these crucial issues [1.44].

1.3.4 Transport layers and their influence on stability

Even though the instabilities which represent themselves within the photoactive layer of the device are crucial to the overall performance of PVSC, there are other factors which are able to affect the stability of the cell as well. These other vital components are the transport layers (ETL and HTL). The function of these two layers are vital for the cells execution simply because they provide sufficient charge collection efficiency, and secondly, they act as an ohmic contact for the electrode. Therefore, it is of utmost importance that the properties of these transport layers are understood properties [1.44].

1.3.4.1 Electron Transport layer

In order to assemble a high performance PVSC obtains a good conversion efficiency, a reliable electron selective contact is needed between the ETL and the perovskite active layer. This selective layer serves in the purpose of minimizing the potential barrier for electron charge transfer and hinder hole transport so that carrier recombination doesn't occur at the interface. As ETL removes the photogenerated electrons from the photoactive layers, and transfers them to the cathode, where they promote photovoltaic performance. Basic requisites that should be met before a material is regarded as a suitable match for a PVSC are that it should form a suitable alignment between the perovskite film and the electrode. Secondly, the material should possess a high electron mobility, have a great stability in air and easy termination degradation if exposed to an organic solvent. If a proper ETL is chosen, it is able to improve the PVSC by introducing flexible substrates, having lower processing temperatures, straightforward fabrication, most importantly decreases the chances of hysteresis. On the other hand, if an inappropriately chosen ETL is selected, a poor carrier efficiency and damage of the ohmic contact in conjunction with the electrode properties will result. [1.44].

1.3.4.2 Hole transport layer

HTL are also critical to the conversion efficiency of PVSC because they are assigned to prevent the travelling of electrons between the perovskite and electrode to lessen carrier recombination, and thus consequently increasing the device efficiency. Additionally, HTL protect the perovskite from harmful external elements which promote degradation by moisture, oxygen and heat properties [1.44].

1.3.5 SnO₂ as an ETL for Perovskite solar cells

A component of PVSC as previously stated in section 1.3.4.1 that is critical to the overall stability of the device is the ETL. The role of the ETL is to support electron extraction and hole blocking to prohibit the hole from reaching the transparent electrodes [1.14].

At the moment there are a variety of options which have been opted for as a candidate for ETL use. Organic conducting materials namely graphene, fullerene and some of its variants have been studied as possible ETL, but due to their environmental, thermal and photostability has brought on apprehension for long-term use [1.14]. Therefore, instigating the search for planar and mesoporous n-type metal oxides to satiate these vastly challenging issues. Some possible inorganic metal oxides that can be used for ETL are TiO₂, SnO₂, ZnO₂SnO₄, WO₃ and so forth have been opted for [1.44, 1.14]. Each of these metal oxides has their own appealing factors and limits, however, SnO₂'s overall properties has brought on the most appeal [1.14]. Five of these attractive properties as listed by Jiang et al. are: 1) Its deep conduction band and excellent energy level for electron extraction and hole blocking. 2) Increased electron mobility in its bulk form up to 240 cm² v⁻¹ s⁻¹ and high conductivity aiding in electron transport and reduces the chances of recombination loss. 3) The high level of transmittance in the visible region of the EM spectrum combined with its wide band gap between 3.6 - 4.0 eV. 4) Its ability to be produced at low temperatures (less than 200 °C), making it an excellent contender for flexible solar cell and tandem solar cell applications resulting in simplistic large – scale commercialization. 5) Excellent chemical stability such as UV-stability, less photocatalytic activity in comparison to other ETLs and overall its robustness [1.14].

1.3.5.1 Modifications of Perovskite solar cells by the implementation of SnO₂

Hysteresis and its misleading efficiency outcomes is a prevalent and significant problem faced by PVSCs. There exist several reasons that have been discussed to clarify as to why this phenomena has become quite evident, these are issues such as the charge trapping at interfaces and grain boundaries, capacitive, ion migration as well as ferroelectric effects. Although lately, charge collection brought on by ion migration seems to be the most logical justification [1.14]. SnO₂'s deeper conduction band joint with its higher conductivity and electron mobility is what makes it advantageous over most metal oxides. These assets are what induce easier charge transference that limits charge accumulation at the interface. According to Jiang et al., in comparison to the formidable TiO₂, SnO₂'s use as an ETL in a regular planar PVSC (n-i-p) structure has displayed a significant decrease in hysteresis behaviour and has been successful in solving this problem in n-i-p structured PVSC. The use of colloidal SnO₂ as a precursor solution and the subsequent spin-coating thereof made way for the production of a high quality SnO₂ thin film which generated a 19.9% conversion efficiency. These results had showed little to no hysteresis, where it has been confirmed that it was owed to the increased extraction of electrons by the SnO₂ ETL formed as a consequence of the deeper conduction band and enhanced mobility of the SnO₂ metal oxide [1.14].

SnO₂ materials are fairly vigorous and show some immunity to oxygen and moisture filled environments. Such invulnerability (chemical stability) under atmospheric conditions in a material demonstrates quite valuable properties for PVSC devices, more specifically in transport layers. A study performed by Fang et al., whilst employing hierarchical SnO₂

nanosheets as an ETL, proved that PVSC with these kind SnO₂ materials could retain 90% of its initial efficiency in storage without encapsulation for 3000 hours. Another study was done on reverse p-i-n structured PVSC by Jen and colleagues who combined as-synthesized SnO₂ nanocrystals and C₆₀ as an ETL adjacent to the perovskite active layer. In doing so, the use of the thick SnO₂ compact layer displayed an improved moisture stability varying from 10 - 80%, and is capable of maintaining 80% of its original efficiency placed under 70 - 80% relative ambient humidity for 30 days [1.14].

Photostability in PVSC is another forthcoming concern placed by researchers. In the more general TiO₂ ETL, UV light exposure promotes the performance degradation by the oxygen vacancies present in TiO₂ crystal lattice provoked under UV illumination activation. Subsequently, desorption of O₂ passivates these deep electronic traps. When these deep traps emerge within the lattice, they cause the electronic properties of the material to worsen. The degraded electronic properties which ultimately destroys the activity at the interface ensues conversion efficiency loss. Under similar circumstances SnO₂ behaves in a more robust manner due to its catalytic activity. You et al. substantiated this statement by comparing the short time stability while using TiO₂ and SnO₂ as an ETL in planar PVSC under constant sun conditions. The results proved that SnO₂-based devices had an improved photostability than that of the TiO₂-based device. Furthermore, Wang et al. demonstrated that by placing SnO₂ alongside the perovskite layer under continuous UV illumination for 6 hours that the PVSC (FTO/SnO₂/(FAPbI₃)_{0.85}(MAPbBr₃)_{0.15}/Spiro-OmeTaD/Au structure) remained stable [1.14].

1.4 Properties of SnO and SnO₂ materials

Tin oxide based-materials are exceptional semiconducting metal oxides (SMO_x) and have received much interest from researchers in aid to fully exploit the advantages that this material and its derivatives have to offer, especially in the nanoscale. A few of tin oxide material variations are SnO, SnO₂, Sn₂O₃ and Sn₃O₄. Amongst all these variations of tin oxide SMO_x, SnO₂ is the most popularly studied and utilized material in a number of devices. More recently, SnO based-materials have also been studied due to its ambipolar behaviour and the promise of its high mobility. Therefore, in this section a brief overview of the properties pertaining to the two most prominently utilised derivatives of tin oxide will be discussed. Listed in the table below (Table 1.1) are the general properties SnO and SnO₂ materials provided by [1.29]. Moreover, one of the many ways in which tin oxide materials may be manufactured is through thermal corrosion of the metallic Sn species. With that said, in Figure 1.10 presents a phase diagram of tin (Sn) and oxygen (O) in which the thermal conditions can be studied so that an estimate of the desired form of Sn_xO_y may be accomplished. Applications Sn_xO_y nanomaterials are in PVSC, TFT's, sensors and catalysts.

Table 1.1: General Properties of SnO₂ and SnO [1.29].

	SnO ₂	SnO
Name	Stannic oxide	Stannous oxide
Chemical classification	Oxide	Oxide
Crystalline system	Tetragonal	Tetragonal ^b or Orthorhombic
Space group	P4 ₂ /mnm	P4/nmm ^b
Cell parameter (Å)	4.738 × 4.738 × 3.187	3.802 × 3.802 × 4.836
"a" × "b" × "c"	< 90° × 90° × 90° >	< 90° × 90° × 90° >
Density	6.99 g/cm ³	6.40 g/cm ³
Melting point	1898 K	1315 K
Hardness	6–7 Mohs	
Color	Transparent (single crystal) or white (polycrystalline)	Dark gray
Optical bandgap	3.4–3.7 eV	2.4–2.7 eV
Fundamental Bandgap	3.4–3.7 eV	0.7 eV
Position of VBM (ionization energy)	~ -9 eV	~ -5.8 eV
Electrical classification	n-type semiconductor	p-type semiconductor
Dielectric constant	9.0	15

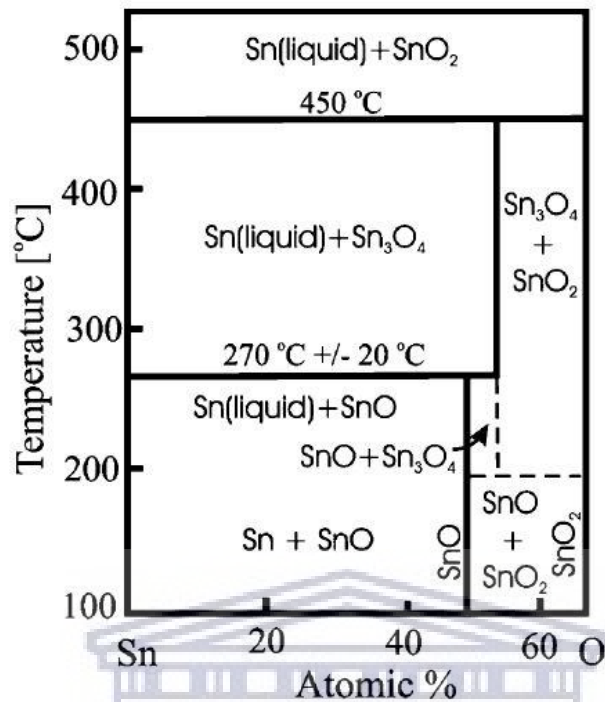


Figure 1.10: Phase diagram of Sn – O [1.3].

1.4.1 Crystal Properties

Stannic oxide (SnO_2) is the most thermodynamically stable form of tin oxides. SnO_2 crystallizes in a tetragonal rutile structure as illustrated in Figure 1.12, with the space group of $P4_2/mnm$ (D_{4h}^{14} symmetry) and has lattice constants $a = b = 4.7374 \text{ \AA}$ and $c = 43.1864 \text{ \AA}$ [1.3, 1.9, 1.37]. In the rutile structure of stannic oxide, each Sn(IV) ion is located at the centre of the distorted octahedra of oxide ions. The c/a ratio and the internal parameter denoted as u , are responsible for the atomic positions of the crystalline structure. Cations are situated at equivalent positions of $2(a) \left[(0,0,0) \text{ and } \left(\frac{1}{2}, \frac{1}{2}, \frac{1}{2} \right) \right]$, while the anions are found at positions $4(f) \left[\left(\frac{1}{2}, \frac{1}{2}, 0 \right), \left(-\frac{1}{2}, -\frac{1}{2}, 0 \right), \left(-u + \frac{1}{2}, u + \frac{1}{2}, \frac{1}{2} \right), \left(u + \frac{1}{2}, -u + \frac{1}{2}, \frac{1}{2} \right) \right]$. In this way, the

anions form an octahedral surrounding the cations, with two anions at a distance of $d_1 = \sqrt{2}ua$ and four anions at a distance $d_2 = \sqrt{2(\frac{1}{2}-u)^2a^2 + (\frac{c}{2})^2}$. The perfect octahedral coordination is obtained when d_1 and d_2 are equal, which is a consequence of the internal parameter u and c/a ratio achieving the best values of $u_{ideal} = \frac{1}{2}(2 - \sqrt{2}) = 0.293$ and $c/a_{ideal} = 2 - \sqrt{2} = 0.586$, respectively. Furthermore, the distortion parameter within the crystal is given by the relation $c/a - 2u$. In a perfect crystal structure the distortion of the crystal will amount to 0, therefore, $c/a - 2u = 0$ and any deviation from this is an indication of distortion within the octahedral [1.37]. Figure 1.11 displays a schematic of SnO_2 's crystal structure [1.3].

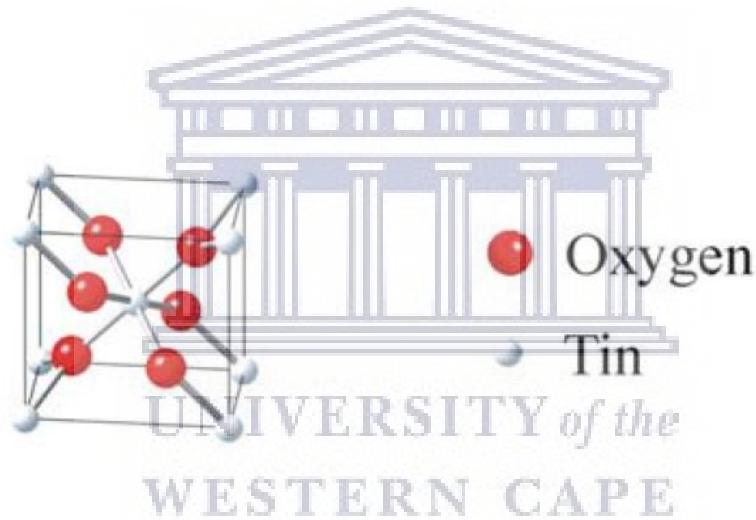


Figure 1.11: Ball and stick model of SnO_2 crystal structure [1.3].

Tin monoxide (SnO) or stannous oxide crystallizes into a distorted tetragonal structure commonly known as the litharge structure. The SnO litharge crystal structure can be seen in Fig. 2.1, with the space group $P4/nmm$ and has lattice constants $a = b = 3.8029 \text{ \AA}$ and $c = 4.8382 \text{ \AA}$ [1.3, 1.37]. The crystal structure Sn ions are located at equivalent positions $2(c), \left[\left(\frac{1}{2}, 0, -u\right) \text{ and } \left(0, \frac{1}{2}, u\right)\right]$, while the oxygen (O) ions are at $2(a) \left[\left(0, 0, 0\right) \text{ and } \left(\frac{1}{2}, \frac{1}{2}, 0\right)\right]$. In SnO , both the Sn and the O are four-coordinate, such that O

ions are centred by a surrounding tetrahedron of Sn ions. The four coordinating O ions are located on the same side as the Sn ion, while a lone pair can be found on the opposite side. As a consequence, layers are situated in an *ab* plane, assembled in the *c*-direction joined by van der Waals interactions [1.3, 1.37]. The crystal structure of SnO is displayed in Figure 1.12 [1.3]. It is worth mentioning that in the presence of poor-oxygenated conditions, SnO₂ will decompose into SnO [1.37].

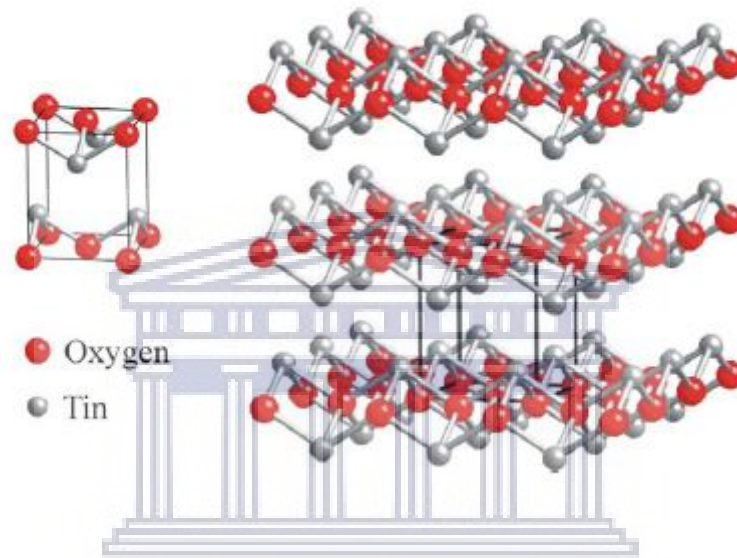
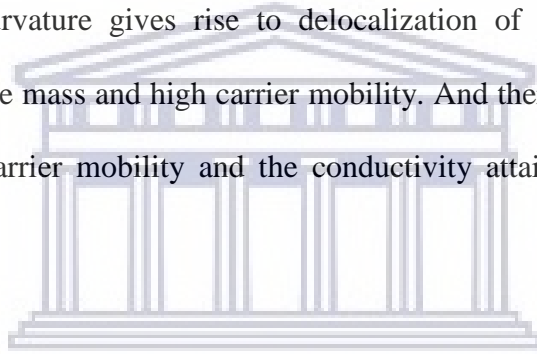


Figure 1.12: Ball and stick model of SnO crystal structure [1.3].

1.4.2 Electronic Properties

The electron configuration of Sn(IV) is given as [Kr]4d¹⁰5s⁰5p⁰. In Figure 1.13 and 1.15, the electronic band structure and density of states for SnO and SnO₂ may be studied. Orlandi et al. were able to model the electronic band structures using Vienna Ab initio Simulations Package (VASP) for density-functional theory (DFT) calculations. In their findings, the best modelling technique employed was that of the hybrid function of the generalized gradient approximation of Perdew, Burke, and Ernzerhof coupled with the Grimme “D3” dispersion correction i.e. the PBE0+D3 calculations executed using the python sumo package [1.37].

The electronic structure of SnO₂ has a valence band (VB) maximum that is governed by the highest occupied O 2p states and some Sn p states. While, the bottom of the conduction band (CB) consists of broad minimum antibonding Sn 5s and O 2p states at Γ . The interaction of these states consequently forms a highly dispersed conduction band minimum. This highly dispersed conduction band minimum is characteristic to n-type materials and results in a low effective mass. On the other hand, excellent p-type materials display highly dispersed VBM. SnO₂ has an effective mass of 0.3 m_0 and according to Savioli et al. in Orlandi et al.'s book of Tin Oxide Materials Synthesis, Properties and Applications; the effective mass is associated with the electrical conductivity. This is also linked to the curvature of the band edges such that a high degree of curvature gives rise to delocalization of electron/holes, and thus translates to lower effective mass and high carrier mobility. And therefore, a broad minimum can easily be linked to carrier mobility and the conductivity attained by n-type materials [1.37].



At the centre of the Brillouin zone due the crystal field effects, the CB of SnO₂ is split into Γ_1^+ and Γ_4^+ states, such that Γ_1^+ is completely symmetric and lower in energy. The VB of SnO₂ on the other hand, is split into nine states (Γ_1^+ , Γ_2^+ , Γ_3^+ , Γ_4^+ , Γ_5^+ , Γ_2^- , Γ_3^- , and two Γ_5^-), where Γ_5^+ and Γ_5^- are doubly degenerate. There is some confusion with regards to the ordering and the symmetries associated to the lower-lying states of the VB because according to Orlandi et al. experimental and theoretical finding disagree with one another. The direct transition at Γ between the CBM and the VBM is dipole forbidden for single photon absorption due to the symmetry between the Γ_1^+ and Γ_3^+ states. This absorption however, is only permissible for two-photon spectroscopy and related to the high onset absorption energy required for SnO₂ materials [1.37]. For SnO₂ rutile structures, absorption of direct photon energies where $h\nu \approx E_g$ does not take place, instead absorption only occurs for energies above the band gap

such that $E_g + \Delta \approx 3.79$ eV, where in accordance to M. Dou and C. Persson's calculations, $\Delta=0.72$ eV [1.37, 1.9].

Analytical techniques such as resonant photoemission spectroscopy, ultraviolet photoelectron spectroscopy, two-photon spectroscopy, electron energy loss spectroscopy, and XPS have previously been exercised in order to study the electronic structure of SnO₂ diligently. XPS results have proven that for SnO₂ a well-established 3d and 4d peaks can be expected to appear approximately at energies of 490 and 26 eV, respectively. At 8.4 eV, a spin-orbit splitting between the 3d^{3/2} and 3d^{5/2} peaks occurs, while at 1.1 eV the splitting of 4d^{3/2} and 4d^{5/2} peaks are found. Additionally, extended XPS studies have shown that the VB width of SnO₂ is approximately 8 eV, where 3 broad bands situated around 5, 8 and 11 eV is located below the Fermi level. While, for SnO Lau and Weirheim have reported binding energies of 3, 6.5 and 9.7 eV within the VB [1.37].

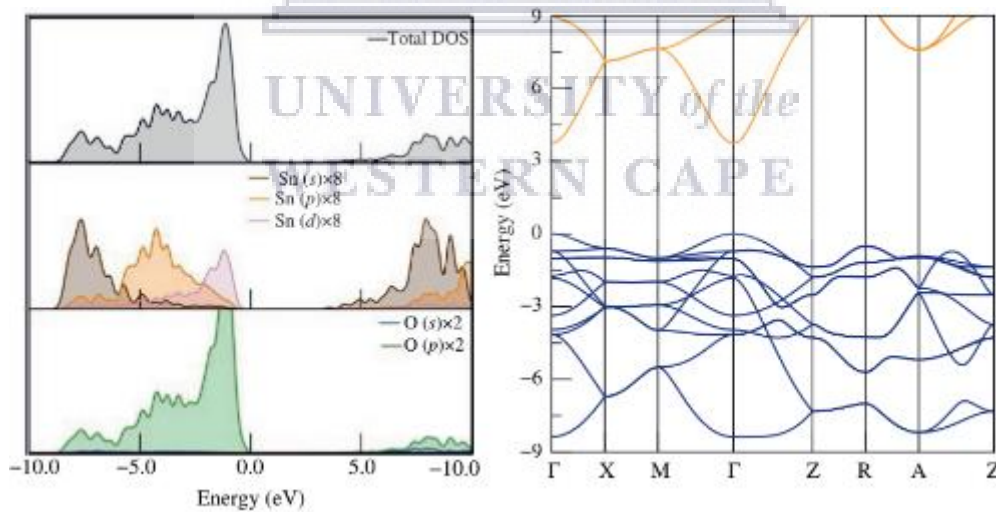


Figure 1.13: DFT calculations for a) density of states (DOS) and b) electronic band structure of SnO₂ [1.37].

For the detection of Sn(II) and Sn(IV) being both concurrently present within a sample, a characteristic decomposition of the $4d^{3/2}$ and $4d^{5/2}$ signals are taken heed of because the anticipated 0.7 eV chemical shift is linked the oxidation state. Another chemical shift is also projected between 0.5 - 0.7 eV for the Sn 3d core levels [1.37]. Discriminating SnO from SnO₂ can be awfully complex. Even though, a shift of the size 0.5 - 0.7 eV associated with the 3d core level between SnO and SnO₂ is expected. There is however, an alternative and more consistent way in which the two tin oxide compounds may be identified from one another [1.3].

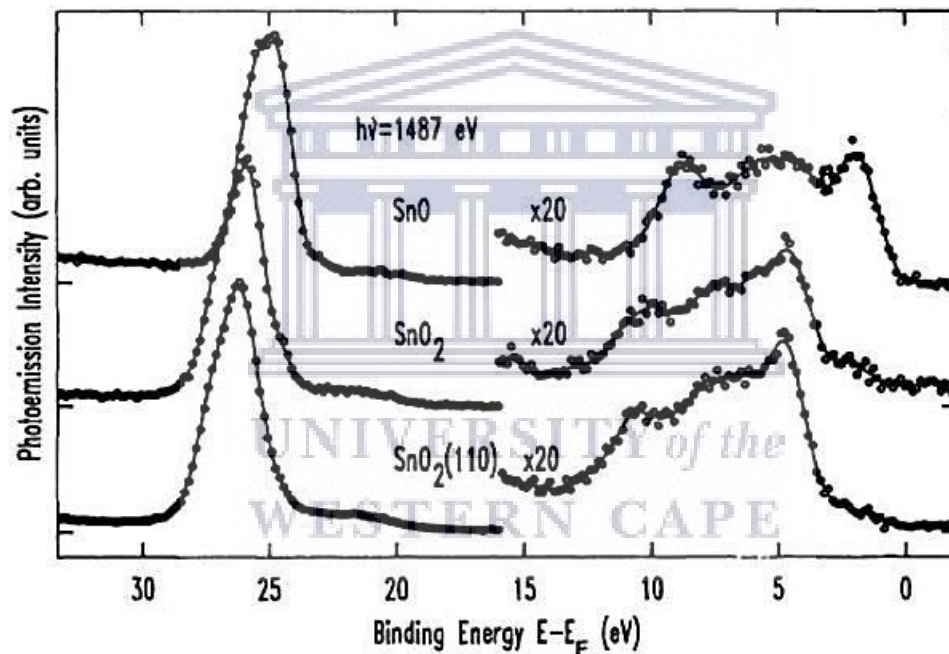


Figure 1.14: Photoelectron spectra of the Sn 4d core level chemical shift of 0.5 eV SnO and two SnO₂ samples given by Batzille et al. [1.3, 1.37].

Distinguishing between SnO and SnO₂ may simply be done by making a comparison between the VB spectra or the energy difference between the Sn $d^{5/2}$ peak and the foremost edge of the VB. The increased energy separation of 22.4 - 23.7 eV belonging to SnO in comparison to that of 21.1 - 21.4 eV for SnO₂ is caused by the smaller band gap relative to that of SnO₂.

SnO is characterized by four labelled peaks A - D in Figure.15 c) shows the total density of states (DOS) belonging to SnO. According to M. Batzill, these four structures labelled from A - D are primarily O 2p states, which are hybridized with Sn-p and Sn-s states. Such that, majority of structure A is consistent with the hybridization with Sn 5s states. Similarly, structure B also has some 5s states, structure C is caused by the hybridization between the O 2p and Sn 5p states, and finally, the D structure corresponds mostly to 5s character states [1.3].

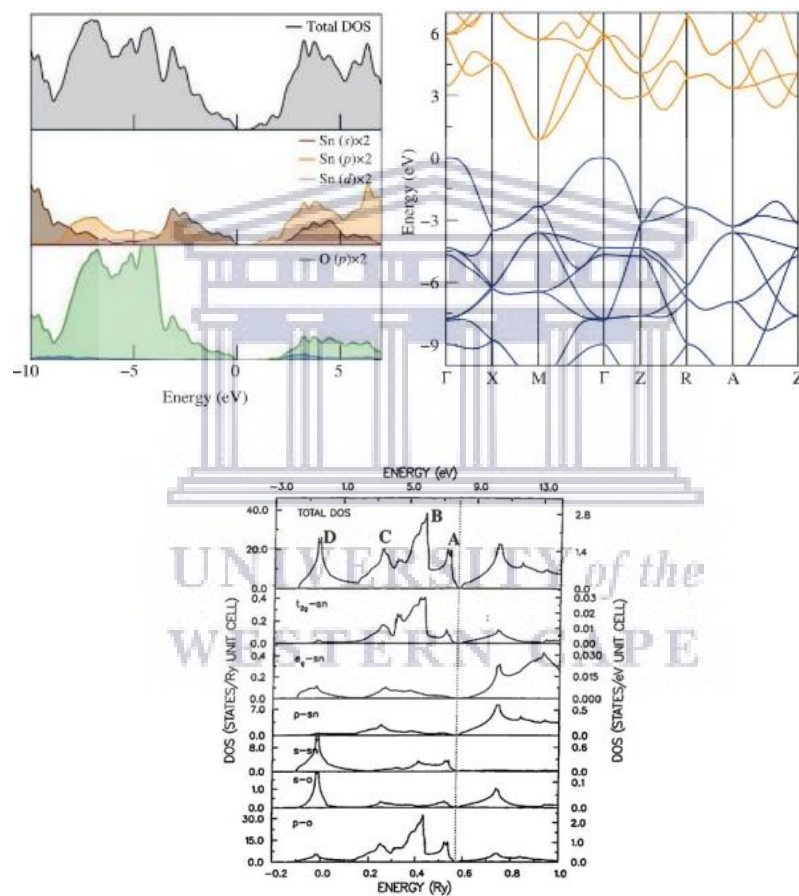


Figure 1.15: DFT calculations for a) density of states (DOS) and b) electronic band structure of SnO provided by Orlandi et al, while c) total density of states given by Batzille et al. illustrating the 4 structures (A, B, C, D) by which SnO can be distinguished from SnO₂ [1.3, 1. 29].

SnO is a metastable p-type semiconductor. Its p-type conductance forms as a consequence of the intrinsic Sn vacancies within the lattice which produce shallow acceptor states. This p-type mobility develops due to the O (2p) - Sn (5s) orbital contribution at the VBM. This behaviour ultimately materializes into the distortion of SnO structure. This distortion triggers a hopping mechanism through lone pairs within interlayer region. The effective mass theoretical values established for the SnO of which belongs to the electron falls within the region of 0.21 - 0.27 m_e , and 2.05 - 2.60 m_e for a hole [1.37].

1.4.3 Electrical Properties

Like many other TCO's, SnO₂ materials are of the n-type variety. As an example of a previous discussion (section 1.2.1) pertaining to how n-type materials are created, SnO₂ compounds of this type are often generated by means of creating oxygen vacancies or cation interstitials, or otherwise, by the interaction with hydrogen and acceptor impurities [1.42].

The electrical conductivity of SnO₂ is related with its intrinsic donor defects. Located in the CB is the fully ionized interstitial tin donor level, while below the CB (within the band gap) at 0.03 and 0.15 eV, the shallow singly ionized oxygen vacancy and deep doubly ionized oxygen vacancy donor levels can be found, respectively. Hence, it is accepted that oxygen vacancies facilitate the electron concentration as a result of the two oxygen donor levels. And therefore, the ionized electrons are then mobile and move freely through the SnO₂ lattice by means of a small-polaron hopping mechanism triggering electron conduction driven by temperature or another compelling force [1.10].

SnO₂ possesses a high charge carrier concentration of magnitudes between 10^{18} - 10^{21} cm⁻³ coupled with high carrier mobilities ranging from 80 - 200 cm²/Vs. These results have been

reported for both single crystal SnO₂ and amorphous SnO_x derivatives of tin oxide, however it is worth noting that the single crystal SnO₂ possesses charge carrier mobilities of a higher standard than that of the amorphous layered SnO_x [1.10].

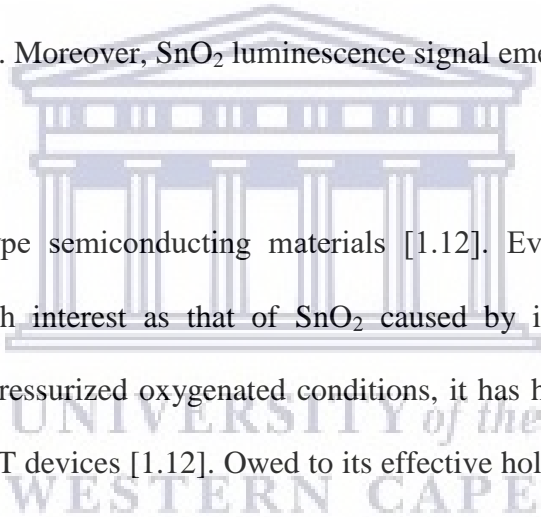
SnO owns an intrinsic p-type conductivity due to the existence of majority tin vacancies caused by its low energy formation and oxygen interstitials present within the lattice. This superior contribution of tin vacancies introduces acceptor defects close to the VBM. SnO materials are also capable of showing n-type conductivity according to experiments that produced nano- and micro- structures manufactured in a reducing synthesis atmosphere. SnO's transparency within the visible region is associated with its direct optical band gap usually between 2.5 - 3.0 eV and to a small indirect band gap of 0.7 eV. This causes a shift of the Fermi level from being close to the VBM towards the CBM by means of element or electrostatic doping, thus supporting the ambipolar effect. Having an exceptional high hole mobility of 6.5 cm² V⁻¹ s⁻¹ and an on/off ratio of > 10⁵, SnO materials are especially good p-type semiconductors since they are proficient enough to operate in ambipolar mode for thin film transistors (TFT's) and complementary metal oxide semiconductor (CMOS) technologies. Contrary to most SMO_x like SnO₂ who's VBM consists of local O 2p orbitals, SnO's VBM however, as previously mentioned has Sn 5s and O 2p orbitals responsible for the hybridized Sn 5s - O 2p states bringing about a high mobility. The ambipolar behaviour of SnO can be understood by studying the SnO's electron configuration [1.42].

The small size of SnO's 0.7 eV fundamental band gap is what makes it a rare p-type semiconductor compared to other p-type semiconductors generally having a fundamental band gap greater than 1.7 eV. The energy variation between the VBM and the vacuum level is referred to as the ionization potential. For SnO, the ionization potential is approximately

5.8 eV (falling in the general range of other p-type materials), and therefore attaining an electron affinity of about 5.8 eV similar to that of n-type semiconductors [1.42].

1.4.4 Optical Properties

As previously stated, SnO₂ is an n-type semiconductor and has an optical band gap also known as the fundamental band gap of about 3.6 - 4.0 eV at the Γ point and is dipole forbidden. From initiating absorption at around 343 nm, as a TCO, SnO₂ is able to reach transparency values of above 80% up till wavelengths of 2000 nm. Thus, including the visible region of the EM spectrum. Moreover, SnO₂ luminescence signal emerges at 350 nm [1.10].



SnO compounds are p-type semiconducting materials [1.12]. Even though, SnO hasn't received as much research interest as that of SnO₂ caused by its metastable nature of converting to SnO₂ high pressurized oxygenated conditions, it has however been used quite frequently as anodes in TFT devices [1.12]. Owing to its effective hole transporting properties as a result of Sn 5s nature at the VBM, its high hole mobility ($2.6 \text{ cm}^2 \text{ V}^{-1} \text{ s}^{-1}$) has proven to be comparatively advantageous over most p-type conductive oxides. This may be improved further by additive dopants to the material. Possessing an indirect band gap of 0.7 eV and a direct band gap typically within the range of 2.5 - 3.0 eV, its large absorption coefficient indicates transmission in the ultraviolet, visible and near infrared regions of the EM spectrum. Liang et al. reported thermally oxidized (at 400 °C for 20 and 40 minutes, respectively) SnO films having a 70% transmission, while others like Sethi et al. have reported an 50% [1.38, 1.21]. In addition, Liang et al.'s SnO thin films exhibited photoluminescence (PL) emission bands around 300 and 450 nm at room temperature [1.21].

1.5 Thermal Oxidation of Metals

Majority of metals are produced by reducing ores. Most ores are metal oxides and are stable under natural environmental conditions. In order for the formation of metal oxide, a certain amount of energy is needed. When metals react with oxygen (O_2), they often return to a more stable state as an ore. In this case smelting may be performed artificially, where corrosion occurs naturally. In dry conditions at a normal temperature around 25 °C, the corrosion rate usually doesn't demonstrate any challenges. However, the same outcome isn't true at elevated temperatures, since the rise in temperature triggers the progression in the corrosion rate. Thermally induced corrosion is generally termed as temperature corrosion or thermal oxidation. The reaction in which a metallic element denoted M undergoes thermal corrosion which ensues in the materialization of a metal oxide M_xO_y , is expressed by the following chemical equation:



Where the change in Gibbs free energy (ΔG) can be determined by the following expression:

$$\Delta G = \Delta G^o + RT \ln \left(\frac{a_{M_xO_y}}{a_{xM} \cdot P_{\frac{y}{2}O_2}} \right) \quad (\text{Eq. 1.12})$$

Such that ΔG^o is the change in standard free energy, R represents the gas constant, T is the absolute temperature, a_α signifies the thermal activity of a species α , while P_{O_2} designates the oxygen partial pressure. Based on the above equation (Eq. 1.12) the following approximations have been understood if:

$\Delta G < 0$; The oxidation reaction given by Eq. 1.11 is active.

$\Delta G = 0$; A state of equilibrium is reached.

$\Delta G > 0$; A reduction reaction is in progress, i.e the reverse reaction from Eq. 1.11.

Under the circumstances where $\Delta G = 0$, the oxygen partial pressure ($\frac{2}{y}P_{O_2}$) is given under the condition where the metal and the oxide is balanced. The partial pressure as outlined by Eq. 1.12 is referred to as the dissociation pressure and is embodied by the following formula:

$$P_{O_2} = \exp\left(\frac{\Delta G^0}{RT}\right) \quad (\text{Eq. 1.13})$$

If oxygen pressure belonging to the atmosphere is greater than that of the dissociation pressure, then metallic oxidation is in progress. Inversely, if the oxygen partial pressure is lower than the dissociation pressure the oxide reduces to metal [1.27].

By considering the reaction listed by Eq. 1.11, in aid of a better understanding of the reaction, an oversimplified practical schematic may be viewed below

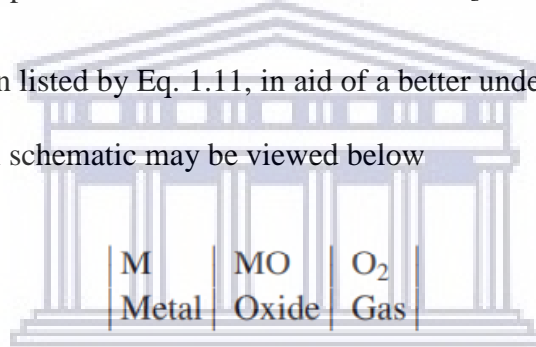


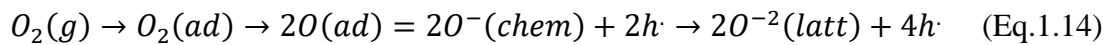
Figure 1.16: An oversimplified illustration of the metal, metal oxide and oxygen gas interfaces [1.4].

Although the schematic presented Figure 1.16 may appear quite straightforward, in order to fully understand the oxidation procedure, it is imperative that one studies the principles pertaining to oxidation mechanism, diffusion process and finally the oxidation rates of the formed metal oxide [1.4].

1.5.1 Mechanisms of Oxidation

When a metal is exposed to an oxidizing atmosphere at a high temperature, it is often assumed that the primary reaction happens at a swift pace thus causing a thin layer to be

formed above the metal substrate. The process in which gas molecules interact with the oxide surface is given by the following equation:



This equation (Eq. 1.14) includes the processes of adsorption, dissociation, chemisorption and finally, ionization of oxygen [1.5].

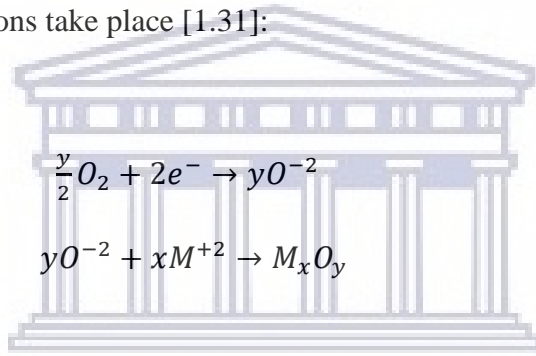
Furthermore, based on the fact that all metal oxides are fundamentally ionic in nature, it is therefore impractical to consider the transport mechanism for metallic oxidation to be via the transportation of neutral metal atoms travelling through the reaction product (MO_x). The transport of ions may be subdivided into two groups, that being of stoichiometric crystals and non – stoichiometric crystals. Fundamentally however, the main concept around the transport mechanism is that of possible defects to some extent in all compounds [1.4].

The main types of defects found in stoichiometric crystal lattices are that of Schottky and Frenkel defects. In a crystal composed of Schottky defects, ionic mobility is executed by existing vacancies within the lattice. In this practice, in order crystal to maintain electroneutrality, it is assumed that an equal amount of cation and anion vacancies are present. Therefore, it is expected that both anions and cations are transportable. In Frenkel defects it is assumed that the anion lattice is perfect, and hence the defect lies within the cationic lattice. In this case cations are mobile, however in order to maintain electroneutrality, the amount of cation vacancies are equal to those of interstitials [1.4].

As informative as these concepts may be, however, it does not sufficiently fully describe the mechanism of thermal oxidation of metals since none of the defect transport processes involves the mobility of electrons. And so, to fully express the metal oxidation system in

practice, a principle involving the transport neutral atoms or ions and electrons is required. It is for this reason that non-stoichiometric compounds seem like the perfect candidates to demonstrate this process. Non-stoichiometric compounds popularly known as semiconductors, and although they show positive and negative behaviour, they are still electrically neutral [1.4].

n-type oxides (semiconductors) operate under metal-excess and oxygen deficit conditions. In these type of semiconductors free mobile interstitial cations M^{+2} and electrons also known as quasi free electrons traverse through the lattice in the direction of the oxide/gas interface, where the following reactions take place [1.31]:



P-type oxides consist of a metal deficit and oxygen excess form of compound. In this case, during oxidation M^{+2} cations are supplied at the metal/oxide interface and subsequently diffuse in the direction of the oxide/gas interface by means of cation vacancies. Furthermore, the positively charged hole travels through the CB, and hence, by means of metal vacancy diffusion ionic mass transfer is possible. The following equations outline these reactions at the metal/oxide and oxide/gas interfaces, respectively [1.31]:



Figure 1.17 exhibits a schematic for n- and p- type oxide lattice crystal semiconductor structures coupled with defects such as point defects, interstitial cations, cation vacancies as well as electron-holes [1.4].

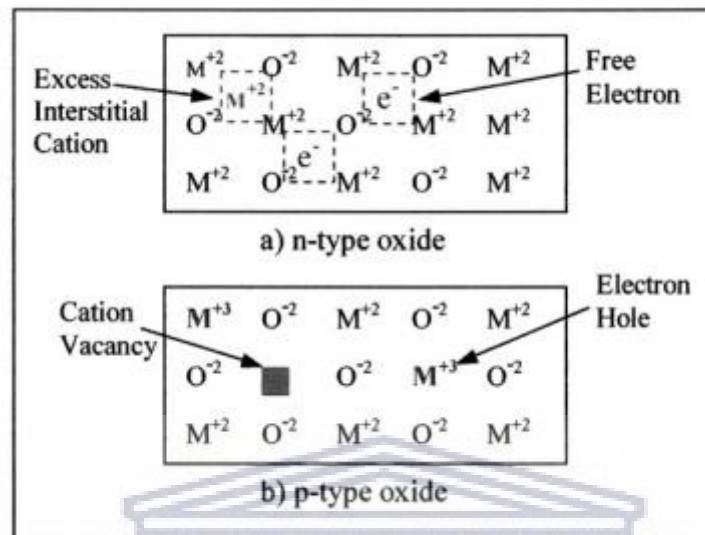


Figure 1.17: Illustration of metal oxide semiconductors [1.31].

Moreover, it is also worth mentioning that another type of oxide does exist whose crystal is close to stoichiometry and exhibits relatively high electrical conductivities irrespective of the oxygen partial pressure. These types of type of materials are named intrinsic or transitional semiconductors. In this instance, the concentration of electron defects surpasses that of ionic defects. As a consequence, an excited electron is elevated to the CB, thus creating a quasi-free electron and leaving behind a hole in the VB. And so, in this way an electron-hole pair is then generated.

1.5.2 Kinetics of Oxidation in metals

When metals are subjected to oxygen rich conditions at increased temperatures, corrosion takes place in form of oxides like n- and p- type non-stoichiometric compounds. The

applications of such materials have attested to be quite useful in a number of electronic devices such as PSC, TFT's and gas sensors. It is for this reason that knowledge pertaining to the rate of the oxide layer growth, the diffusion mechanism, and the extent of protectiveness in the oxide layer is crucial. Figure 1.18 illustrates the behaviour of oxide formation in metals placed under enhanced thermal conditions [1.31].

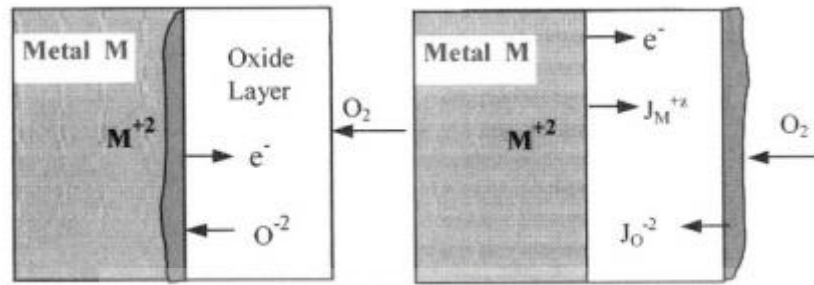


Figure 1.18: Diagram showing the dominant molar flux for a diffusion controlled oxidation process [1.31].

Under thermal corrosive conducive conditions the interaction between metal and oxygen atoms materializes by initially forming a thin M_xO_y film situated at the metal/gas interface. Once a significant thickness of the oxide thin film is reached, it then acts as a barrier which separates or insulates the metallic layer. From here, oxidation proceeds by the diffusion of M^{+2} and O^{-2} species through the oxide film, where the diffusion rate of the properties of the film will vary [1.31].

Anions are only permitted to diffuse through the oxide if metal vacancies are present within the lattice. In the event where O^{-2} anions diffuse at a faster rate than that of the M^{+2} cations throughout the oxide, the diffusion molar flux of such activity is then given as $J_{O^{-2}} > J_{M^{+2}}$. As such an imbalance of diffusion molar flux continues, the oxide proceeds to grow and in doing so the volume of the oxide increases at the metal oxide/gas interface. An illustration of this is

given by Figure 1.16 (a). Once the $V_{M_xO_y} > V_M$, the oxide begins to undergo a high stress concentration resulting in the oxide layer to rupture. Thus, revealing the metal substrate where it may be further oxidised. An example of a metal exhibiting such behaviour is titanium (Ti) [1.31].

Alternatively, if M^{+2} cations diffuse faster than O^{-2} anions, then the diffusion molar flux will then be the reverse of the process shown in Figure 1.16 (a), where anions diffuse faster. In this case, the molar flux will be given as $J_M^{+2} > J_O^{-2}$ displayed in Figure 1.16 (b). Due to this molar flux, an outer layer begins to form at the oxide/gas interface. Unlike the situation displayed by Figure 1.16 (a), in this instance the stress concentration is mitigated and therefore the metal oxide stays attached to the metal substrate. Hence, the metal remains covered and is protected from any further oxidation. An example of a metal which falls in this category is nickel (Ni). The PB ratio is a means by which one is able to identify the degree of how protective a certain metal is [1.31].

In the case where the ionic radius of the anions O^{-2} exceeds those of the divalent cations M^{+2} such that $R_{O^{-2}} > R_{M^{+2}}$, and the anions traversing (diffuse) through the oxide at such a slow rate that it is almost insignificant but cations still continue to diffuse through the oxide, then molar flux in this situation will be that of $J_{O^{-2}} \approx 0$ and $J_{M^{+2}} > 0$. Subsequently if the diffusion rate continues at this pace, the molar flux will eventually slow down until a steady – state of conditions is reached [1.31].

1.5.2.1 The diffusion rate of an oxide scale

Mathematically, the diffusion and mass transfer may be expressed in accordance to Fick's first law of diffusion [1.31]. By the principles outlined by this law, the molar flux is associated to the rate of oxide thickness growth $\left(\frac{dx_t}{dt}\right)$ by the following equations:

$$J = -D \frac{dC}{dx_t} \quad (\text{Eq.1.19})$$

$$J = -C \frac{dx_t}{dt} \quad (\text{Eq.1.20})$$

Where the rate of thickness growth or drift velocity is expressed as:

$$\frac{dx}{dt} = \frac{D}{C_{x_t}} \frac{\Delta C}{x_t} \quad (\text{Eq.1.21})$$

Such that D signifies the diffusivity (diffusion coefficient) in units of $\text{cm}^2 \text{s}^{-1}$, C_{x_t} is the concentration of the diffusive species in ions. cm^{-3} , x_t represents the thickness of the oxide scale expressed in cm or μm and t is the period in which oxidation takes place [1.31].

By integrating Eq. 1.21, the parabolic rate law for thickness is generated as delineated below:

$$x = \sqrt{K_{x_t} t} \quad (\text{Eq.1.22})$$

Where the parabolic rate constant K_x represents:

$$K_{x_t} = \frac{2D\Delta C}{C_{x_t}} \approx 2D \quad (\text{Eq.1.23})$$

When corrosion occurs due to enhanced thermal conditions, most variables involved are temperature dependant. With this said, it is only natural that the diffusivity and parabolic rate law conforms to the principles given by Arrhenius relationship where:

$$D = D_o \exp\left(-\frac{Q_d}{RT}\right) \quad (\text{Eq.1.24})$$

$$K_{x_t} = K_{x_{t_0}} \exp\left(-\frac{Q_d}{RT}\right) \quad (\text{Eq.1.25})$$

In a similar way in which most variables are temperature reliant, so oxide thickness may also be expressed as $x_t=f(T)$ by:

$$x_t = (K_{x_t} t)^n \quad (\text{Eq.1.26})$$

Therefore, the rate in oxide thickness is given as:

$$\frac{dx_t}{dt} = n(K_{x_t})^n t^{n-1} \quad (\text{Eq.1.27})$$

Where the value of the exponent n represents is linked to the diffusive behaviour of the oxide. If n has a value of 1, then a linear rate behaviour is established. At this rate, oxides are described as possessing an non-uniform, porous and cracked structure achieving PB ratios of $1 < \text{PB}$ or $\text{PB} > 2$. Such values describe a non-protective oxide layer, where diffusion progresses via the cracks, pores and vacancies [1.31].

If n is equal to 1/2, then a parabolic rate will be apparent. This rate entails an oxide having a non-porous structure, is adherent properties. Furthermore, this rate describes a protective layer which emerges due to the diffusion mechanism. PB lies within the range of $1 \leq \text{PB} \leq 2$ where the oxide growth associated with metal cations M^{+2} diffusing through the oxide scale towards the oxide/gas interface and reacts with oxygen there [1.31].

If the value of n is given 1/3, then this cubic rate defines properties of a non-porous oxide layer that is adherent and protects the metal substrate from any further oxidation. Hence, the PB ratio value falls within the range of $1 \leq \text{PB} \leq 2$ [1.31].

For thin layers oxidized under fairly low temperature (~ 400 °C), a logarithmic behaviour exists. With regards to logarithmic behaviour where the weight of the oxide formed is given by:

$$W = K_a \log(a_2 + a_3 t) \quad (\text{Eq.1.28})$$

Where K_a is the rate constant (g. cm^{-1}), a_2 signifies dimensionless constant, and a_3 a constant measured in units time^{-1} [1.31].

1.6 Aim

The aim of this study is to find a simplistic and inexpensive way in which SnO_2 thin films may be created. It is common knowledge that SnO_2 films may be prepared by a number of techniques namely: sol-gel dip coating, chemical spray pyrolysis of a precursor solution, molecular beam epitaxy, chemical bath deposition, thermal evaporation. The preferred processing route in this work, however, was that of thermal evaporation of a metallic Sn precursor powder, subsequently followed by the thermal oxidation of the Sn thin films placed under fairly low temperatures in ambient conditions i.e. without the employment on any pure gases at excessive high temperatures.

1.7 Outline of thesis

Chapter 1 outlines the theoretical basis of the study as well as the motivation behind the experimental work. The theoretical basis includes a brief introduction regarding the energy crisis and why renewable energy sources are becoming a necessity. More specifically, a great

amount of detail is focused around photovoltaic technologies such as the emerging perovskite solar cell. Moreover, instabilities associated with the device are listed such as the ETL, where SnO_2 is mentioned as a promising candidate for filling this role (ETL) in the device. In addition, the basic characteristic properties of SnO_2 and SnO are given because during this procedure many derivatives of Sn_xO_y may be formed, but SnO_2 and SnO are the most probable types of Sn_xO_y to develop. Finally, the mechanism of thermal corrosion used to create Sn_xO_y films is discussed in detail.

Chapter 2 highlights the experimental techniques employed to manufacture Sn_xO_y thin films. The initial section delineates the experimental procedures utilized for creating the thin film samples. Sample preparation procedures are given in conjunction with a theoretical background for the instruments exercised. The second part entails a general theoretical background (introduction, theory and working principle) of the characterization techniques used to analyse the thermally oxidized Sn thin film samples. In addition, every characterization technique includes the parameters employed to analyse all thin film samples. This is listed under the “Data Acquisition” section.

Chapter 3 provides a detailed analysis of the results provided by the analytical techniques listed in chapter 2. In this chapter, a thorough investigation of the morphological, structural, vibrational and optical properties will be scrutinized and compared to that of theoretical standards listed by previous studies. A detailed discussion is then followed pertaining to the outcomes of these characteristic properties of the Sn_xO_y thin films.

In chapter 4, well-thought of deduction and conclusion is listed based on the results given by in chapter 3. Based on these outcomes, any future improvements and prospects with regards to the study are provided.



References

- 1.1 Abdelhady, S., Abd-Elhady, M. and Fouad, M. (2017). An Understanding of the Operation of Silicon Photovoltaic Panels. *Energy Procedia*, 113(2017), 466 - 475.
- 1.2 Bagdadee, A. and Zhang, L. (2020). Electrical power crisis solution by the developing renewable energy based power generation expansion. *Energy Reports*, 6(2), 480 - 490.
- 1.3 Batzille, M. and Diebold, U. (2005). The surface and materials science of tin oxide. *Progress in Surface Science*, 79(2005), 47 - 154.
- 1.4 Birks, N., Meier, G. and Pettit, F. (2009). Mechanisms of oxidation. In: Birks, N., Meier, G. and Pettit, F. 2nd Ed. *Introduction to the High-Temperature Oxidation of Metals*. New York: Cambridge University Press, 39 - 74.
- 1.5 Birks, N., Meier, G. and Pettit, F. (2009). Oxidation of pure metals. In: Birks, N., Meier, G. and Pettit, F. 2nd Ed. *Introduction to the High-Temperature Oxidation of Metals*. New York: Cambridge University Press, 75 - 99.
- 1.6 Bhutto, A., Bazmi, A. and Zahedi, G. (2012). Greener energy: Issues and challenges for Pakistan-Solar energy prospective. *Renewable and Sustainable Energy Reviews*, 16(5), 2762 - 2780.
- 1.7 Chevalier, J. (2009). The New Energy Crisis. In: Chevalier, J. 1st Ed. *The New Energy Crisis: Climate, Economics and Geopolitics*. New York: Palgrave Macmillan, 6 - 59.
- 1.8 Coyle, E. D., Grimson, W., Basu, B. and Murphy, M. (2014). Reflections on Energy, Greenhouse Gases, and Carbonaceous Fuels. In: Simmons A, R. and Coyle, D, E. 1st Ed. *Understanding the Global Energy Crisis*. Indiana: Purdue University Press, 1 - 24.

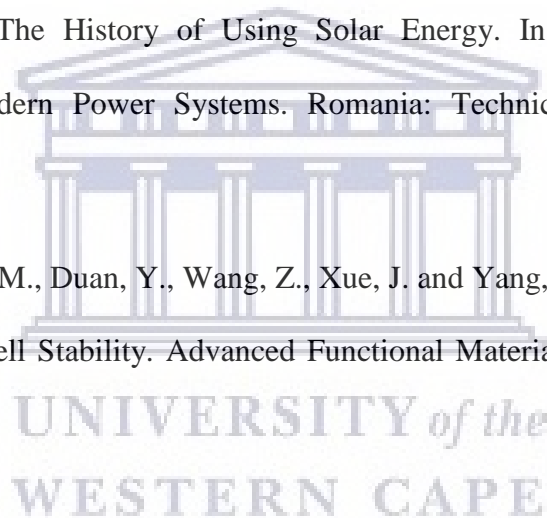
- 1.9 Dou, M. and Persson, C. (2013). Comparative study of rutile and anatase SnO₂ and TiO₂: Band-edge structures, dielectric functions, and polaron effects. *Journal of Applied Physics*, 113(8), 083703(1 - 9).
- 1.10 Henkel, K., Haeberle, J., Müller, K., Janowitz, C., Schmeißer, D. (2018). Preparation, properties and electronic structure of SnO₂. In: Fornari, R. 1st Ed. *Single Crystals of Electronic Materials*. Cambridge: Woodhead Publishing, 547 - 572.
- 1.11 Gul, M., Kotak, Y. and Muneer, T. (2016). Review on recent trend of solar photovoltaic technology. *Energy Exploration & Exploitation*, 34(4), 485 - 526.
- 1.12 Guo, W., Fu, L., Zhang, Y., Zhang, K., Liang, L., Liu, Z., Cao, H. and Pan, X. (2010). Microstructure, optical, and electrical properties of p-type SnO thin films. *Applied Physics Letters*, 96(4), 042113(1 - 3).
- 1.13 Hersch, P. and Zweibel, K. (1982). The Photovoltaic (PV) Effect. In: n.k.n.k. *Basic Photovoltaic Principles and Methods*. Colorado: Solar Energy Research Institution, 9 - 15.
- 1.14 Jiang, Q., Zhang, X. and You, J. (2018). SnO₂: A Wonderful Electron Transport Layer for Perovskite Solar Cells. *Small*, 14(31), 1801154(1 - 14).
- 1.15 Irvine, S. (2017). *Solar Cells and Photovoltaics*. In: Kasap, S. and Capper, P. 2nd Ed. *Springer Handbook Of Electronic And Photonic Materials*. Cham: Springer, 1097 - 1109.
- 1.16 Kalyani, N.T. and Dhoble, S. J. (2018). Empowering the Future With Organic Solar Cell Devices. In: Bhanvase, B. A., Pawade V. B., Dhoble, S. J., Sonawane, S. H., Ashokkumar, M. 1st Ed. *Nanomaterials for Green Energy*. s.l: Elsevier, 325 - 350.

- 1.17 Kibria, M. T. (2015). A Review Comparative studies on different generation solar cells technology. In: Proceedings of 5th International Conference on Environmental Aspects of Bangladesh. Bangladesh: University of Dhaka, 51 - 53.
- 1.18 Le Donne, A., Scaccabarozzi, A., Tombolato, S., Binetti, S., Acciarri, M. and Abboto, A. (2013). Solar Photovoltaics: A Review in Advanced Sciences and Engineering, 2(3), 170 - 178.
- 1.19 Levy, R. (2010). Global Warming. [online] Earthobservatory.nasa.gov. Available at: <https://earthobservatory.nasa.gov/features/GlobalWarming/page5.php> [Accessed 28 August 2020].
- 1.20 Li, J., Wang, Q. and Abate, A. (2019). In: Thomas, S., Sakho E. H. M., Kalarikkal, N., Oluwafemi, O. S. and Wu, J. 1st Ed. Nanomaterials For Solar Cell Applications. Amsterdam: Elsevier, 417 - 440.
- 1.21 Liang, L., Liu, Z., Cao, H. and Pan, X. (2010). Microstructural, Optical, and Electrical Properties of SnO Thin Films Prepared on Quartz via a Two-Step Method. ACS Applied Materials & Interfaces, 2(4), 1060 - 1065.
- 1.22 Luceño-Sánchez, J., Díez-Pascual, A. and Peña Capilla, R. (2019). Materials for Photovoltaics: State of Art and Recent Developments. International Journal of Molecular Sciences, 20(4), 976(1 - 42).
- 1.23 Manieniyam V. (2009). Study on Energy Crisis and the Future of Fossil. In: Conference Proceedings of SHEE. Chidambaram: Annamalai University, 2234 - 3689.

- 1.24 Miles, R., Hynes, K. and Forbes, I. (2005). Photovoltaic solar cells: An overview of state-of-the-art cell development and environmental issues. *Progress in Crystal Growth and Characterization of Materials*, 51(1-3), 1 - 42.
- 1.25 Mishra, A., Singh, V. and Jain, S. (2010). Impact of global warming and climate change on social development. *Journal of Comparative Social Welfare*, 26(2-3), 239 - 260.
- 1.26 Ninad, M. (2018). Perovskites: a complete overview. *International Journal of Advanced Research in Electronics and Communication Engineering*, 7(10), 718 - 723.
- 1.27 Noguchi, M. and Yakuwa, H. (2017). Seminar: Lecture On Fundamental Aspects Of High Temperature Corrosion And Corrosion Protection Part 1: Basic Theory, lecture notes, Ebara Engineering Review 252, Ebara Environmental Plant Co., Ltd., delivered 10/3/2017.
- 1.28 Omer, A. (2009). Energy use and environmental impacts: A general review. *Journal of Renewable and Sustainable Energy*, 1(5), 053101(1– 29).
- 1.29 Orlandi, M. O. (2019). Tin oxide materials. In: Orlandi, M. O. 1st Ed. *Tin Oxide Materials*. Netherlands: Cambridge University Press, 1 - 9.
- 1.30 Our World in Data. (2021). Solar PV Cumulative Capacity. [online] <https://ourworldindata.org/> Available at: <https://ourworldindata.org/grapher/solar-pv-cumulative-capacity> [Accessed 16 April 2021].
- 1.31 Perez, N. (2005) High-temperature Corrosion. In: Perez, N. 1st Ed. *Electrochemistry And Corrosion Science*. Boston: Kluwer Academic Publishers, 301 - 338.

- 1.32 Phillips, L. (2019). Solar energy. In: Letcher, T. 1st Ed. Managing Global Warming. London: Elsevier, 317 - 332.
- 1.33 Powertech, VGB. (2020). Electricity Generation: Facts and Figures, Germany: VGB Powertech.
- 1.34 Psomopoulos, C. S. (2013). Solar Energy: Harvesting the Sun's Energy for Sustainable Future. In: Kauffman, J. and Lee, K. 1st Ed. Handbook of Sustainable Engineering. New York: Intergovernmental Panel on Climate Change, 1065 - 1107.
- 1.35 Rao, C.N.R. (2003). Perovskites. In: Meyers, R. 3rd Ed. Encyclopedia Of Physical Science And Technology. Amsterdam: Elsevier, 707 - 714.
- 1.36 Righini, G. C. and Enrichi, F. (2019). Solar cells' evolution and perspectives: a short review. In: Enrichi, F. and Righini, G. C. 1st Ed. Solar Cells and Light Management: Materials, Strategies and Sustainability. Cambridge: Elsevier Ltd, 1 – 27.
- 1.37 Saviolia, J. Gavina, A., Lucida, A. K. and Watsona, G. W. (2019). The structure and electronic structure of tin oxides. In: Orlandi, M. O. 1st Ed. Tin Oxide Materials. Netherlands: Cambridge University Press, 11 - 39.
- 1.38 Sethi, R., Ahmad, S., Siddiqui, A. and Aziz, A. (2015). Structural, Optical and Electrical Properties of Tin Oxide Thin Films for Application as a Wide Band Gap Semiconductor. In: AIP Conference Proceedings. Longowal: American Institute of Physics, 030039(1 - 6).
- 1.39 Sharma, S., Jain, K. and Sharma, A. (2015). Solar Cells: In Research And Applications – A Review. Materials Sciences and Applications, 6(12), 1145 - 1155.

- 1.40 Shakouri, A., Norton, B. and McNally, H. (2014). Solar Power and the Enabling Role of Nanotechnology. In: Simmons A, R. and Coyle, D, E. 1st Ed. Understanding the Global Energy Crisis. Indiana: Purdue University Press, 125 - 150.
- 1.41 Singh, B. R. and Singh, O. (2012). Study of Impacts of Global Warming on Climate Change: Rise in Sea Level and Disaster Frequency. In: Singh, B. R. 1st Ed. Global Warming: Impacts and Future Perspective. Croatia: InTech Publishing, 93 - 118.
- 1.42 Suman, P. H. (2019). Electrical properties of tin oxide materials. In: Orlandi, M. O. 1st Ed. Tin Oxide Materials. Netherlands: Cambridge University Press, 11 - 39.
- 1.43 Szabó, L. (2018). The History of Using Solar Energy. In: The 7th International Conference on Modern Power Systems. Romania: Technical University of Cluj-Napoca, 1 - 8.
- 1.44 Wang, R., Mujahid, M., Duan, Y., Wang, Z., Xue, J. and Yang, Y. (2019). A Review of Perovskites Solar Cell Stability. *Advanced Functional Materials*, 29(47), 1808843(1 - 25).



CHAPTER 2

EXPERIMENTAL TECHNIQUES

2.1 Introduction

For a material to be considered useful in its application, prior knowledge pertaining to its characteristics are essential. These characteristics of a material are outlined by the synthesis procedure and the conditions thereof. It is for this reason that this chapter provides an extensive and thorough description of the techniques used to make the Sn_xO_y thin films. Section 2.2, offers a full explanation of the steps taken to create such thin films as well as the materials involved. Furthermore, section 2.3 provides an overview of the analytical techniques used to characterise these Sn_xO_y thin films and encompasses a brief description of how data of the films were acquired.

2.2 Sample Preparation

2.2.1 Substrate Preparation

Flourine tin oxide (FTO) and silicone (Si) substrates were meticulously selected for the study of Sn_xO_y thin films to suite every analytical technique requirement. Initially, FTO films of thickness 180 - 200 nm, sheet resistivity $\leq 10 \Omega \cdot \text{sq}^{-1}$, and transmittance, $\geq 79\%$ coated on a single sided polished glass purchased at Techinstro, Ltd., were cut into dimensions of 1×1 cm each. P-type polished single-crystalline (100) Si wafer subtrates of size $100 \times 100 \text{ mm}^2$,

thickness 380 μm , and resistivity ranging from 1 - 10 $\Omega \cdot \text{cm}$ acquired from Saeetra (Pty) Ltd., Pretoria, South Africa, were cut into 1.5 \times 1.5 cm. All substrates were successfully sliced by a diamond cutter on a rigid surface. Thereafter, all substrates were cleaned using two-part solution containing 2% of a hellmanex (III) purchased at Sigma-Aldrich, Inc., and deionized (DI) water (H_2O). Substrates were then placed in isopropanol (IPA) (99.5%), and finally rinsed in deionized (DI) water (H_2O). All cleaning stages were performed in an ultrasonic bath for 10 minutes each. Upon removing substrates from the ultrasonic bath, they were subsequently dried with high-purity nitrogen (N_2) gas. Substrates and fluids used during this procedure were placed in polytetrafluoroethylene (PTFE) Teflon beakers, while Teflon coated stainless steel tweezers handled all substrates to avoid any forms of contamination. Plastic sample holders were then used to protect the substrates from any kind of damage.

2.2.2 The Thermal Evaporation Deposition Chamber

Metallic Sn thin films were deposition by a thermal evaporation deposition chamber procured through VACUTECH and housed in the CADAR lab of the Department of Physics and Astronomy (UWC). A simplified illustration of the system can be viewed in Figure 2.1. Evaporation takes place when a source material is exposed to exceedingly high temperatures of approximately above its melting point within a vacuum chamber. The evaporated atoms then follows a linear trajectory directed towards the wafers ensued by a long mean free-path caused by the vacuum [2.30]. During this process atoms form a vapour flux where these vapour particles ultimately condense on the wafer to form a film [2.14,2.22]. Metal source materials are inserted into a crucible, where they can then either be heated by a resistive heating system, an RF heating system, or an electron beam. The easiest type of evaporation

source is that of a resistively heated system. Heating by a resistive heat source is achieved by passing a large current through a resistive wire or foil encompassing the source material. Well-equipped resistive heating systems often use boats (crucibles) to hold source material instead of a coiled wire because of their convenience. These boats are generally made up from materials being able to withstand high temperatures like tantalum (Ta), tungsten (W), molybdenum (Mo), or ceramic materials. Furthermore, mechanical shutters are set in front of crucibles to control film deposition thickness by being able to start and stop the deposition procedure immediately [2.30].

Wafers are placed into a chamber incorporated with either a diffusion pump, a cryo-pump, or a turbo pump. These pumps are responsible for maintaining a highly-vacuumed state within the chamber. Metal depositions of molten are performed at pressures below 1.33×10^{-2} mbar. Deposition rates as low as $(1 - 3 \text{ \AA s}^{-1})$ are used to produce films of best uniformity [2.30]. On the other hand, deposition rates of such magnitudes require extremely high vacuums. Quartz crystal monitors measure deposition rates through the execution of a resonator plate oscillating at a certain resonance frequency. As additional material is deposited on top of the crystal, a shift of resonance frequency is detected. When enough material has been added, this shift triggers the oscillator causing a more dampened form of resonance. When the output of the frequency measurement system is connected to the mechanical shutters, the thickness of the deposited layers can be managed by regulating the deposition rate. Once the change of thickness is reported back to the crucible temperature, a constant deposition rate may be achieved [2.30].

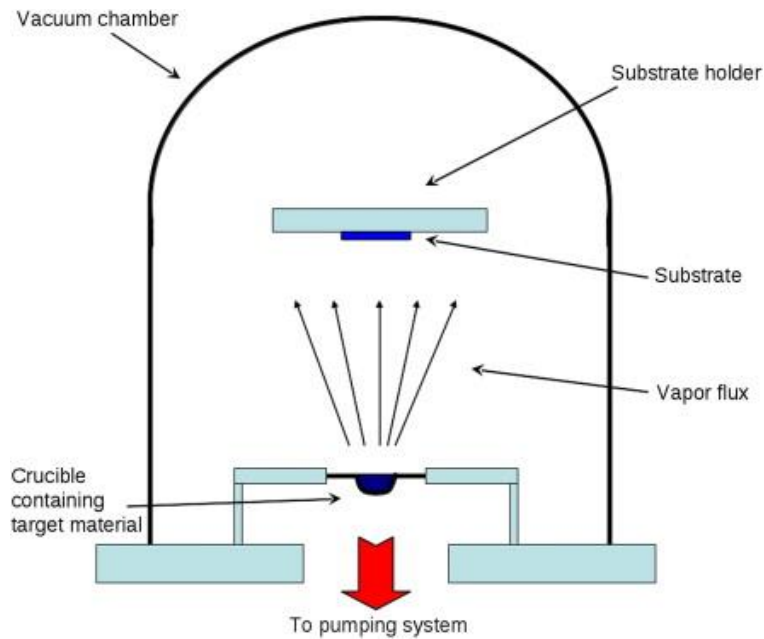


Figure 2.1: Simplified illustration of a thermal evaporation deposition chamber [2.14].

2.2.3 Deposition of Sn thin films

Prior to performing a deposition on both well-refined FTO and Si substrates, a purging of the system was done to eradicate any form of impurities and to avoid contamination of the samples. Once the system was thoroughly cleaned, 10 mg of Sn powder (99.9%) source material obtained through Sigma -Aldrich. Inc, was planted into a tungsten (W) crucible. The crucible connected to the electrodes within the chamber. Samples were then loaded by means of a Kapton tape secured in the centre of a flat metal surface. Once the chamber was sealed, it was allowed to pump down for a time period of ≈ 2.5 hours by means of a turbo pump until finally reaching a base pressure of 10^{-5} mbar. A current ranging between 70 - 75 A was supplied to the two electrodes, thus heating the crucible containing the Sn source material. A temperature ≤ 1000 °C in a deposition pressure of 10^{-4} mbar vapourised the Sn powder allowing this flux of Sn atoms to travel a mean free-path of a 12 cm in distance to both FTO

and Si substrates. 41 nm thick metallic Sn films were deposited at a deposition rate varying between 0.4 - 0.7 Å for a duration of 11.5 minutes.

2.2.4 The Single Tube Furnace System

Sn_xO_y thin films were thermally oxidized by the single tube furnace (see Figure 2.2) purchased at VACUTECH. It is a high temperature vacuum tube furnace capable of annealing samples up to temperatures of 1200 °C depending on the type of tube being used. The furnace has a heating zone length of 20 cm with a maximum heating rate of 10 °C minute⁻¹ and is able to obtain 30 segments of heating and cooling steps with ± 1 °C of accuracy. Settings such as present temperature (PV) and set temperature (SV) are all managed via a Yudian temperature controller (see Figure 2.3). Inside, this instrument is composed of a double steel structure with air cooling, fibrous insulation made up of high purity aluminium oxide (Al_2O_3) for saving energy purposes, a split cover for easy tube replacement and is able to hold tubes of a size in diameter up to ≈ 5 cm. The mullite or quartz tube of a length > 45 cm incorporated within the system is able to reach continuous temperatures of up to 1200 °C and 1100 °C, accordingly. With overall dimensions of 34×30×40 cm in terms of width, length, and height, respectively, and a weight of the furnace is approximately 18 kg. This furnace is compact and convenient for sample use [2.17].



Figure 2.2: Single tube furnace situated in a laboratory at the Physics and Astronomy department (UWC).

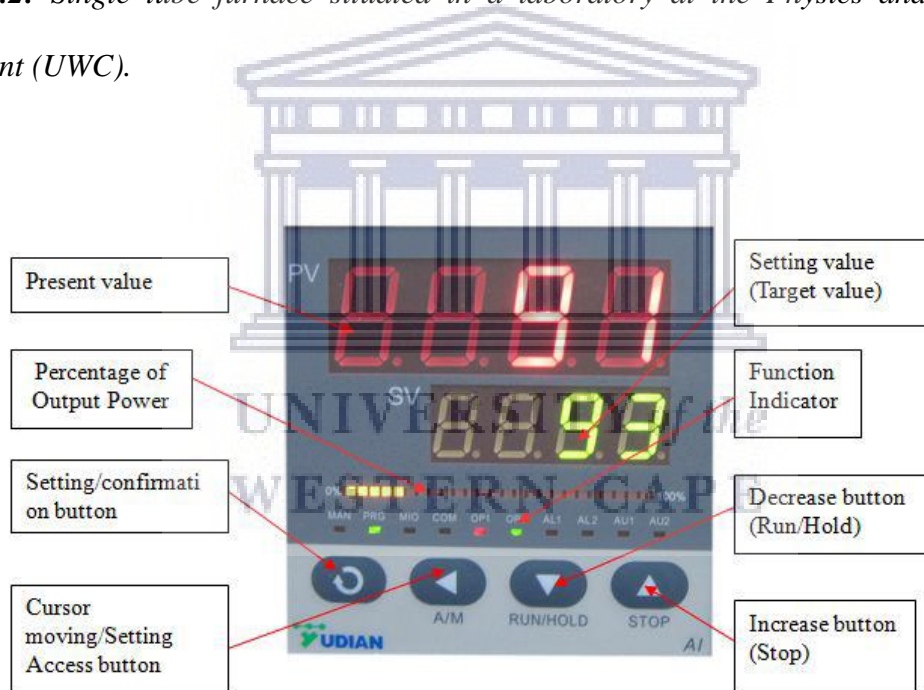


Figure 2.3: Yudian temperature controller with a description of its various settings [2.16].

2.2.5 Thermal Oxidation of Sn thin films

After deposition had taken place, 41 nm thick Sn thin film samples were set to be annealed at temperatures of 200, 250, 300, 350 and 400 °C within the single tube furnace located in a laboratory situated in the Physics and Astronomy department (UWC). Before Sn films were permitted to enter the quartz tube, temperature profiles were deliberated for both Si and FTO substrates at temperatures ranging from 200 - 400 °C, with 50 °C intervals. These temperature profiles are displayed in Figure 2.4 (a) - (e) are in accordance with the temperature profiles established in Figure 2.3. Once a set temperature at point *c2* was reached, samples were then placed at a distance of 22.5 cm (midway) into the quartz tube by a well standardised meter stick. Oxidation was induced by annealing samples in ambient air for 2 hours by allowing oxygen (O₂) molecules in the atmosphere to penetrate the thin film samples, and thereby creating Sn_xO_y bonds. Subsequently, thermally oxidized thin films were naturally cooled in a room temperature of about 25 °C.



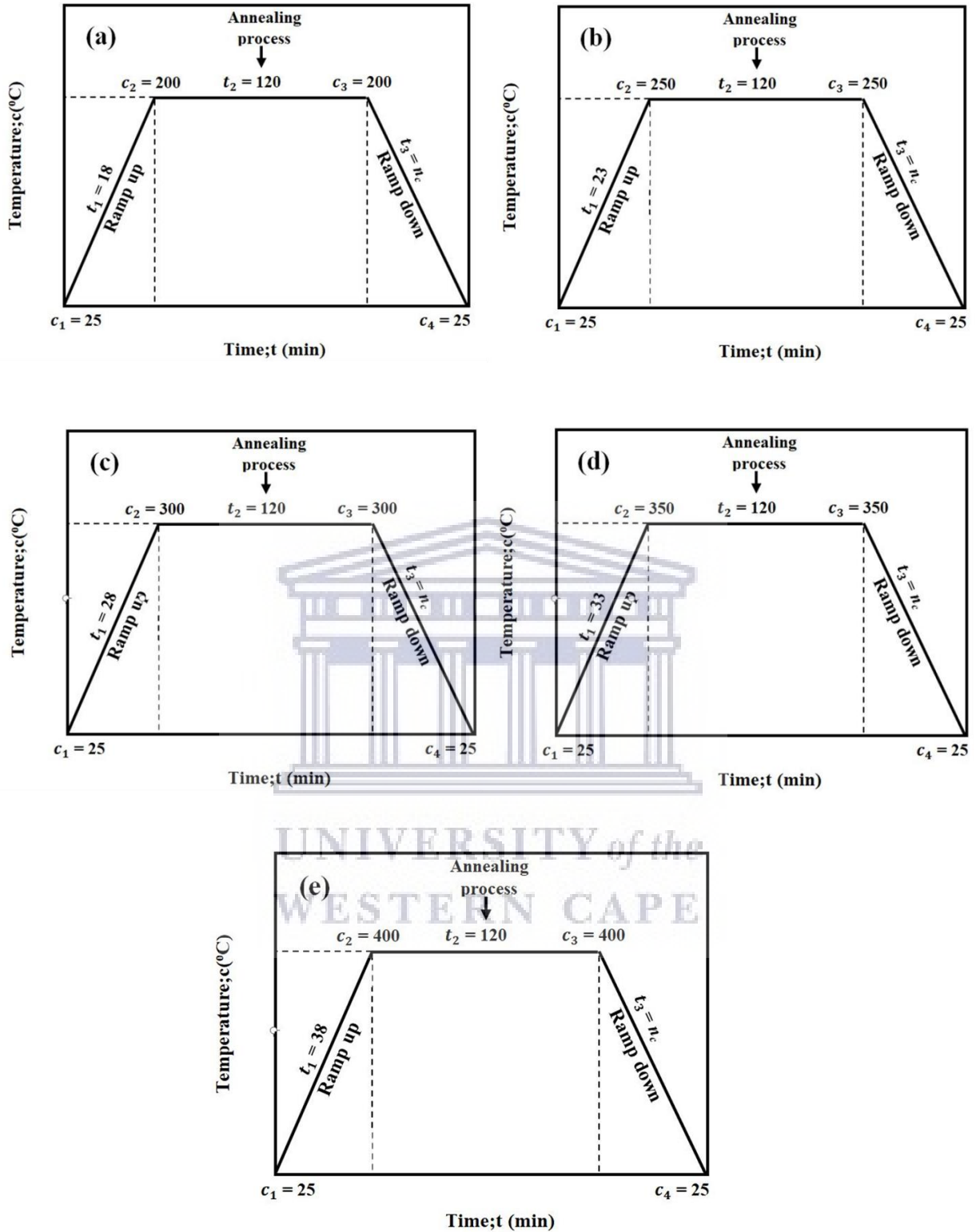


Figure 2.4: Temperature profiles from (a) - (e) for Sn thin films annealed at temperatures of 200, 250, 300, 350 and 400 °C, respectively.

2.3 Analytical Techniques

2.3.1 Scanning Electron Microscopy

2.3.1.1 Introduction

When examining a material, the microstructural morphology and chemical composition are both vital components to consider before using it in an application. The scanning electron microscope (SEM) is one of the most versatile instruments that are able to study these characteristics of a sample. In order to fully comprehend the fundamentals of electron microscopy, it is important to equip oneself with the knowledge of the basic principle of light optics. Zhou et al. states that “Generally, at an optimum viewing distance of 25 cm, the human eye can independently distinguish objects subtending about 1/60 visual angle, in agreement with a resolution of ~ 0.1 mm. Light microscopy obtains a limit resolution of ~ 2000 Å by means of increasing the visual angle through an optic lens.” This is just one of the reasons why light microscopy acts as an imperative study in scientific research. However, electron microscopy has advanced in replacing the light source with a highly energetic electron beam [2.33]. In this section we will discuss the principles and instrumentation of the SEM which was used to analyse the morphology and chemical composition of the Sn_xO_y thin films. This encompasses resolution limitation, electron beam interactions with specimens and instrumentation.

2.3.1.2 Fundamental Principle and Instrumentation

During SEM analysis an electron beam is produced via an electron gun held within a vacuum of 10^{-6} - 10^{-7} Torr for LaB₆ emitters (10^{-9} - 10^{-10} Torr for filed emitters) [2.1]. The purpose of the electron beam is to generate a secure current with an energy that is able to variate between 0.1 - 30 keV. Current energies of such a magnitude are implemented in order to suit the requirements needed evaluate a sample without causing any damage. There are two kinds of electron guns or emission sources which are specifically known as: (1) a thermionic emitter (tungsten (W) or lanthanum hexaboride (LaB₆)) used in the SEM, and (2) a field emitter employed in an FESEM. LaB₆-filaments possess a lower work function of 2.4 eV than that of W-filaments (4.5 eV) [2.33]. Thus, indicating a stronger emission of electrons at certain temperatures, and hence, obtains an elevated brightness of 5 - 10X greater than the conventional W-filament. In addition, LaB₆-filaments also have longer lifetimes and are therefore often preferred. By heating the filament, the work function is overcome and electrons begin to emanate from the source. A negative potential within the range of 0.1 - 30 kV is then applied to both the filament (cathode) and the Wehnelt cylinder, where an electric field drives the electrons towards the anode plate. After passing through the anode, the electron beam diverges. The condenser lenses then converge these electrons belonging to the beam into a collimated and fairly parallel stream [2.33].

The stream then follows a vertical trajectory path through electromagnetic fields to the objective lens. Objective lenses are then used to focus the electron beam into a probe point before it subsequently scans over a particular area of the samples surface. From here, a scan generator controls the deflector coils, which in turn assists the electron beam to raster across the surface of the sample. The rastering pattern is governed by the magnification of the

instrument. So once the magnification changes, the rastered area alters on the sample [2.1]. An illustration of the SEM instrument and a self-biased thermionic electron gun can be observed in Figure 2.5 and Figure 2.6, respectively.

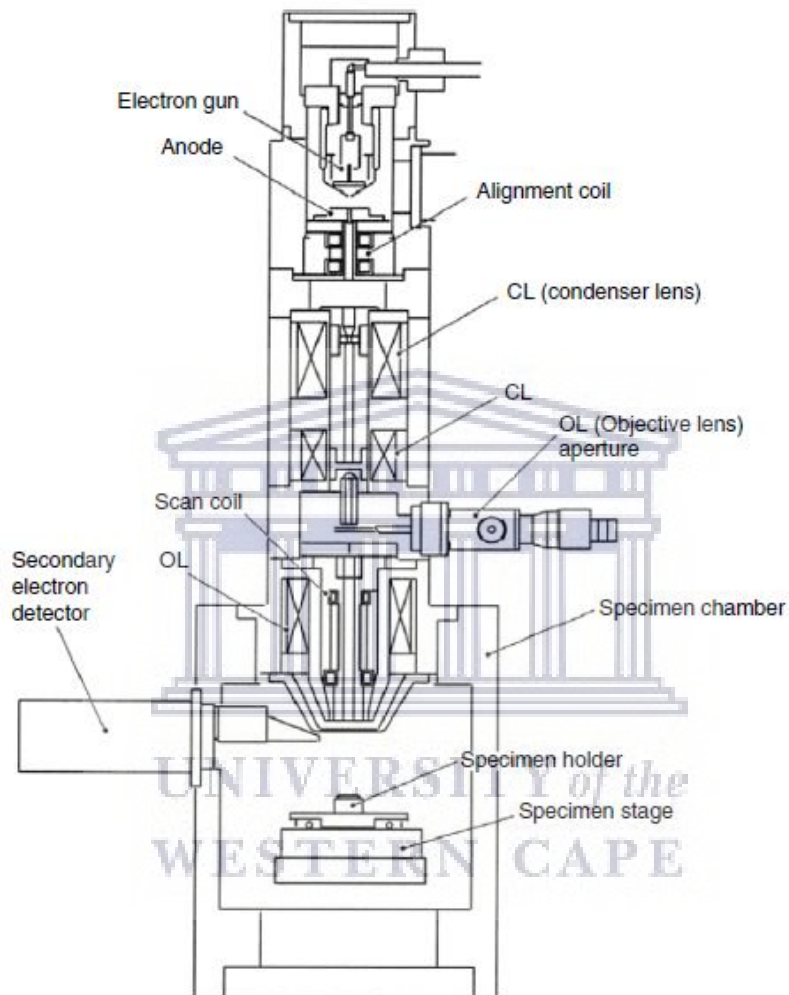


Figure 2.5: Full diagram of the SEM instrument [2.33].

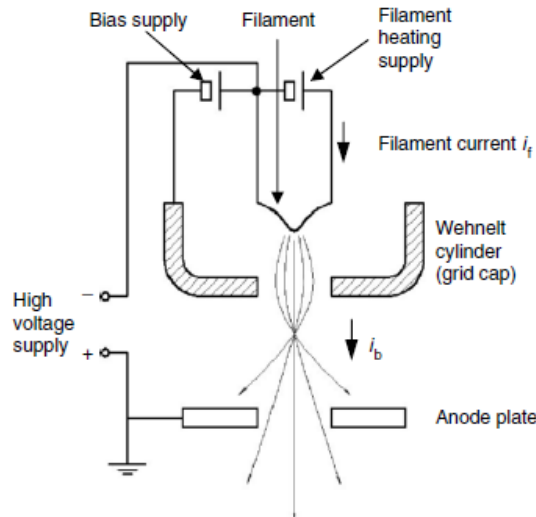


Figure 2.6: Demonstration of a self-biased thermionic electron gun [2.33].

When the electron beams strikes the sample material, vast amounts of signals are given off, more specifically in the form of electrons and x-rays emitted from the sample. These signals are then sensed by detectors accordingly. The various kinds of signals detected are namely: BSE signals which are picked up by solid state BSE detectors. The Everhart-Thornley detector is used for sensing SE's and BSE's. While, energy-dispersive x-ray spectrometers (EDS) and wavelength-dispersive x-ray spectrometers (WDS) are employed for characteristic x-rays signals. Finally, photomultipliers (PMT's) are used for signals in cathodoluminescence. After signals are detected, they are then suitably processed and projected on a CRT screen or camera where a point-to-point image of a scanned area is created (see Figure 2.7). Electron-sample interaction signals provide information pertaining to the external morphology (texture), chemical composition and crystalline structure and orientation of the sample material [2.33].

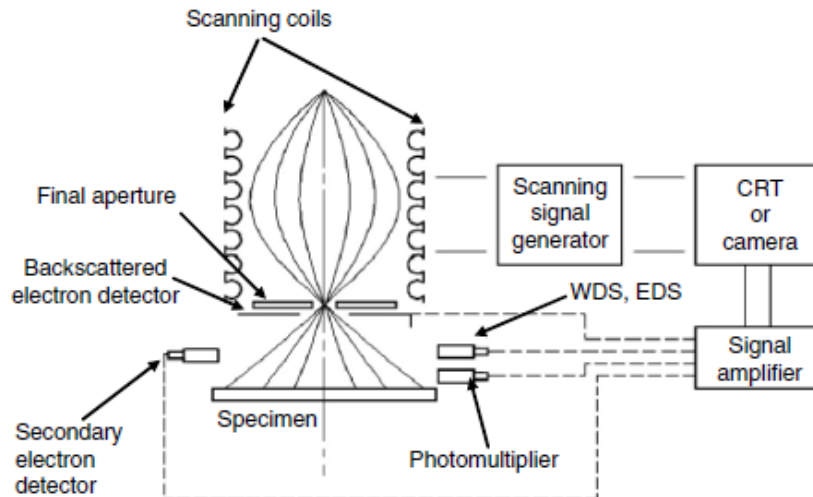


Figure 2.7: Example of the compartments used to form an image in the SEM [2.33].

2.3.1.3 Sample Interaction

When the electron beam interacts with a sample an excitation volume is formed beneath the sample surface. The three factors that influence the depth of the interaction volume are the composition of the solid, the energy of the incident electron, and the incident angle. Every electron that is a constituent of the electron beam comprises of kinetic energy which will ultimately experience energy loss after the scattering process, and as a consequence, will emit a variety of signals.

When an incident electron strikes the sample's surface, the electron is not bounced off instantaneously. Instead, the energetic electrons penetrate into the sample at a certain distance prior to colliding with an atom from the sample. A region of primary excitation is created by the interaction between the primary electron beam and the sample. This region of excitation subsequently gives off a variety of signals that are later picked up by the detector. Features such as the electron beam energy, atomic number, and density plays a crucial role in the size

and shape the primary excitation zone. An increase in beam energy enlarges the volume and depth of penetration. However, an increase in atomic number generates the opposite effect. Atoms which have higher atomic numbers consist of more particles that ultimately prohibits further penetration of electrons.

Furthermore, it should be mentioned that the interaction volume affects the signal acquisition by means of the accelerating voltage. Figure 2.8 displays how high accelerating voltages causes deeper penetration lengths and large primary excitation regions, while low accelerating voltages produces smaller excitation regions. Extreme use of accelerating voltage ultimately results in loss of detailed surface information. Thus, damaging the sample [2.1].

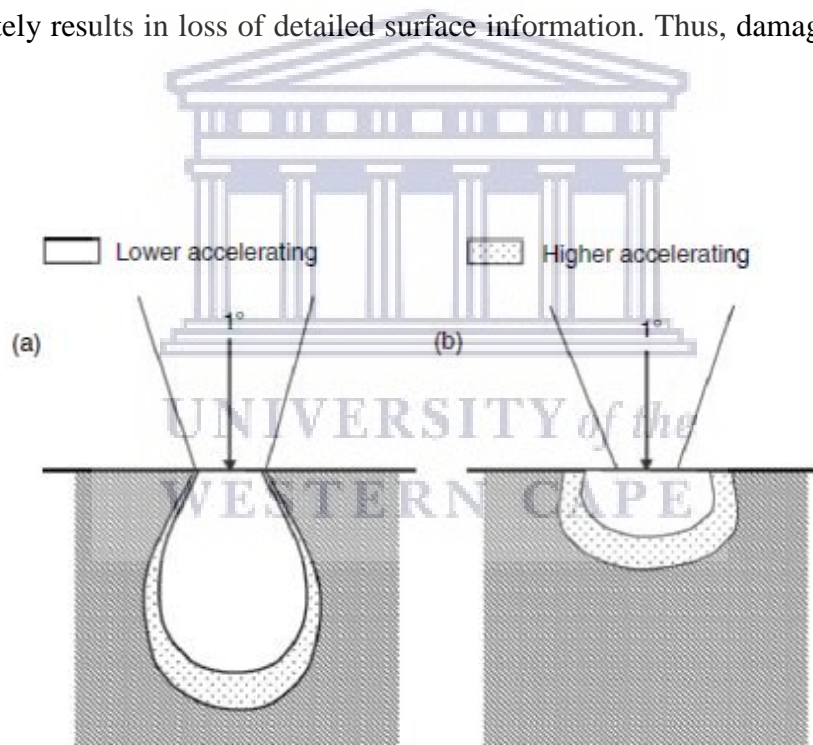


Figure 2.8: Impact of accelerating voltage and atomic number on the primary excitation volume. (a) low atomic number and (b) high atomic number [2.33].

2.3.1.4 Type of Signals

SEM instruments form images based on the type of signals acquired from the interaction between the electron beam and the sample material. These interactions are categorized into two main groups typically referred to as elastic interactions and inelastic interactions. Figure 2.9 and 2.10, shows the various kinds of signals produced by the interaction between a sample and the electron beam [2.33].

2.3.1.4.1 Backscattered Electrons

Elastic scattering occurs when an incident electron is deflected by a nucleus or by an electron from an outer shell possessing a similar energy to that of the nucleus. During this collision, this kind of interaction is typified by its minimal energy loss and wide-angle directional change of the scattered electron. Backscattered electrons (BSE) are incident electrons that elastically scatter through an angle greater than 90° , and in the process gains a reasonable signal used for imaging [2.33].

2.3.1.4.2 Secondary Electrons

Inelastic collisions are caused by a variety of interactions between incident electrons and the electrons belonging atoms within the sample material. As a consequence, the electrons from the primary beam transfers a considerable amount of energy to the atom. The extent of energy loss is dependent on the atom's binding energy and whether the samples electrons are excited singly or collectively. Secondary electrons (SE's) possessing energies of typically $< 50 \text{ eV}$ are given off when a primary electron excites the secondary electrons situated within the

surface atoms within the sample. Additionally, if these excited electrons have enough energy, they eventually cause surface the atoms to become ionized. SE's are used to image or analyse specimens. In addition to these signals, the interaction between the electron and a material are able to create a variety of signals namely: characteristic x-rays, Auger electrons as well as cathodoluminescence [2.1, 2.33]

2.3.1.4.3 Characteristic X-rays

Characteristic x-rays offers information concerning the chemical composition during analysis of the material and is considered to be the most popular microanalytical technique used in the SEM. These kinds of signals are created when an inner shell electron is displaced by the collision with a primary electron. In order to maintain charge balance within the atom and to overcome the ionization, an outer electron shell electron may fall into the inner shell, and thus will emit an x-ray photon. Therefore, causing the atom to return to its ground state [2.33].



2.3.1.4.4 Auger Electrons

Another signal that is able to give elemental composition of a specimen is through the generation of Auger electrons. During this process, the interaction between a primary electron and the atom belonging to the specimen ultimately results in a vacancy within the inner shell of the atom. Following this ionization process, an outer shell electron subsequently fills the inner shell vacancy and releases the characteristic excess energy by an Auger electron. Auger electrons generally consist of low energies and are emitted from near the sample surface, thus only having escape depths of a few nanometres (nm) [2.33].

2.3.1.4.5 Cathodoluminescence

The release of excess energy induced by the collision between a primary electron and a sample can be in the form of a variety of radiations. Certain materials are able to emit excess energy in the form of photons with infrared, visible or ultraviolet wavelengths. In cathodoluminescence the photons are detected and counted via a light pipe and a photomultiplier similar to the ones implemented for the detection of SE's. Images are constructed by means of this method. The best resolution for such images have limit of up to 50 *nm* [2.33].

2.3.1.4.6 Transmission of Electrons

A technique that is readily available with the SEM instrument is the use of transmitted electrons. Transmitted electrons are used to produce images of the sample under the provision that the sample being less than 1 μm thick so that primary beam electrons are able to pass through. Through this method the internal ultrastructure of a thin sample is accessible. Moreover, by means of x-ray microanalysis, transmitted electrons can be used to attain the elemental information as well as distribution of the sample [2.33].

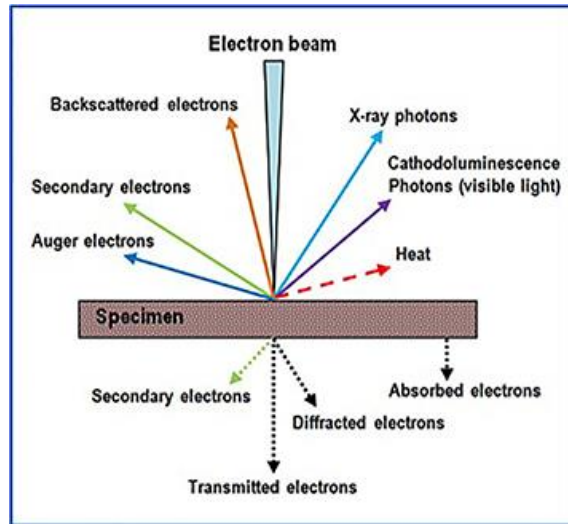


Figure 2.9: Interaction with the electron beam with a sample [2.9].

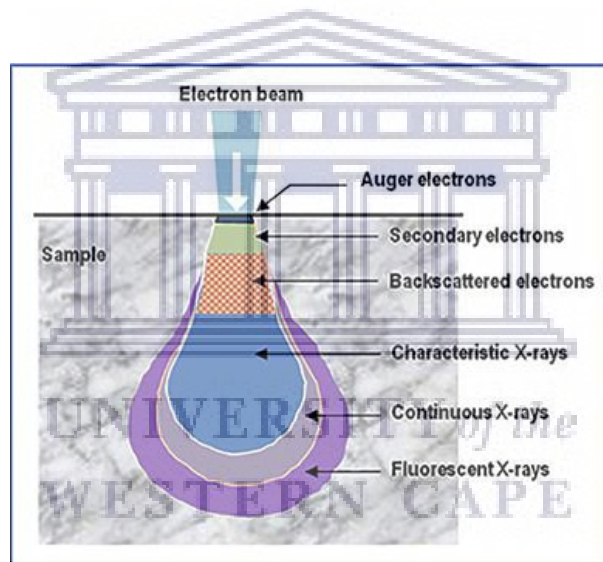


Figure 2.10: Primary excitation volume and the signals generated as a result of the sample and electron beam interaction [2.9].

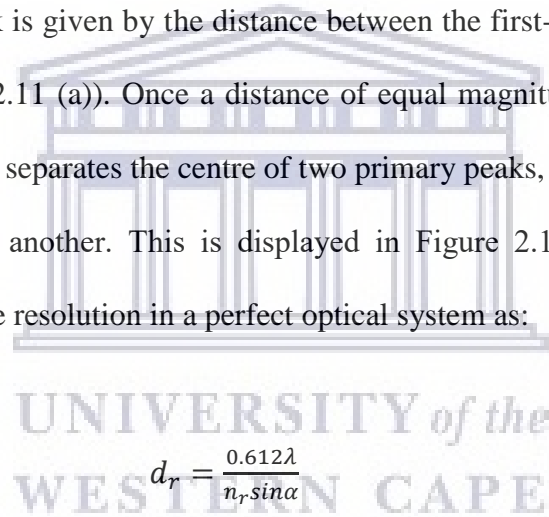
2.3.1.5 Resolution and Abbe's Equation

Zhou et al. states that “The limit of resolution is defined as the two minimum distances by which two structures can be separated and still appear as two distinct objects.” Ernst Abbe

showed that the limit of resolution is influenced by the wavelength of the illumination source such that once the limit of resolution is surpassed at a specific wavelength the magnified image blurs.

When a beam of light focuses on a specific point, the point cannot be focused as a perfect dot caused by interference and diffraction. Instead, the image would appear to have a disk made of concentric circles with a fading intensity with a diameter greater than that of the light source. This is referred to as an Airy disk (illustrated in Figure 2.11 (a)).

The radius of an Airy disk is given by the distance between the first-order peak and the first-order trough (see Figure 2.11 (a)). Once a distance of equal magnitude to that of the radius belonging to the Airy disk separates the centre of two primary peaks, then two objects may be distinguishable from one another. This is displayed in Figure 2.11 (b). Abbe's equation mathematically defines the resolution in a perfect optical system as:



$$d_r = \frac{0.612\lambda}{n_r \sin\alpha} \quad (\text{Eq. 2.1})$$

Given that d_r is the resolution, λ is the wavelength of the imaging radiation and n_r is the index of the refraction of medium between the point source and the lens relative to free space. The half angle of the cone of light i.e. the angle from a specimen plane accepted by the objective is given by α or generally known as the half aperture angle in radians. The numerical aperture is popularly given by the term $n_r \sin\alpha$. By replacing the illumination source and condenser lens with an electron beam, and electromagnetic coils in light microscopes, electron microscopes were discovered [2.33].

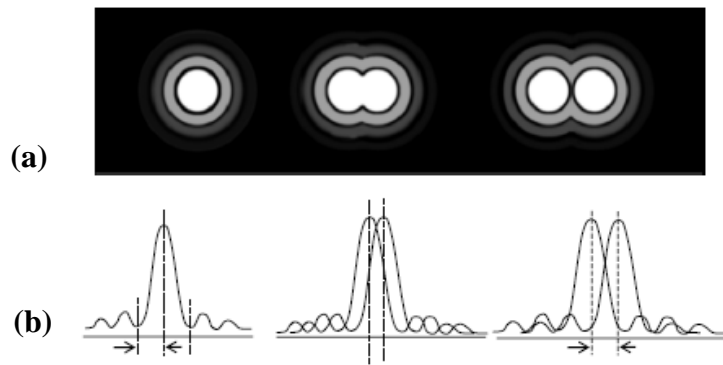


Figure 2.11: Schematic depiction of resolution, where (a) airy disks and (b) wavefronts [2.33].

2.3.1.6 Aperture

Apertures are generally employed for the exclusion of scattered electrons and for the regulation of spherical aberrations in the final lens. The two kinds of apertures in existence are real apertures and virtual apertures. Real apertures are found at the base of the final lens, while the virtual aperture is located in the electron beam on top of the final lens. A virtual aperture is known to restrain the electron beam, but both apertures seem to affect the beam shape and beam edge sharpness. By decreasing the aperture size, the beam angle α will lessen at a given WD. As a result, the increase in the depth of field will diminish the current of the final probe (see Figure 2.12) [2.33].

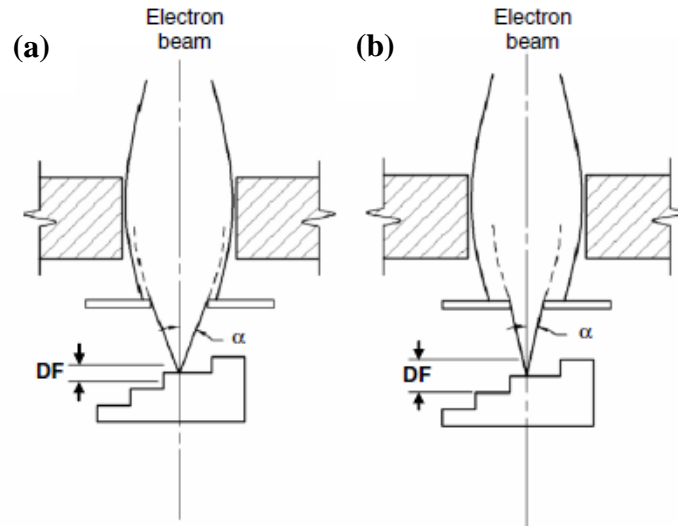


Figure 2.12: Illustration of the effects of a small and large aperture presented by (a) and (b) respectively [2.33].

2.3.1.7 Depth of Field and Working Distance

An image that only displays a section which appears well in focus is referred to as the “depth of field”. The depth of field is reliant on the convergence angle α of the electron beam, such that a smaller convergence angle will result in a larger depth of field. This happens since the change in spot size has less influence along the beam direction for a sharper electron beam. In addition to the aperture size, another factor which has an effect on the depth of field is the working distance (WD). The WD is defined as the distance between the sample surface and the objective lens. This is illustrated in Figure 2.13. A change in WD influences the spread of electrons interacting with sample. By shortening the WD, the sample is scanned with a wide cone of electrons producing an image with a little depth of field. Conversely, at a longer WD, the sample will be scanned with a narrower cone of electrons which results in an increased

depth of field. However, it is important to note that by enlarging the WD the resolution won't necessarily be improved [2.33].

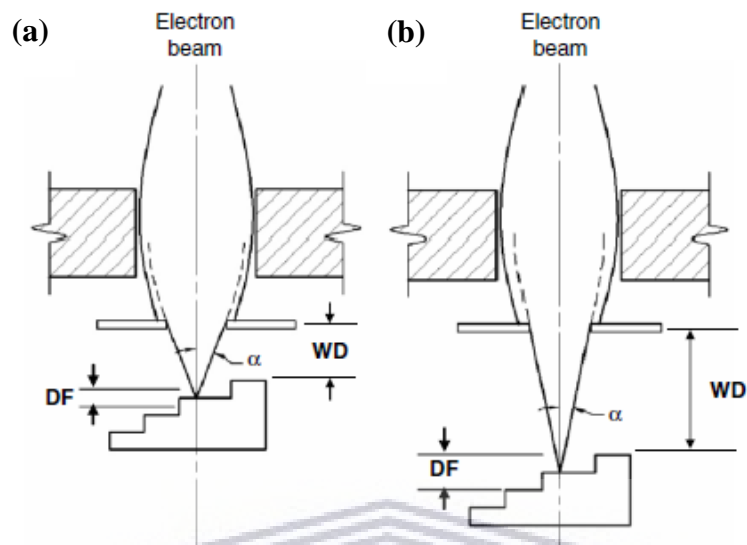


Figure 2.13: Representative model of the relationship between the depth of field and working distance. (a) Short working distance with a decreased depth of field. (b) long working distance with an enhanced depth of field [2.33].

2.3.1.8 Sample Preparation

Before samples are analysed with the SEM instrument, they are loaded onto a specific sample holder where a stub should be secured to effectively contain the sample on the surface. A two-sided carbon tape is commonly used for sticking the sample to the stub. Most nanomaterials can be successfully imaged using the SEM. However, nonconductive materials require a metal coating or some other complicated sample preparation process to avoid overcharging on the sample's surface. Overcharging effects of the sample surface unfortunately presents itself within images with extreme brightness and poor quality. Therefore, non-conductive samples are often sputter coated with a thin layer carbon or a

material that reflects electrons such as gold, silver, gold/palladium, or platinum in the presence of argon gas. Therefore, by coating samples under the aforementioned conditions, the overcharging problem is consequently overcome and samples can then readily be studied [2.1].

2.3.1.9 Data Acquisition

The morphological evolution and chemical composition of Sn_xO_y thin films in relation to varying annealing temperatures were studied by the SEM. All micrographs were scrutinised using Zeiss Auriga field-emission gun scanning electron microscope (FEG-SEM) housed at the National Metrology Institute of South Africa (NMISA) in Pretoria. Micrographs of Sn_xO_y thin films layered on top of FTO substrates were attained with a magnification setting of 50 kX, a WD between 2.1 - 2.5 mm, and an accelerating voltage of 2 kV. Films deposited on Si substrates were taken under a magnification setting of 50 kX, a WD of 3.2 mm and an accelerating voltage of 2 kV. Elemental composition was executed using Electron Dispersive x-ray Spectroscopy (EDS), where analysis was implemented by the Oxford Aztec version 1.2 software and an Oxford X-Max solid-state silicon drift detector (SDD). This was done by the Zeiss Auriga field-emission gun scanning electron microscope (FEG-SEM) situated in the Electron Microscopy Unit (EMU) at the Department of Physics and Astronomy (UWC). All EDS film specifications were performed with an accelerating voltage of 20 kV.

2.3.2 X-ray Diffraction

2.3.2.1 Introduction

X-ray radiation possesses wavelengths of a magnitude roughly between $10 - 10^{-3}$ nm within the electromagnetic spectrum. x-rays are generated when a high voltage with a magnitude of several tens of kV is supplied between two electrodes [2.31]. When an electrically charged particle such as an electron is drawn from the cathode, the electron travels at a high speed toward a metallic target commonly known as the anode. Once electron with a sufficient amount kinetic energy strikes the anode, the electron consequently rapidly decelerates and loses kinetic energy. Continuous x-rays with different wavelengths exist due to the numerous ways in which kinetic energy is lost with regards to electrons. If an electron loses all its energy in one collision, the produced x-ray will attain the maximum energy with the shortest wavelength (λ_{SWL}). Waseda et al. mentions that “The value of the shortest wavelength limit can be estimated from the accelerating voltage V between electrodes.”

$$eV \equiv h\nu_{max} \quad (\text{Eq.2.2})$$

$$\lambda_{SWL} = \frac{c}{\nu_{max}} = \frac{hc}{eV} \quad (\text{Eq.2.3})$$

Where eV is the kinetic energy of the electron e with a charge of 1.602×10^{-19} C, h and c represents Planck's constant and the speed of light respectively, and ν_{max} is the maximum frequency value corresponding to λ_{min} of the λ_{SWL} . However, it is worth mentioning that when a wave is in motion, the corresponding x-ray consists of a frequency lower than ν_{max} , and thus a wavelength longer than λ_{SWL} . The sum of all these wavelengths, of a range longer than the λ_{SWL} , will make-up the continuous spectrum. Moreover, Waseda, et al. also documented that “The total x-ray intensity released in a fixed time interval is equivalent to the area under the

curve.” The intensity related to the atomic number of the material forming anode target denoted as Z , and the tube current i such that:

$$I_{cont} = AiZV^2 \quad (\text{Eq.2.4})$$

Where A is a proportionality constant. For situations where high intensity white x-rays are required, Waseda, et al. recommends that tungsten or gold with atomic number Z should be employed as the target. Additionally, an increased accelerating voltage V and a larger draw current i will assist in the requirement because it correlates to the number of electrons that collide with the target per unit time. It should be noted that during the interaction of electrons with the anode, that most of the kinetic energy is given off as heat and less than 1% is converted into x-rays.

2.3.1.1 Characteristic X-rays

When x-rays are given off, the energy of the photon is equal to the difference in the electron energy levels within the atom. During this process an electron that acquires the adequate amount of kinetic energy ejects an inner-shell electron, thus causing the atom to enter an excited state with a hole in the electron shell. As soon as such a hole is filled by an outer-shell electron, an x-ray gets emitted, and hence the atom will become stabilized once again. Based on the fact that the energy of the produced x-ray is the same as the difference in the energy levels, where such energies are distinctive to certain target metals, these x-rays are unique and are called characteristic x-rays. Another term used for these x-rays are characteristic lines since they are so narrow. These lines correspond to specific subshells referred to as K , L and M and are in accordance to their increasing wavelengths or decreasing energies. As a whole, these lines ultimately form the characteristic spectrum of a certain metal target. For instance

if a molybdenum target is used, the K lines obtain wavelengths of approximately 0.7 \AA , L lines have about 5 \AA , while M lines are even longer. These shells denoted K, L, M, \dots are consistent with the principle numbers $n = 1, 2, 3, \dots$, respectively. Furthermore, if an x-ray is emitted due to the de-excitation of the atom as a result of an electron filling the vacancy in the K shell, this x-ray will then be a characteristic K radiation. This same principle is applied to the other shells L, M, \dots and so forth [2.2] (see Figure 2.14).

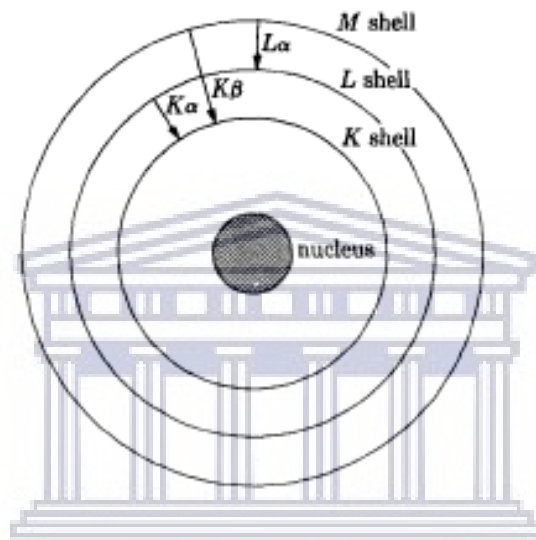


Figure 2.14: Schematic of the electronic transitions within an atom, where the types of characteristic emissions are illustrated by the arrows [2.2].

K lines are commonly used for x-ray diffraction since longer lines are more easily absorbed. There are numerous lines which exist within the K set, however only the three strongest observable lines are made use of. These are called $K\alpha_1, K\alpha_2$ and $K\beta_1$. Since α_1 and α_2 are in such proximity to each other they are often undistinguishable. If they are able to be resolved they are called a doublet, and if resolved they are referred to as a $K\alpha$ line. In the same way, $K\beta_1$ lines are called $K\beta$ lines, where the subscript is omitted [2.2,2.31].

2.3.1.2 Geometry of Crystals

Waseda, et al. states that ““Crystallography” involves the general consideration of how crystals can be built from small units. This corresponds to the infinite repetition of identical structural units (frequently referred to as a unit cell) in space.” To put this more simply, crystal structures can be defined as a lattice with a group of atoms allocated at every lattice point. Crystals are divided into 32 point groups which are based on the eight types of symmetry elements. There are 7 classes of crystal systems, containing 14 kinds of Bravais lattices. This is illustrated in Figure 2.15 for further clarification. Further crystal structure classification can be performed by encompassing the inclusion of space groups, by adding point groups, Bravais lattices, screw axis, and glide reflection axis, there will officially be 230 classified space groups. This means that all crystals belong to one of 230 space groups [2.31].

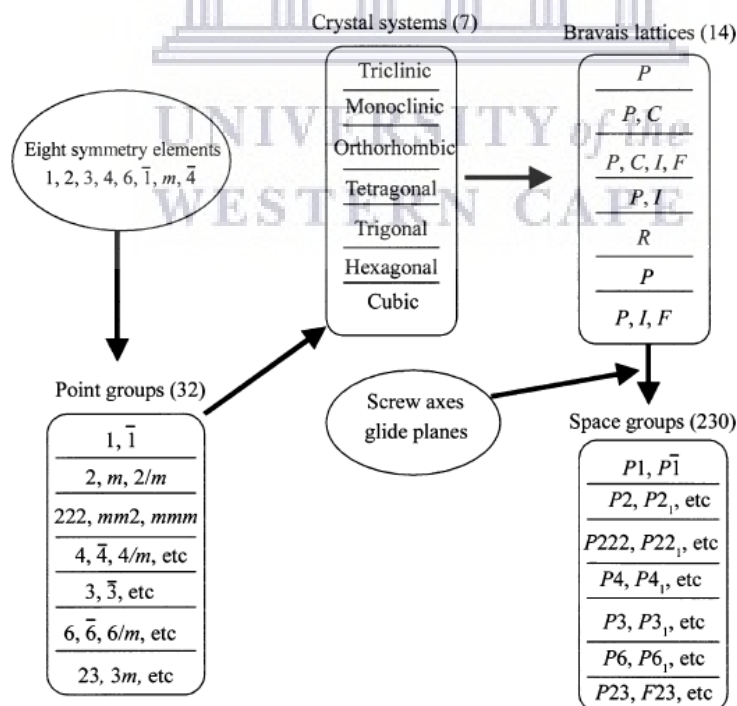


Figure 2.15: Assortment of crystals and how they are classed [2.31].

For example, Figure 2.16 (a) displays a three-dimensional array of points called a point lattice. When a lattice point is used to outline the position or configuration of an atom in a crystal, it can easily be observed that at any point within the lattice the environment remains the same i.e. they all have identical surroundings [2.31]. This indicates that the replication of the lattice is possible through repetition of a small unit called a unit cell. The arrangement of the unit cell is allocated by three translational vectors \vec{a} , \vec{b} and \vec{c} , where the interaxial angles between them are α , β and γ , respectively. Therefore, any position within the lattice denoted \vec{r} given in Eq. 2.5, can be described by these three translational vectors.

$$\vec{r} = n_1\vec{a} + n_2\vec{b} + n_3\vec{c} \quad (\text{Eq 2.5})$$

Where n_1 , n_2 and n_3 are integers. The relation between \vec{a} , \vec{b} and \vec{c} and the angles α , β and γ are known as the lattice parameters (lattice constants) of the unit cell and can be seen in Figure 2.16 (b) [2.18].

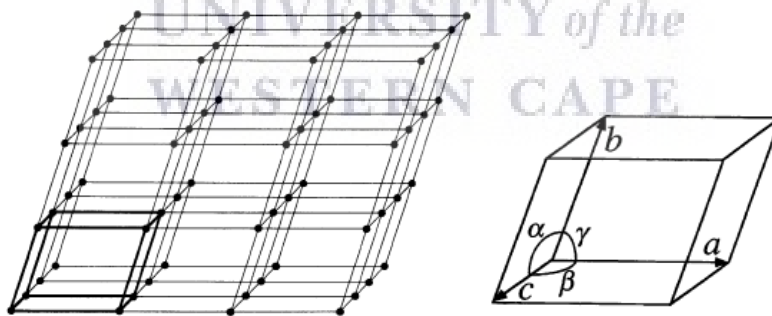
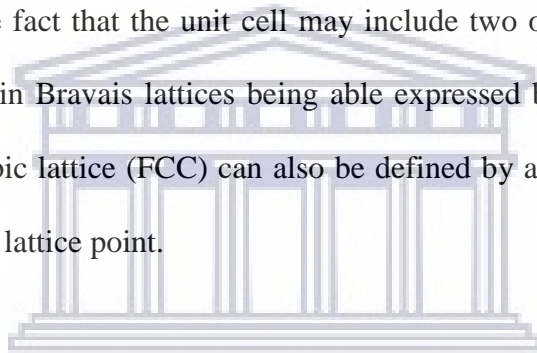


Figure 2.16: (a) Illustration of a three-point lattice. (b) Schematic representation of a unit cell and its lattice parameters [2.2, 2.31].

Bravais lattices and real crystals based upon these structures display various kinds of symmetry. A structure is considered symmetrical when upon applying any of the four macroscopic operations of symmetry (reflection, rotation, inversion and rotatory inversion),

the change in orientation of the lattice seems to leave the atoms unmoved i.e. the arrangement of atoms within the crystal remains constant. The determination of a particular minimum set of symmetry elements is an important property for each crystal system. By applying lattice points to the corners (vertices) of the crystal structure for finding these minimum set of symmetry elements, one is able to differentiate 7 forms of crystal systems. This implies that all possible point lattices or crystals are able to be categorized into one of these 7 crystal systems listed in Table 2.1. On the other hand, there are several other means in which this condition may also be satisfied, such that each point attains identical surroundings. In this manner, the Bravais lattices demonstrates that there are no more than 14 point lattices (see Figure 2.17), based on the fact that the unit cell may include two or more lattice points for convenience. This results in Bravais lattices being able expressed by other simpler lattices, like the face – centred cubic lattice (FCC) can also be defined by a trigonal (rhombohedral) lattice containing only one lattice point.



Lattice symbols such as P, F, I, are assigned to each Bravais lattice according to cells being classed as simple, or primitive represented by P or R, while non-primitive cells are given any other symbol. Primitive cells contain one lattice point per unit cell whereas non-primitive cells have more than one. The F and I symbols are allocated to face-centred and body centred cells accordingly. The symbols A, B, and C are allocated to base-centred cells where the lattice point is located at the centre on one pair of the opposite faces A, B, or C. For example, the face C is defined by the b- and a- axis [2.31].

Table 2.1: Summary of the 7 crystal systems and Bravais lattices [2.31].

System	Axial lengths and angles	Bravais lattice	Lattice symbol
Cubic	Three equal axes at right angles $a = b = c, \alpha = \beta = \gamma = 90^\circ$	Simple	<i>P</i>
		Body-centered	<i>I</i>
		Face-centered	<i>F</i>
Tetragonal	Three axes at right angles, two equals $a = b \neq c, \alpha = \beta = \gamma = 90^\circ$	Simple	<i>P</i>
		Body-centered	<i>I</i>
Orthorhombic	Three unequal axes at right angles $a \neq b \neq c, \alpha = \beta = \gamma = 90^\circ$	Simple	<i>P</i>
		Body-centered	<i>I</i>
		Base-centered	<i>C</i>
		Face-centered	<i>F</i>
Trigonal*	Three equal axes, equally inclined $a = b = c, \alpha = \beta = \gamma \neq 90^\circ$	Simple	<i>R</i>
Hexagonal	Two equal coplanar axes at, 120° third axis at right angles $a = b \neq c, \alpha = \beta = 90^\circ, \gamma = 120^\circ$	Simple	<i>P</i>
Monoclinic	Three unequal axes, one pair not at right angles $a \neq b \neq c,$ $\alpha \neq \gamma = 90^\circ \neq \beta$	Simple	<i>P</i>
		Base-centered	<i>C</i>
Triclinic	Three unequal axes, unequally inclined and none at right angles $a \neq b \neq c, \alpha \neq \beta \neq \gamma \neq 90^\circ$	Simple	<i>P</i>

*Also called rhombohedral.

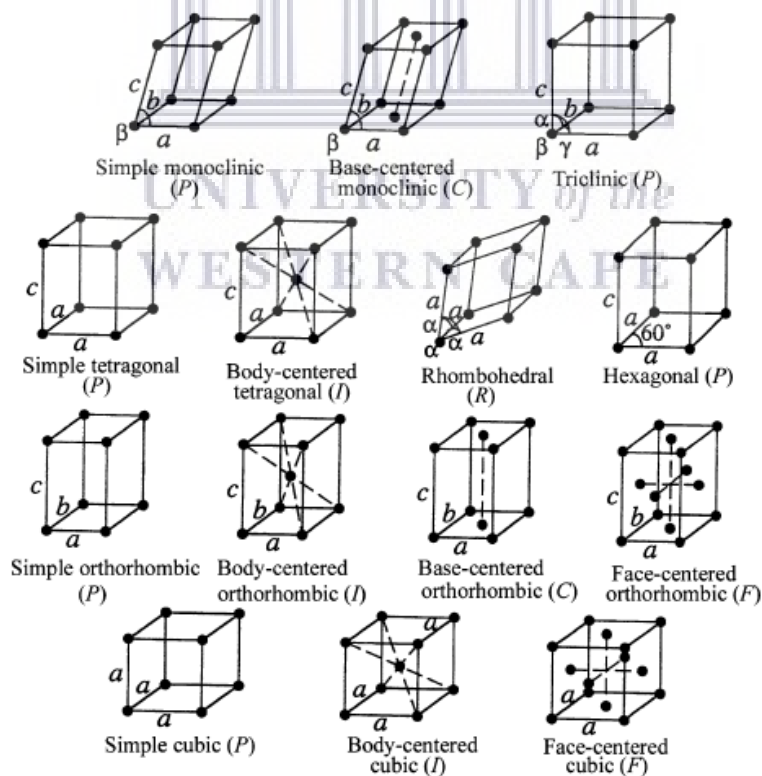


Figure 2.17: The 14 type of Bravais lattices [2.31].

2.3.1.2.1 Lattice Planes and Directions

Lattice planes are indicated by means of Miller indices. According to Waseda et al. Miller indices are given by the reciprocal of the fractional intercepts which a plane makes with the crystallographic axes. For instance, if we consider a plane intersecting the a , b and c axes at $\frac{1}{h}$, $\frac{1}{k}$, and $\frac{1}{l}$ respectively, the miller indices of this plane will be given as $(h k l)$. In the case where a plane is parallel to an axis, this particular index will be given the value of zero. So in accordance with the steps outlined by the Miller indices, the distance from the origin to the axis would be infinite. Even though, it is possible for a set of to be parallel to a specific axis. Miller indices generally refer to the planes closest to the origin. Negative intercepts occur when a plane intersects an axis on its negative side. As such, these values are then indicated by writing a bar over the Miller indices as $(\bar{h} \bar{k} \bar{l})$. Equivalent lattice planes related by symmetry, such as the planes (100) , (010) , $(\bar{1}00)$, $(0\bar{1}0)$, (001) , and $(00\bar{1})$ of a cube are all called “planes of form”. This can also be expressed as $\{001\}$, where the amount of equivalent lattice planes in one plane form is referred to as its multiplicity [2.31].

The direction of a crystal lattice is given by the coordinates $u v w$ on a line passing through the origin such that ua is in the direction of line in the a -axis, vb is in the direction of the b -axis, and finally, wc gives the direction in the c -axis. It should be noted that direction of the line is also expressed by means of the Miller indices technique. So for a line passing through the origin, intersecting the a , b and c axes at $\frac{1}{u}$, $\frac{1}{v}$ and $\frac{1}{w}$, respectively, the indices corresponding to such a line is represented as $[u v w]$. In a similar manner to the planes, the direction of negative indices are written with a bar over the number, for example $[\bar{u} \bar{v} \bar{w}]$, where the equivalent direction by symmetry known as the direction of form is described by $\langle u v w \rangle$ [2.31].

In a hexagonal system, a somewhat different method is employed for the indexing of planes. This technique is called the Miller-Bravais indices which refers to the axes as $(h k i l)$ where $i = -(h + l)$ since the intercepts of a plane on the a_1 and a_2 axes determines the intercept of the a_3 axis [2.2, 2.31]. The index i is defined by the reciprocal of the fractional a_3 axis. In terms of the directions in the hexagonal lattice, the system of four indices $[u v t w]$ is used, where $t = -(u + v)$ [2.31].

2.3.1.2.2 Interplanar Spacing

The interplanar spacing d is a function of both the plane indices $(h k l)$ and the lattice parameters $(a, b, c, \alpha, \beta$ and $\gamma)$, and are related to one another based on the type of crystal system. Table 2.2, displays the relation between interplanar spacing d , plane indices $(h k l)$ and the lattices parameters for various forms of crystal systems [2.2].

Table 2.2: The interplanar spacing for the 7 different crystal systems [2.31].

Cubic	$\frac{1}{d^2} = \frac{h^2+k^2+l^2}{a^2}$
Tetragonal	$\frac{1}{d^2} = \frac{h^2+k^2}{a^2} + \frac{l^2}{c^2}$
Hexagonal	$\frac{1}{d^2} = \frac{4}{3} \left(\frac{h^2+hk+k^2}{a^2} \right) + \frac{l^2}{c^2}$
Trigonal	$\frac{1}{d^2} = \frac{(h^2+k^2+l^2) \sin^2 \alpha + 2(hk+kl+hl)(\cos^2 \alpha - \cos \alpha)}{a^2(1-3 \cos^2 \alpha + 2 \cos^3 \alpha)}$
Orthorhombic	$\frac{1}{d^2} = \frac{h^2}{a^2} + \frac{k^2}{b^2} + \frac{l^2}{c^2}$
Monoclinic	$\frac{1}{d^2} = \frac{1}{\sin^2 \beta} \left(\frac{h^2}{a^2} + \frac{k^2 \sin^2 \beta}{b^2} + \frac{l^2}{c^2} - \frac{2hl \cos \beta}{ac} \right)$
Triclinic	$\frac{1}{d^2} = \frac{1}{V^2} (S_{11}h^2 + S_{22}k^2 + S_{23}k^2 + 2S_{12}hk + 2S_{23}kl + 2S_{13}hl)$

On the triclinic system, V is the volume of a unit cell and the coefficients are given below.

$$S_{11} = b^2c^2 \sin^2 \alpha, \quad S_{12} = abc^2(\cos \alpha \cos \beta - \cos \gamma),$$

$$S_{22} = a^2c^2 \sin^2 \beta, \quad S_{23} = a^2bc(\cos \beta \cos \gamma - \cos \alpha),$$

$$S_{33} = a^2b^2 \sin^2 \gamma, \quad S_{13} = ab^2c(\cos \gamma \cos \alpha - \cos \beta)$$

2.3.1.3 Diffraction from Crystals

X-ray diffraction occurs when an x-ray beam is confronted with a crystal whose atomic arrangement displays a long range of periodicity. The intensity of such x-ray beams are influenced by the arrangement of the atoms as well as the crystal's atomic species. For an x-ray emanating from a crystal comprising of a periodic layout of multiple atoms which has a wavelength exactly equal to that of an incident x-ray initially interacting with the crystal, will most likely be in the form of spherical waves cantering on respective atoms. The phenomena of x-ray diffraction by a crystal is dependent on the phase difference between two or more waves which are attributed to the variation in their path lengths. A deviation in the phase of any two waves is commonly given by the symbol Δ . For two waves that are completely in phase, the value of Δ will be given an integer multiple of wavelength λ . These waves which completely coincide will combine to produce a resultant wave of twice the amplitude to that of the original two. On the other hand, if two waves cancel one another, they will be completely out of phase, giving rise to a value of Δ being $\frac{\lambda}{2}$. These two extremes ($\Delta = \lambda$ and $\Delta = \frac{\lambda}{2}$) are dependent on the direction of the x-ray with respect to the crystal [2.31].

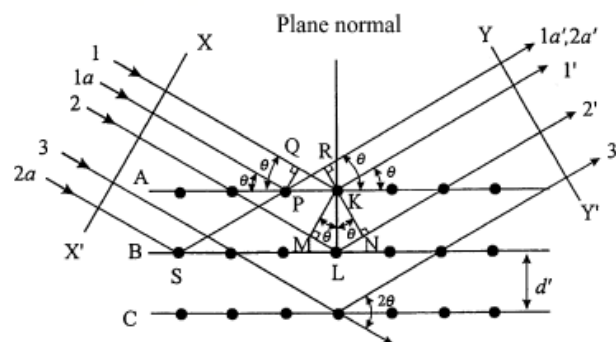


Figure 2.18: Schematic diagram of the diffraction of x-rays by a crystal under conditions of the Bragg law [2.31].

2.3.1.3.1 The Bragg Law

The central aim of x-ray diffraction by crystal is to create a situation in which both the scattered and incident x-rays completely interfere constructively, thus reinforcing each other and causes a detectable diffraction beam. In order to fully grasp the concepts, Waseda et al. suggest that it is important to remember the following geometrical concepts:

1. The angle formed between an incident x-ray beam and the normal to the reflection plane is of the same value to the angle formed between normal and the diffracted x-ray beam. It should also be mentioned that the incident x-ray beam, the normal plane, and the diffracted x-ray beam all reside in the same plane.
2. The diffraction angle, identified as the angle constructed between the diffracted x-ray beam and the transmitted one will always be 2θ .

Once a diffracted x-ray beam is ultimately generated from a crystal as a result of incident x-rays of wavelength (λ) colliding the crystal's atoms arranged in periodic array with an interplanar spacing denoted d' . Then the diffracted beam with an appropriate amount of intensity will only be detected once the condition outlined the Bragg law in Eq 2.8 is met.

$$2d' \sin\theta = n\lambda \quad (\text{Eq.2.8})$$

Where n is the order of reflection.

Diffraction takes place at angles of incidence namely: $\theta_1, \theta_2, \theta_3, \dots$, corresponding to $n = 1, 2, 3, \dots$, if the values of λ and d' are static. In Figure 2.18, the symbols 1', 2' and 3' all signify scattered x-rays emanating from the crystal. For a value of $n = 1$, also known as the first-order of reflection, the path differences between these scattered x-rays will all indicate a certain amount of wavelengths between them. An example of this is that the path difference

between x-rays 1' and 2' is one wavelength, and the path difference between x-rays 1' and 3' are two wavelengths. If the diffracted x-rays coming from all atoms in all the planes are completely in phase with a sufficient amount of intensity, and the direction suits the requirements listed by Bragg's Law, then Eq. 2.8 may be altered in the following manner:

$$2d \sin\theta = \lambda \quad (\text{Eq. 2.9})$$

Such that $d = \frac{d'}{n}$ [2.31].

2.3.1.4 The X-ray Diffractometer

A diffractometer is an instrument that acquires the intensity data of a diffracted x-ray beam as a function of angle in order to satisfy the conditions of the Bragg Law, given that the wavelength of the x-rays are known. This equipment operates with two axes namely: ω and 2θ , whose rotations both function independently. The x-ray source (F), sample holder (S), and a detector (G), are the three major constituents of the diffractometer which are located along the circumference of a circle. This is the focusing circle or the Rowland circle. Rowland circle found in Figure 2.19 is also defined as the circle going through the focal spot target (F), the centre of the diffractometer (S), and the focal point of the diffracted beam (G). In the case where the x-ray source is static and fixed to the 2θ - axis, a powder sample is analysed and placed into a flat-plate sample holder attached to the ω -axis situated in the centre of the diffractometer. Found parallel to the ω - axis is the line focal spot on the target of the x-ray tube. In the process of analysing the sample, the 2θ - axis obtains twice the amount of rotations than that of the ω - axis. For this reason, this procedure is regarded as a “two-theta” scan, and ensures the experimental condition which Waseda, et al. states that “the

direction of normal to the sample plane should be fit to the direction of the scattering vector $\vec{q} = \vec{s} - \vec{s}_0$ defined by the difference between vector \vec{s}_0 of the incident x-ray beam and the vectors of the diffracted x-ray beam \vec{s} .

Slit systems are implemented into the x-ray path in order to lessen the angular dispersion, and to mutually enhance spatial resolution for both the incident and diffracted x-ray beam. A soller slit is made up of multiple thin plates closely spaced parallel to the plane of the diffractometer circle. This slit is employed to limit the perpendicular dispersion of incident x-ray beam, as well as the diffracted x-ray beam. Slits such as the divergent slits (DS) and the scattering slits (SS) as depicted in Figure 2.19, limits every horizontal dispersion made by the incident and the diffracted x-ray beams. The receiving slit (RS), situated in front of the detector then regulates the spatial resolution. This collimating and focusing interaction between these slits are called para-focusing. The fact the RS is located in front of the detector as seen in Figure 2.19, which matches with a para-focusing spot in the diffractometer, ensures that the intensity measurement is effective and improves the spatial resolution [2.31].

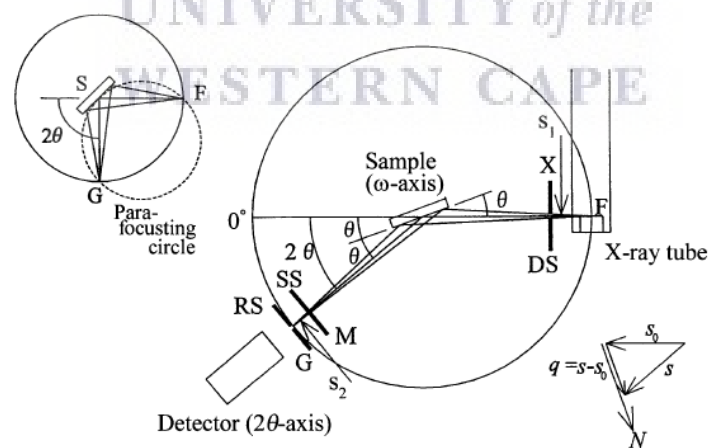


Figure 2.19: The fundamental layout of an x-ray diffractometer and para-focusing geometry [2.31].

2.3.1.5 Data Acquisition

All XRD data regarding the oxidised Sn thin films were obtained through An Empyrean XRD system from PANalytical at the National Metrology Institute of South Africa (NMISA) in Pretoria (see Figure 2.20). A Cu K-alpha 1 ($Cu K\alpha_1$) of wavelength 1.5406 Å x-ray radiation source was used to ensure a continuous scan of the range $2\theta = 10 - 100^\circ$, in steps of 0.02° was performed. The experiment proceeded with a supplied voltage of 45 kV and a tube current of 40 mA. A fixed divergence slit of the size 0.76 mm was used on both FTO ($1 \times 1 \text{ cm}^2$) and Si ($1.5 \times 1.5 \text{ cm}^2$) substrates layered with Sn_xO_y films. The PANalytical X'PERT Data Collector and X'PERT HighScore software were ultimately used to analyse all data, and in doing so was able to identify crucial crystallographic information pertaining to the sample. Information such as interplanar spacing (d), peaks position 2θ and FWHM values are effortlessly obtained. Peak positions were indexed by means of a data base listed in the software, while lattice constants (a , b and c) are computed reorganising interplanar spacing equations listed in Table 2.2, according to the 7 different crystal lattices. XRD patterns were produced using the OriginPro 8.5.1 software [2.23].



Figure 2.20: The Empyrean XRD system from PANalytical at the National Metrology Institute of South Africa (NMISA) in Pretoria [2.23].

2.3.3 Fourier Transform Infrared Spectroscopy

2.3.3.1 Introduction

Infrared (IR) spectroscopy is based on the interaction between electromagnetic radiation and the natural vibrations of the atoms of a molecule [2.24, 2.27, 2.7]. An IR spectrum is obtained once IR radiation is passed through a sample, and the fraction of incident radiation absorbed at a particular energy. The energy corresponding to any peak in an absorption spectrum, correlates with the frequency of a molecule's vibration from the sample [2.24]. Molecules are only able to absorb radiation once the infrared radiation is of an identical frequency as one of the fundamental modes of vibration of the molecule. This means that a small part of the molecule's vibrational motion is increased and while the remainder of the molecule is left unaffected [2.24].

The term "Fourier spectroscopy" describes the analysis of any varying signal into constituent frequent components. The term was named after the mathematical method created by J.B.J Fourier. Fourier transforms has proven to be useful in not only in fourier transform infrared spectroscopy (FTIR), but in a number of spectroscopic techniques such as nuclear magnetic resonance spectroscopy (NMR) and electron spin resonance spectroscopy (ESR) [2.10]. FTIR spectrosopes are able to identify functional groups within materials in various phases namely: gasses, liquids and solids [2.11].

2.3.3.2 The Electromagnetic spectrum

Electromagnetic radiation are all considered to have a dual nature as a stream of particles (photons) or as an electromagnetic wave travelling at the speed of light in a vacuum [21,30].

In the case of a photon, the interaction between photons and molecules behaviour may be described by the laws of quantum optics. While as an electromagnetic wave, the interaction of an electromagnetic wave with a medium is described by the electromagnetic theory using Maxwell's equations.

In the former case, the energy of a photon is given as:

$$E = h\nu \quad (\text{Eq. 2.14})$$

Where h is the Planck constants ($h = 6.626 \times 10^{-34}$ J. s) and ν is the frequency of light. The velocity of light in a vacuum c ($c = 3 \times 10^8$ m. s⁻¹) and wavelength λ are related by:

$$\nu = \frac{c}{\lambda} \quad (\text{Eq. 2.15})$$

Therefore, it can be deduced that the energy of the electromagnetic wave is directly proportional to the reciprocal of the wavelength. Vibrational spectroscopy often makes use of the reciprocal wavelength denoted $\bar{\nu}$ (wavenumber). The energy of the electromagnetic wave in (Eq. 2.14) can then be written as:

$$E = hc \cdot \bar{\nu} \quad (\text{Eq.2.16})$$

Generally, the wavenumber $\bar{\nu}$ is written in the form:

$$\bar{\nu} [cm^{-1}] = \frac{1000}{\lambda[\mu m]} \quad (\text{Eq.2.17})$$

The second case describes light as an electromagnetic wave. In this situation, the propagation of light may then be expressed as:

$$A(\varphi) = A_0(\varphi)e^{i(\omega t - \delta)} \quad (\text{Eq.2.18})$$

Where A is the amplitude, ω the circular frequency, t is the time, δ is the phase angle and φ is the polarization angle. The circular frequency may be related to the wavelength λ and the refractive index n :

$$\omega = \frac{c}{\lambda n} \quad (\text{Eq.2.19})$$

For the propagation of light through an absorbing medium Eq. 2.19 is adjusted by replacing the refractive index n by its complex value n^* such that:

$$n^* = n + ik \quad (\text{Eq.2.20})$$

where n and k are always non-negative. For an absorbing medium, the absorption coefficient α is often used.

$$\alpha = \frac{4\pi k}{\lambda} \quad (\text{Eq.2.21})$$

From Eq. 2.18 the light intensity denoted I , can now be described as:

$$I = I_0 e^{-\epsilon c l} \quad (\text{Eq.2.22})$$

where ϵ is the molar absorption coefficient and c the concentration of the absorbing compound. In the logarithmic form Eq. 2.22 can be expressed as:

$$\log\left(\frac{I_0}{I}\right) = A = \epsilon c l \quad (\text{Eq.2.23})$$

This is known as the Beer-Lambert law. It is important to note that the absolute value of ϵ changes by a factor of 2.303 if the function “log” is replaced by “ln”. When light is absorbed by a medium, it causes a transition from an energetic ground state to an excited state. Excited states may differ depending on the energy of the light absorbed or the chemical nature of the interacting compound as displayed in Figure 2.21. Rotations and vibrations are excited in the spectral infrared range [2.28].

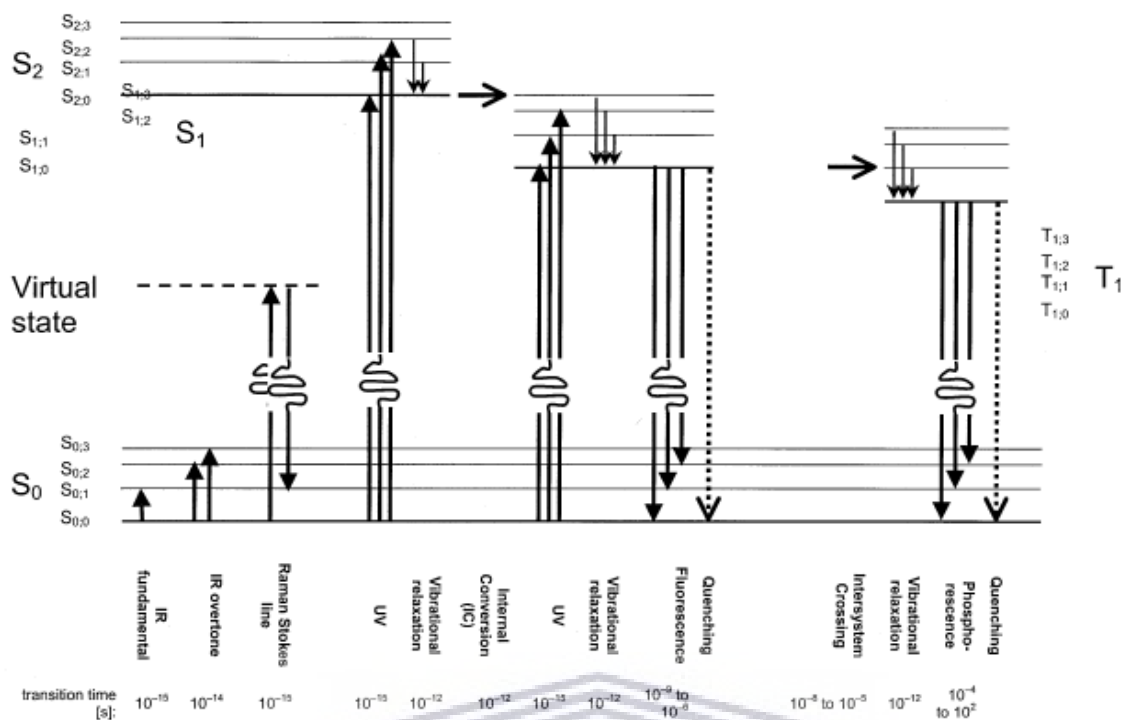
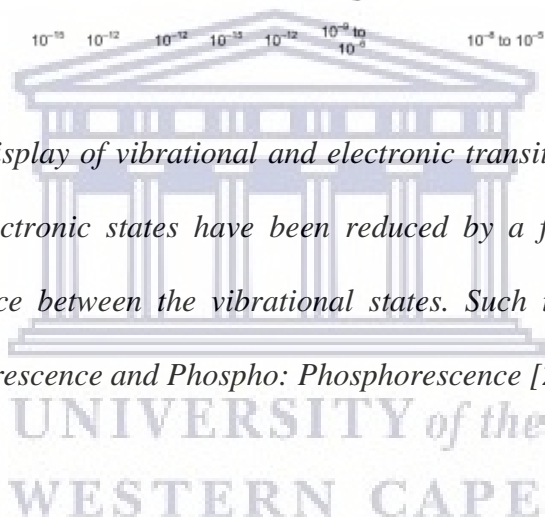


Figure 2.21: Schematic display of vibrational and electronic transitions. It should be noted that distance between electronic states have been reduced by a factor of at least 10 in comparison to the distance between the vibrational states. Such that fund: fundamental; harm: overtone; fluo: fluorescence and Phospho: Phosphorescence [2.28].



2.3.3.3 Infrared Absorption

The IR region lies between the visible and the microwave end of the electromagnetic radiation spectrum. The IR region is parted into three main portions mainly the near-infrared (NIR) in the range of $\lambda = 14000 - 4000 \text{ cm}^{-1}$, the mid-infrared (MIR) in the range of $\lambda = 4000 - 400 \text{ cm}^{-1}$, and finally, the far-infrared (FIR) within the range of $\lambda = 1400 - 40 \text{ cm}^{-1}$. IR spectroscopy is used to investigate the structural chemistry with IR radiations. During this process, the sample, or more specifically molecules which makeup the sample, absorb the IR radiation and the intensities of these absorbed radiations is then consequently displayed by an

absorption spectrum. These absorbed infrared radiations trigger a variety of molecular motions within the molecule and thus generates a dipole moment. When a molecule is able to obtain a net dipole moment it is said to be IR active. Conversely, if a molecule has no net dipole moment it is IR inactive [2.15, 2.24]. Before a molecule can absorb IR radiation two necessary conditions needs to be met. The first condition states that the molecule must have a vibration during which a change in dipole moment occurs with respect a distance being non-zero. This statement can be given as an equation by the following:

$$\frac{\partial\mu}{\partial x} \neq 0 \quad (\text{Eq.2.24})$$

Where $\partial\mu$ is the change in dipole moment and ∂x represents the change in distance. Vibrations that fulfil the expression above (Eq.2.24) are IR active. The second essential condition for IR absorbance is that the energy of the light which interacts with the molecule must be equal to the vibrational energy level difference within the molecule. As an equation, this is expressed in Eq. 2.14 [2.26]. When this condition is not met, the energy of the light will then be transmitted by the sample. On the contrary, if the equation (Eq. 2.3) is satisfied, the energy will be absorbed [2.25].

2.3.3.4 Normal Modes of Vibrations

When IR radiation interacts with matter the phenomena may be understood by gaining insight on the changes in molecular dipoles associated with vibrations and rotations. According to a basic model, a molecule can be regarded as a system of masses joined by bonds with spring-like properties. In the most simple case of diatomic molecules, like molecules which possess three degrees of translational freedom and two degrees of rotational freedom. The atoms are able to move relative to one another, where bond lengths may vary or one atom is able to

move out of its present plane. This is jointly referred to as vibrations. For a diatomic molecule only one vibration that corresponds to stretching and compression of the bond is allowed. This accounts for one degree of vibrational freedom.

Molecules containing many (N) atoms will have 3N degrees of freedom. In the case where molecules contain three atoms, two groups of triatomic molecules are well-known namely: linear and non-linear. CO₂ (carbon dioxide) and H₂O (water) are clear-cut examples of linear and non-linear triatomics, respectively. This is illustrated by Figure 2.3. CO₂ and H₂O both exhibit three degrees of freedom. Water has three degrees of rotational freedom, while carbon dioxide, a linear molecule has only two. Given that there is no energy detected involved in the rotation around the O = C = O axis. By subtracting these from 3N, consequently, any linear molecule like CO₂ results in 3N - 5 degrees of freedom and 3N - 6 for any non-linear molecule such as water. Moreover, water obtains three vibrational modes and carbon dioxide four vibrational modes. A summarized version of this is given in Table 2.2, which displays the degrees of freedom for triatomic molecules.

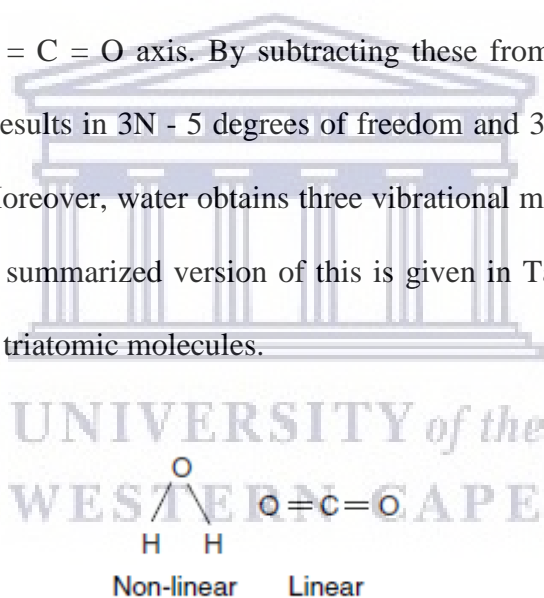


Figure 2.22: Water and carbon dioxide molecules [2.24].

Table 2.3: Degrees of freedom for polyatomic molecules [2.24].

Type of degrees of freedom	Linear	Non-linear
Translational	3	3
Rotational	2	3
Vibrational	3N - 5	3N - 6
Total	3N	3N

Diatomic molecules only have one mode of vibration which is consistent with a stretching movement. Furthermore, triatomic non-linear structured molecules in the form of B - A - B has three modes of vibration, two correlating to the stretching motions, and the other corresponding to a bending motion. Linear structured triatomic molecules have four modes, where two obtain the same frequency and are degenerate.

Another concept which plays an important role in the frequency of vibrational modes is the stiffness of the bond. The stiffness in the bond can be characterized by the force constant k stemmed from Hooke's law. The reduced mass denoted μ , assists by adding the individual atomic masses and may be given as follows:

$$\left(\frac{1}{\mu}\right) = \left(\frac{1}{m_1}\right) + \left(\frac{1}{m_2}\right) \quad (\text{Eq. 2.25})$$

Where m_1 and m_2 are the masses situated at the ends of the bond. Alternatively, this equation may also be expressed as:

$$\mu = \frac{m_1 m_2}{(m_1 + m_2)} \quad (\text{Eq. 2.26})$$

The frequency of absorption relates the force constant to the reduced mass by the following expression:

$$\nu = \left(\frac{1}{2\pi c}\right) \sqrt{\left(\frac{k}{\mu}\right)} \quad (\text{Eq. 2.27})$$

In order to use the direct wavenumber values for the bond vibrational frequencies, Eq. 2.27 may be altered as:

$$\bar{\nu} = \left(\frac{1}{2\pi c}\right) \sqrt{\left(\frac{k}{\mu}\right)} \quad (\text{Eq. 2.28})$$

Where c is the speed of light [2.24,2.27].

Molecular vibrations display two types of movements, either a change in bond length known as stretching or a change in the bond angle commonly referred to as bending. Both stretching and bending vibrations consist of more complex categories of vibrational movements. Symmetric and asymmetric vibrations are types of stretching vibration, while wagging, rocking, twisting, and scissoring are characteristic types of bending vibrations. Stretching vibration generally occur at higher energies in comparison to bending vibrations. Since the absorption process is quantized, stretching and bending vibrations are therefore present at specific allowed energy levels. Moreover, it is important to note that absorption strength is dependent on the dipole moment. Since absorption of infrared radiation can only take place once there is a change in the dipole moment of a molecule. Therefore, the greater the dipole change, the more intense the absorption band will be [2.11].

2.3.3.4.1 Stretching Vibration

Certain bonds are able to stretch in-phase (symmetrical stretching) or out-of-phase (asymmetrical stretching) as displayed in Figure 2.23. In symmetrical stretching the bond attached to atoms within the molecule either increase or decrease in length concurrently, while in asymmetrical stretching the bond lengths increase and decrease consecutively. If a molecule contains at least two or three identical groups, then symmetric and asymmetric stretching is able to arise in groups such as CH_2 , CH_3 , CCl_2 , $\text{C}_4\text{H}_6\text{O}_3$, NO_2 , and NH_2 . When a molecule has various kinds of atoms connected to the bonds such as HCN , ClCN , or ONCl , then the two stretching modes are no longer symmetrical or asymmetrical forms of vibration for similar bonds. Hence, these bonds will exhibit a range of stretching motion proportions for each group where the amount of coupling will vary. Symmetrical molecules generally have fewer infrared active' vibrations, and therefore has a lower energy in comparison to that

of the asymmetric stretching. A few examples of the variation between the appearance of symmetric and asymmetric vibrations are the symmetric stretch of CH_3 which appears at 2872 cm^{-1} , whereas for its counterpart the asymmetric stretch is found at 2962 cm^{-1} . In the same way, the symmetric stretch of NH_2 appears at 3300 cm^{-1} , while the asymmetric stretch is found at 3400 cm^{-1} as shown in Figure 2.23 [2.11].

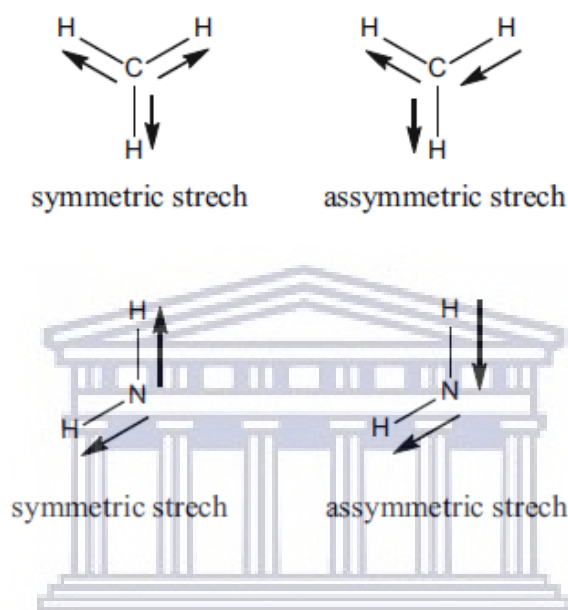


Figure 2.23: Symmetric and asymmetric stretching of the CH_3 and NH_2 molecules, where the asymmetric stretch is found at a higher energy than the symmetric stretching bond [2.11].

2.3.3.4.2 Bending Vibrations

A bending vibration is also referred to as deformation vibration that involves the change in a bond angle while the bond length remains constant. There are two kinds of bending vibrations which are in-plane and out-of-plane vibrations.

In-plane vibrations involve the movements of scissoring and rocking vibrations. In scissoring vibration, both atoms approach or move away from each other simultaneously, and hence, the bond angle decreases. Whereas the rocking vibration, however, shows no change in the bond

angle but participating bonds move within the plane in the same particular direction (see Figure 2.24).

Out-of-plane bending vibrations include the wagging and twisting vibrations. In wagging vibrations, both participating atoms move towards the same plane. While in twisting vibrations both atoms move toward opposing planes [2.11].

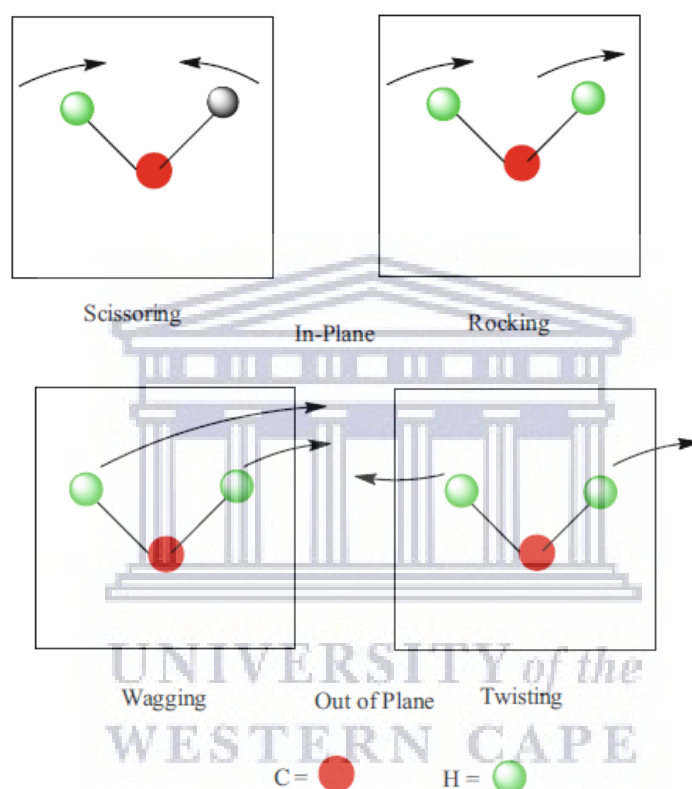


Figure 2.24: The various forms of bending vibrations in the CH₂ group [2.11].

The difficulty in interpreting an IR spectrum stems from the coupling of vibrations over a large fragment of the molecule or the whole of the molecule. These kinds of vibrations are referred to as skeletal vibrations, and their associated bands generally correspond to a fingerprint of the molecule entirely rather than of a specific group within the molecule [2.24].

An IR spectrum is generally split into the functional group region and the fingerprint region.

The fingerprint varies for each molecule. This means that two functional groups may produce

similar absorption spectra within the functional group region but will always differ within the fingerprint region. Characteristic vibrations are founded on the type of motions made by participating atoms. Generally, stretching vibrations that are found within the molecule are characteristic of typical functional groups. In organic compounds, characteristic vibrations for a specific functional group will usually take place within the region between 4000 - 1500 cm^{-1} . However, for inorganic compounds this range may differ for compounds with heavier atoms, and therefore these characteristic vibrations will be expected at lower frequencies. All frequencies which fall below 1500 cm^{-1} (the fingerprint region), often involve the bending motion of molecular vibrations. These characteristic vibrations represent the fingerprint of the molecule [2.7].

2.3.3.5 IR Analysis

FTIR spectra can be analysed in two ways which are through Qualitative and Quantitative techniques.

2.3.3.5.1 Qualitative Analysis

Interpreting an IR spectrum may be complex due to the various interactions between atoms within the molecule, and the fact that IR absorptions of functional groups may differ over a broad range [2.21]. However, FTIR spectroscopy is a technique which provides a means in identifications functional groups within a sample [2.25]. With this said, every compound's absorption spectrum is unique and obtains a molecular fingerprint that in most instances can be distinguished from the patterns of other molecules [2.29]. Therefore, researchers have taken the initiative to outline tables for identifying relative intensities and their absorption

bands. Table 2.6, a number provides functional groups and their characteristic absorption frequencies [2.21].

2.3.3.5.2 Quantitative Analysis

The foundation of quantitative analysis of IR absorption spectra revolves around the Bouguer-Beer-Lambert law expressed in Eq.2.23. This law basically states that the relation between absorbance and concentration is linear [2.21, 2.25]. Nonconformities from the Bouguer-Beer-Lambert law could be possible as a consequence of stray radiation, chemical effects and an inadequate resolution [2.29].

2.3.3.5.3 Organic Compound Interpretation

In order to elucidate an IR absorption spectrum, one needs to identify the absorption bands of an unknown compound and subsequently match them to their corresponding absorption frequencies to determine the types of bonds present in the sample. Table 2.4 displays certain characteristic vibrations belonging to certain functional groups correlating to their absorption frequencies within the spectrum [2.21].

Table 2.4: Characteristic absorption bands and their corresponding frequencies [2.21].

Bond	Compound type	Frequency range (cm ⁻¹)
C – H	Alkanes	2960 – 2950 (<i>s</i>) stretch
		1470 – 1450 (<i>v</i>) scissoring and bending
	CH ₃ Umbrella Deformation	1380 (<i>m - w</i>) – Doublet- isopropyl-butyl
C – H	Alkenes	3080 – 3020 (<i>m</i>) stretch
		1000 – 675 (<i>s</i>) bend
C – H	Aromatic Rings	3100 – 3000 (<i>m</i>) stretch
	Phenyl Rings Substitution Bands	870 – 675 (<i>s</i>) bend
	Phenyl Rings Substitution Overtones	2000 – 1600 (<i>w</i>) – fingerprint region
C – H	Alkynes	3333 – 3267 (<i>s</i>) stretch
		700 – 610 (<i>b</i>) bend
C = C	Alkenes	1680 – 1640 (<i>m, w</i>) stretch
C ≡ C	Alkynes	2260 – 2100 (<i>w</i>) stretch
C = C	Aromatic Rings	1600, 1500 (<i>w</i>) stretch
C – O	Alcohols, Ethers, Carboxylic acids, Esters	1260 – 1000 (<i>s</i>) stretch
C = O	Aldehydes, Ketones, Carboxylic acids, Esters	1760 – 1670 (<i>s</i>) stretch
O – H	Monomeric-Alcohols, Phenols	3640 – 3160 (<i>s, b</i>) stretch
	Hydrogen-bonded -Alcohols, Phenols	3600 – 3200 (<i>b</i>) stretch
	Carboxylic acids	3000 – 2500 (<i>b</i>) stretch
N – H	Amines	3500 – 3300 (<i>m</i>) stretch
		1650 – 1580 (<i>m</i>) bend
C – N	Amines	1340 – 1020 (<i>m</i>) stretch
C ≡ N	Nitriles	2260 – 2220 (<i>v</i>) stretch
NO ₂	Nitro Compounds	1660 – 1500 (<i>s</i>) asymmetrical stretch
		1390 – 1260 (<i>s</i>) symmetrical stretch

* *s* – strong, *v* – variable, *m* – medium, *w* – weak and *b* – broad

2.3.3.6 Working Principle

As previously stated, IR spectroscopy is based on the principle of the interaction between electromagnetic radiation and matter within the IR range [2.4]. Photons within the infrared spectrum possess the ability to cause a group of atoms to vibrate with respect to the bonds that join them. Once infrared radiation comes into contact with an IR active sample, the radiation is absorbed and consequently creates a variety of vibrational modes. Similar to electronic transitions, vibrational transitions correlates to discrete energies, and hence, molecules will only absorb radiations that correspond to particular wavelengths or

frequencies. As a molecule vibrates, a fluctuation in the molecule's dipole moment takes place. This then results in a field that interacts with the electric field coupled to the radiation [2.25]. During this interaction by absorbing the IR radiation, the molecules are excited to a higher vibrational state at a specific frequency. This absorption thus exposes the nature (chemical bonding and molecular structure) of these bonds present within the molecule. It is precisely for this reason that IR spectroscopy is considered a powerful technique. IR spectroscopy is able to provide fingerprint information on the chemical composition of the sample with absorption peaks correlating to the frequencies of the molecule present within the sample [2.4]. This technique proves to be useful for the analysis of organic and a few inorganic materials. By measuring the IR radiation as a function of frequency, one is able to obtain a spectrum. Through interpretation of the IR spectra, functional groups and compounds are easily distinguished by the absorption bands of the material. Qualitative and quantitative analysis of these bands allows for concentration of impurities or host materials to easily be deduced [2.21].

Once the interferogram is measured, the signal cannot be inferred directly, and hence, individual frequencies are then deciphered through the mathematical technique Fourier transformations. A resultant spectrum by a computer is then displayed, where further analysis can be performed [2.21].

2.3.3.7 Instrumentation of an FTIR Spectrometer

An FTIR instrument typically composes of an IR light source, an interferometer, sample compartment, detector, amplifier, and a computer [2.11]. An oversimplified illustration of the process is depicted in Figure 2.6. Unlike dispersive instruments, FTIR spectrometers are not

constructed as double-beam instruments since they attain single channelled spectra of a sample as well as a reference spectra prior to calculating their ratio [2.28]. In the process of analysing a sample, a light source produces radiation which passes through an interferometer and subsequently impinges on the sample until finally reaching the detector. Upon the radiant beam reaching the detector, the signal is then amplified, and converted from an analogue to a digital signal via an amplifier which consequently produces an interferogram. A spectrum is then generated by the utilization of the mathematical technique of Fourier Transforms [2.11,2.24]. A schematic of an FTIR spectrometer can be seen in Figure 2.25.

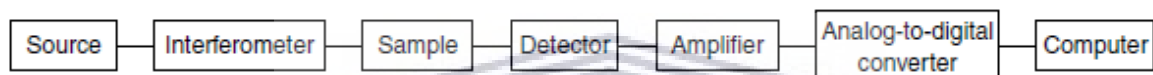


Figure 2.25: Main constituents of an FTIR spectrometer [2.24].

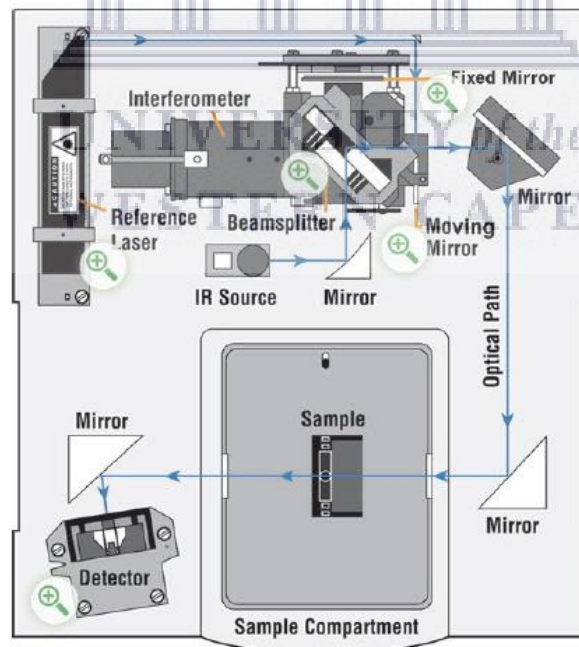


Figure 2.26: Illustration of the operation of a Thermo Nicolet FTIR Instrument. Produced by Thermo Fisher Scientific (Madison, WI, USA) [2.12].

2.3.3.7.1 Michelson Interferometer

The interferometer is often regarded as the key component in an FTIR instrument. The most widely used interferometer is the Michelson interferometer [2.24]. The Michelson interferometer is made up of three main components namely: two flat mirrors situated on perpendicular planes to each other (one being fixed in one arm of the interferometer and the other mobile within the other arm) and a beamsplitter which bisect the two mirrors (see Figure 2.27). The choice of beamsplitter material is dependent on the IR region being studied. Typical MIR and NIR beamsplitters are constructed with an IR-transparent materials like potassium bromide (KBr) or caesium iodide (CsI) as a substrate, with a germanium (Ge) or iron oxide (FeO) multilayer coating. Poly(ethyleneterephthalate) is an organic thin film used in the FIR region beamsplitters [2.24,2.28].

Standard beam – splitters have a reflectivity of 50% and no absorption across its range of use. The Michelson interferometer operates on a well aligned monochromatic IR beam of wavelength λ (cm^{-1}). Once the radiant beam reaches the beamsplitter, the beam is then subsequently divided into two parts of equal intensity. After dividing, the beams are then reflected accordingly between the fixed and movable mirror back to the beamsplitter, where they recombine and interfere [2.28]. Vo-Dinh et al., says that “The displacement of the movable mirror causes change in the optical pathlength between the two beams, so that the conditions for constructive ($n\lambda$) and destructive interference $(n + \frac{1}{2})\lambda$, as well all intermediate states between the two, are consecutively met.” [2.24, 2.30]. The recombined IR beam is then directed towards the sample or reference (source), interacts with the sample, and finally comes into contact with the detector. The beam which exits the interferometer perpendicular to the input beam is referred to as the transmitted beam which is the beam detected for Fourier transformations (FTIR spectrometry). It should be noted that the position and motion

of the movable mirror are controlled by a helium-neon laser ($\lambda_{HeNe} = 632.8 \text{ nm}$), where the IR interferogram sampling is controlled by the interferogram of the helium-neon laser in increments as small as $\lambda_{HeNe}/2 = 316.4 \text{ nm}$ [2.28].

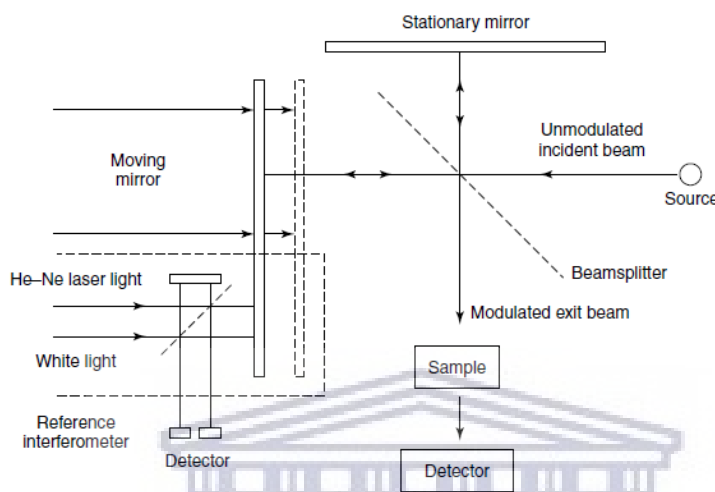


Figure 2.27: Schematic representation of a Michelson interferometer [2.24].

2.3.3.7.2 IR Sources

IR radiation is given off by a glowing black body source. An aperture is used to limit the amount of radiation that interacts with the sample, and eventually the detector. In the MIR region FTIR spectrometers often use a Globular or Nernst source. Globular sources composed of silicon carbon rods which are resistively heated. When an electric current is passed through the rod, the rod reaches temperatures of 1300 K, and therefore emits large amounts of radiation. The progression in metal alloys have allowed for these IR sources to operate without the use of cooling water where in the past it was required to avoid damaging electrical components. Nernst Glowers are constructed from a combination of refractory oxides and has the ability of reaching temperatures exceeding that of the Globular, however, they are incapable of yielding radiation greater than 2000 cm^{-1} [2.12]. For samples being

studied within the NIR region, a tungsten-halogen lamp is used as an IR source, whilst in the FIR region a high pressure mercury lamp is utilized [2.24].

2.3.3.7.3 Detectors

The most prominent kinds of detectors used for the MIR region are the DTGS and the MCT. The abbreviation DTGS is a pyroelectric device which incorporates deuterium tryglycine sulphate in a temperature-resistant alkali halide window. These kinds of detectors are employed for general routine type of uses. For projects in demanding more sensitive analysis, a mercury cadmium telluride (MCT) detector is applied. However, these kinds of detectors require cooling to the same temperatures as liquid nitrogen.

In other regions such as FIR, germanium (Ge) and indium (In)-antimony (Sb) detectors are employed and function at liquid helium temperatures. In NIR regions, lead sulphide photoconductors detectors are commonly used [2.24].

2.3.3.7.4 Fourier – Transformation

Stuart, 2004 stated that “The necessary equations required for Fourier Transformations relating to the intensity falling on the detector $I(\delta)$, to the spectral power density at a particular wavenumber, $\bar{\nu}$, given by $B(\bar{\nu})$, are given as follows:

$$I(\delta) = \int_0^{+\infty} B(\nu) \cos(2\pi\nu\delta) d\nu \quad (\text{Eq.2.30})$$

Which is one half of the cosine Fourier – transform pair, with the other being:

$$I(\bar{\nu}) = \int_{-\infty}^{+\infty} I(\delta) \cos(2\pi\bar{\nu}\delta) d\delta \quad (\text{Eq.2.31})$$

These two equations are interconvertible and are known as a Fourier-transform pair. The first equation displays the relation between the variations in power density as a function of the

difference in pathlength, and as a result an interference pattern is produced. The latter displays the change in intensity as a function of wavenumber, which can be altered by fourier transformation” [2.24].

The objective when using an FTIR spectrometer is to produce an interfereferogram which ultimately is used to yield an FTIR spectrum. During the course of sample analysis, two interferograms are generated with one being (a) the source with sample absorptions and (b) the source without sample absorptions. The latter and former are then used to make a ratio which corresponds to a double beam dispersive spectrum.

The new algorithm used for fast Fourier transformation (FFT) displays vast improvements to the standard FTIR technique within the MIR region. This, in collaboration with computers, makes way for calibrations to be processed and executed at a much faster rate [2.24].

2.3.3.7.5 Computers

The computer performs a number of functions when operating the FTIR spectrometer. It is responsible for the managing of the instrument, scan speeds, scan limit as well as the starting and stopping of the scanner. Once the computer reads the spectra from the instrument, it is then stored within the computer’s memory as the spectrum is scanned [2.24].

2.3.3.8 Data Acquisition

Chemical information regarding the functional groups and bonds formed within Sn_xO_y thin films were given by the Perkin Elmer Spectrum Two FT-IR instrument located in the Chemistry Department (UWC). In performing IR analysis on all Sn_xO_y , a LiTaO_3 detector was utilized, where a resolution of 4 cm^{-1} was used on every sample to produce a spectrum within a range of $\lambda = 4000 - 400 \text{ cm}^{-1}$.

2.3.4 Rutherford Backscattering Spectrometry

2.3.4.1 Introduction

Rutherford Backscattering Spectrometry (RBS) is a technique that relies on the principle of ion scattering in order to find the composition of sample. The technique encompasses the measurement of the number and energy distribution of these energetic ions such as protons or He^+ elastically backscattered within the near-surface region of solid targets. RBS is primarily used to analyse nm - μm thin films and is unique in that it permits quantification without any knowledge of reference standards and can be used to calibrate other analytical methods [2.28]. It is the preferred method with regards to quantitative compositional analysis of thin films used for semiconductors, optical coatings, and other applications where the parameters pertaining to film composition is essential [2.5].

2.3.4.2 Theory

During RBS analysis, a beam of mono-energetic ions such as H^+ and He^+ of energy generally between 0.5 - 2.5 MeV, is aimed towards a target. After the beam of ions interacts with the target, the energies of the ions which are scattered backward are scrutinised. In a backscattering collision, upon impact, energy is transferred from the impinging particle to the static target atom. Binary collision theory provides the energy ratio between the projectile energy E_1 after a collision and the initial energy E_0 before a collision by the following equation:

$$\frac{E_1}{E_0} = K = \left[\frac{(M_2^2 - M_1^2 \sin^2 \theta)^{1/2} + M_1 \cos \theta}{M_1 + M_2} \right]^2 \quad (\text{Eq. 2.32})$$

The energy ratio E_1/E_0 is known as the kinematic factor K , relates the dependence of the energy of the scattering to that of the mass M_1 of the projectile, mass M_2 of the target atom, and the scattering angle θ between the incident and scattered beams. Furthermore, the element of the target can be identified if the values of M_1 , E_0 and θ are known. If direct backscattering through an angle of 180° takes place, the lowest energy ratio value is then given by Eq. 2.33:

$$\frac{E_1}{E_0} = \left(\frac{M_2 - M_1}{M_2 + M_1} \right)^2 \quad (\text{Eq. 2.33})$$

For a scenario where $M_1 = M_2$, the incident particle transfers all the energy to the target atom. Hence, after this central collision, the incident particle remains at rest. If $M_2 < M_1$, then no backscattering takes place.

Eq.2.33 presents the energy of an ion being backscattered after a collision with a target atom with reference to the target surface. In RBS however, the ion beam is also able to penetrate beyond the target surface, where an ion may be backscattered by target atoms at any point along its path. The amount of energy used in this technique gives way for ions to voyage in straight lined trajectory. This however, excludes the motion after a backscattering event. During this straight-line trajectory, an ion loses energy mainly through excitation and ionization of atomic electrons popularly known as the process of electronic energy loss. Palmetshofer et al. says that “The energy loss per path length is symbolized dE/dx , also known as the stopping power.” Supplementary energy losses such as these ultimately broaden the peaks observed in an RBS spectrum of a thin film [2.20].

2.3.4.3 Instrumentation

A standard RBS instrument consists of a particle accelerator that is able to supply beams of low – mass ions within the MeV range. In a brief description, ions are initially generated in an ion source such as a duoplasmatron, accelerated, then selected by their mass and charge, and finally directed towards the specimen. Duoplasmatrons are able to produce ions of both polarities. Traditionally, the Van de Graaff electrostatic accelerator has been the most extensively used particle accelerator that being of either single or double ended (tandem) [2.20]. Generally, the tandem accelerator produces negative ions which are accelerated towards a positive potential. The particles then travel within a vacuum system. Upon reaching the high voltage terminal, electrons are then stripped off the ion where the charge then becomes positive. Particles are then subsequently repelled by the high positive voltage which then increases their energy [2.6]. Thereafter, the beam is analysed and navigated via electrostatic or magnetic lenses towards the target chamber. The beam diameter at the target is approximately 1 mm in size [2.6,2.20]. If smaller beam spots preferred, this can be made possible by applying more suitable lens systems. Particle beams typically collide with the target upon normal incidence. However, the option of mounting a sample on a multiple axis manipulator is also accessible. The multiple axis manipulator allows samples to be rotated about a point of ion impact to vary the angle of incidence is available. This is done by means of channelling directions [2.20].

In agreement with Eq. 2.32, the idyllic scattering angle would be $\theta = 180^\circ$ because it would serve in producing the optimum mass resolution for a given ΔM_2 because the largest change in K value will then be produced. On the other hand, due to the size of the detector, for practical purposes an angle of $\theta = 170^\circ$ is chosen [2.20]. When incident particles penetrate the target, a few of them will encounter a Coulomb force from the target nuclei and will be

redirected from its path. This interaction is dependent on the Rutherford cross section. And even though a minute number of the deflected ions will be backscattered, an adequate amount will reach the detector [2.6]. Backscattered ions are usually detected using a solid state detector such as a silicon barrier detector or a passivated implanted planar silicon (PIPS) detector. Detector signals are highly proportional to the energy of the incident particle, are intensified and arranged in terms of energy in a multichannel analyser [2.20]. Figure 2.28 displays the general layout of an RBS instrument during sample analysis.

Additionally, it is important to know that whilst performing RBS analysis of a target matrix, that the incident low-mass particles are able to lose their energy in processes other than elastic Rutherford events. It is for this reason that for larger sample depths, the energy of E_0 is vague. However, this value can be acquired before a collision takes place. In actuality, if the material of a given target sample known, the change in energy loss can be translated into a depth of scale. It is in this manner that RBS is capable of producing depth profile analysis up to a few micrometres within a film [2.6].

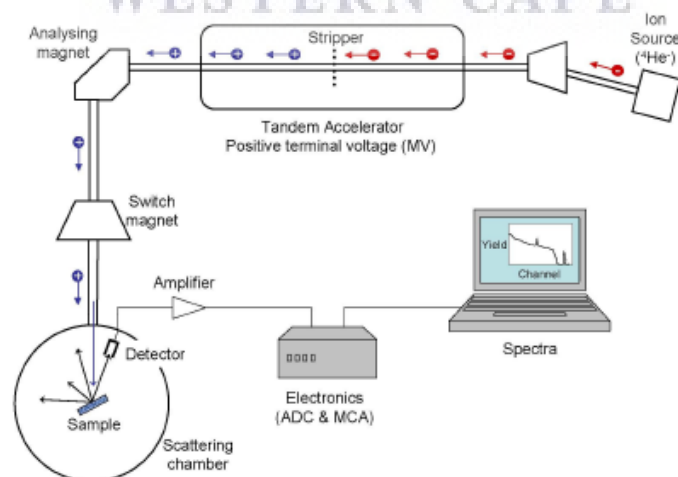


Figure 2.28: Conventional layout of an RBS instrument whilst performing an experiment [2.6].

2.3.4.4 Spectral Information

From a conventional RBS spectrum, one of the most prominent features that may be quantified is the depth of elements in a surface layer of the film. The depth of the elements within the film includes the deduction of properties such as the mass of the scattering atoms, the composition of the surface layer, the depth of the scattering atoms, and the thickness of the surface layer.

By obtaining knowledge concerning the composition of a layer, RBS allows the user to achieve information about the distribution of an element within a depth scale and to deduce the layer thickness by means of the energy of the scattered particles. Palmetshofer et al. declares that “This depends on the energy loss of the projectile on its inward and outward paths, as described by in (the theory) section.” The difference in energy (ΔE), between a particle scattered and a particle scattered at a depth given by x is expressed in Eq. 2.34:

$$\Delta E = [S]x \quad (\text{Eq. 2.34})$$

Where the energy loss factor $[S]$ is influenced by the stopping power experienced by the trajectory of the particles path, the kinematic factor K , and the orientation of the sample with reference to the incoming beam and the direction of the detector.

The RBS in conjunction with channelling is used to detect and measure the thickness of an amorphous layer on a crystalline substrate. This technique bestows structural information pertaining around the damage of a surface layer of ion-implanted semiconductors, as well as being able to study the locations of impurity atoms. Furthermore, this method conveys knowledge concerning the eradication of this surface damage caused by annealing [2.20].

2.3.4.5 Quantification

Consider an incident beam striking a target thin film where the total number of particles within that is represented by the value Q . After colliding with an atom of type A , the number Q_A , provides the sum of the backscattered particles registered in the detector. This is also referred to as the yield denoted Y_A , and is related to Q_A in the following manner:

$$Q_A = Y_A = Q N_A \sigma_A \Delta\Omega \quad (\text{Eq. 2.35})$$

Where N_A is the real density of atoms A in the film measured in units of atoms. cm^{-2} . The differential cross – section is given by σ_A ($\text{cm}^2 \cdot \text{sr}^{-1}$) and $\Delta\Omega$ is the solid angle of the detector. Since the interaction potential between a particle (M_1, Z_1) and a target atom (M_2, Z_2) can be described through the Coulomb potential, therefore, the Rutherford formula for the cross – section is given as:

$$\sigma(E, \theta) = \left(\frac{Z_1 Z_2 e^2}{4E} \right)^2 \frac{4 \left[(M_2^2 - M_1^2 \sin^2 \theta)^{1/2} + M_2 \cos \theta \right]^2}{M_2 \sin^4 \theta (M_2^2 - M_1^2 \sin^2 \theta)^{1/2}} \quad (\text{Eq. 2.36})$$

In ion – beam analysis c g s units are used. This is applicable to the result of Eq. 2.36, while the value of $e^2 \approx 1.44 \times 10^{-13}$ MeV is implemented for more practical calculations. The Rutherford cross-section (Eq. 2.36) is applied for ions 1 - 2 MeV He^+ . Any deviation from this formula occurs for energies out of this range. There are certain experimental circumstances, where the scattering cross – section is only a function of the mass and atomic number of the scattering atom. So for experimental conditions deemed as such, the scattering cross-section may be easily determined [2.20].

Composition of a compound film with elements A_mB_n may be computed by means of Eq. 2.35 and Eq. 2.36, such that:

$$\frac{n}{m} = \frac{N_B}{N_A} = \frac{Q_B}{Q_A} \frac{\sigma_A(E,\theta)}{\sigma_B(E,\theta)} \quad (\text{Eq. 2.37})$$

This ratio is only reliant measured constraints and is easily determined because the complicated quantities like Q and $\Delta\Omega$ cancels out.

For a multi-compositional thin film constituting of several elements that may course overlapping peaks within the RBS spectrum. Deconvolutions of these peaks are done executed computer simulations. A common analysis program that performs such simulations is the RUMP code, although a more recent analysis program going by the name of the IBA data furnace is also becoming more prominent amongst RBS operators [2.20].

2.3.4.6 Data Acquisition

RBS analysis of oxidized metallic Sn thin films deposited on Si substrates was executed at iThemba Laboratory for Accelerator-Based Sciences (iThemba LABS (NRF) research institute) situated in Faure, Cape Town. Examination of the Sn_xO_y thin films samples were performed by using a 3 MeV single beam of He alpha particles generated from 1 MV tandem accelerator. All thin film samples (as-deposited and annealed Sn films) situated at a (-5°) tilt angle within the vacuum chamber with a pressure of approximately $10^{-3} - 10^{-4}$ Pa, were then investigated by the 2 mm collimated ion beam kept at a constant current at around 70 nA. After sample and beam interaction, the consequent backscattered ions originating from the sample were then detected by a silicon surface barrier (SSB) detector placed at a 150° (30° from the focused ion beam) scattering angle from the sample. The signal from the detector was then pre-amplified and lead to the spectroscopic amplifier until it was eventually translated into an RBS spectrum.

2.3.5 UV-Visible Spectroscopy

2.3.5.1 Introduction

At this point it is quite evident that the interaction between radiation and matter brings rise to a number of processes such as reflection, scattering, absorbance, fluorescence/phosphorescence (absorption and re-emission), and photochemical reactions (absorbance and bond breaking). With regard to the UV-Visible (UV-Vis) instrument, majority of the analysis is mainly focused around the absorbance process of radiation within the ultra-violet region ($\lambda = 10 - 400 \text{ nm}$) and visible region ($\lambda = 400 - 800 \text{ nm}$) of the electromagnetic spectrum. Since light is a form of energy, therefore, when atoms (or molecules) are subjected to light through absorbance, the energy content of these atoms increase. The absolute potential energy of a molecule is represented as a sum of its electronic, vibrational, and rotational energies [2.19]:

$$E_{total} = E_{electronic} + E_{vibrational} + E_{rotational} \quad (\text{Eq. 2.38})$$

Owen, T. declares that “The amount of energy a molecule possesses in each form is not a continuum but a series of discrete levels or states” The difference in energy between such states in order of magnitude is given by the following order:

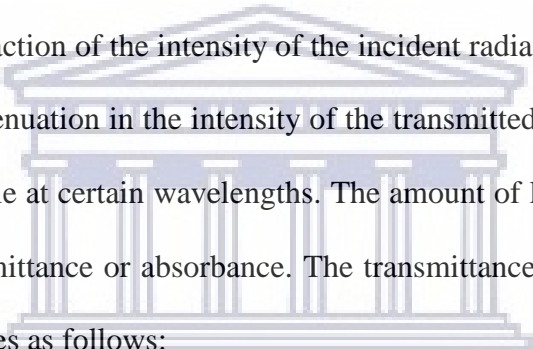
$$E_{electronic} > E_{vibrational} > E_{rotational} \quad (\text{Eq. 2.39})$$

In certain molecules and atoms, absorbed photons with wavelengths of magnitude that falls within the UV or visible range acquires sufficient amounts of energy to trigger transitions between the various electronic energy levels. By absorbing the wavelength which owns the necessary amount of energy for this transition, it ultimately allows an electron to be promoted from a lower energy level to a higher energy level. It is for this reason that UV/Vis

spectroscopy may be referred to as electronic spectroscopy. Organic chemists often utilise this spectroscopic technique for the elucidation of conjugated multiple bonds or aromatic rings [2.19]. However, in this case, the analysis will be concerned with the absorbance of radiation within thin films.

2.3.5.2 Transmittance and Absorbance

When light impinges on a sample, it may reflect, transmit, or absorb. A UV/Vis spectrophotometer measures the intensity of light (I) after passing through a sample. This transmitted intensity is a fraction of the intensity of the incident radiation (I_0) produced by the light source [2.19]. The attenuation in the intensity of the transmitted light occurs as result of the absorption by the sample at certain wavelengths. The amount of light absorbed can either be given in terms of transmittance or absorbance. The transmittance T , is described by ratio between these two intensities as follows:


$$T = \frac{I}{I_0} \quad (\text{Eq. 2.40})$$

Transmittance can either be expressed as a fraction of 1, or as a percentage (%) by multiplying the result by 100. The absorbance A , as seen in section 2.3.3.2, is related to the T in the following manner:

$$A = -\log T \quad (\text{Eq. 2.41})$$

The absorbance can either be expressed in terms of the optical density or by the molar absorptivity as outlined by the Bouguer-Beer-Lambert law [2.3]. According to the Bouguer-Beer-Lambert Law, the fraction of incident monochromatic radiation absorbed by a homogeneous medium is proportional to the number of absorbing molecules and the

pathlength of the radiation travelling through the medium, as given by Eq. 2.23. For a solid sample, the Beer-Lambert described by the following equation:

$$\log \frac{I}{I_0} = A = \alpha x \quad (\text{Eq. 2.42})$$

Where the proportional factor α is known as the linear absorption coefficient of the medium is reliant on the wavelength of the radiation, and x is the distance the radiation travels through the solid [32, 33].

2.3.5.3 UV-Vis mechanism

Electronic transitions within a molecule are responsible for the production of UV – Vis spectra. These transitions are called electronic excitations and involve the promotion of valence electrons from the ground state to a higher energy state. The absorbed electromagnetic radiation is of the same magnitude difference in energy these states [2.32].

The transition with the highest probability of happening is generally from the highest occupied molecular orbital (HOMO) to the lowest unoccupied molecular orbital (LUMO).

The lowest occupied energy orbitals for most molecules are σ bonding orbitals, π bonding orbitals, and n orbitals where unshared pairs of electrons (lone pair) are held. The unoccupied, or antibonding orbitals with the highest energy are the π^* and the σ^* orbitals. It should be noted that there are no n^* orbitals in existence since electrons do not form bonds [2.8]. The arrangement of energy required for electronic transitions between orbitals are listed below and illustrated in Figure 2.30:

$$\sigma \rightarrow \sigma^* > n \rightarrow \sigma^* > \pi \rightarrow \pi^* > n \rightarrow \pi^* \quad (\text{Eq.2.43})$$

Here, $\sigma \rightarrow \sigma^*$ transitions are prompted by advancement of an electron from a σ orbital to its corresponding antibonding orbital σ^* . Since σ bonds are very strong, this process generally requires high levels of energy associated with wavelengths in the range $\lambda = 200 - 800$ nm. It is for this reason that these transitions are usually not observed within the normal UV – Vis range. For an electron promoted from a non-bonding orbital n , to an anti-bonding σ^* orbital $n \rightarrow \sigma^*$ transition is assigned. Compounds encompassing non-bonding electrons on a heteroatom is able to absorb an adequate amount of energy for this kind of transition. $n \rightarrow \sigma^*$ transitions require lower energy than $\sigma \rightarrow \sigma^*$ transitions. Organic compounds such as halides, alcohols, ethers, undergo $n \rightarrow \pi^*$ transitions. $n \rightarrow \pi^*$ transitions are caused by the elevation of an electron from a π bonding orbital to a π^* orbital. $\pi \rightarrow \pi^*$ requires lower energy than $n \rightarrow \sigma^*$ transitions. $n \rightarrow \pi^*$ transitions involves that least amount of energy. This kind of transition takes place when electron from a non – bonding orbital to an anti-bonding orbital π^* [2.32].

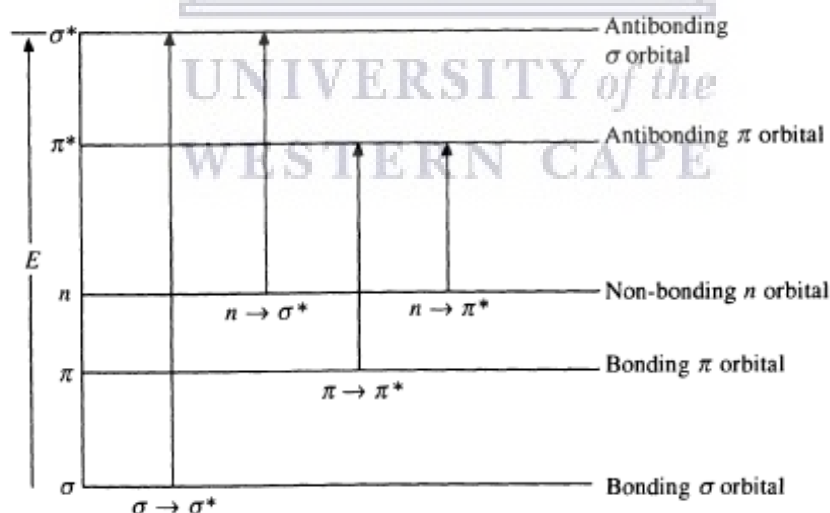


Figure 2.29: Electronic transitions and their relative energy [2.32].

2.3.5.4 Instrumentation

Since UV-Vis analysis mainly revolves around the principle of absorbance, it is for this reason that a UV-Vis spectrophotometer compares the intensity of the transmitted radiation through a medium to that of the incident UV-Vis radiation. The most popular kind of UV-Vis spectrophotometers are double beam instruments made up of the following constituents (see Figure 2.30):

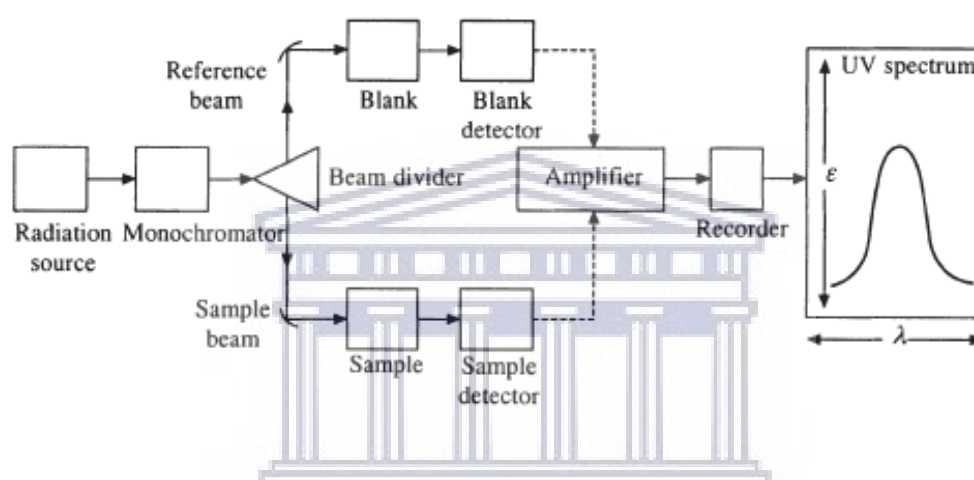


Figure 2.30: Simplified illustration of a UV-Visible spectrometer [2.32].

1. Radiation source – Typically a hydrogen-discharge lamp source is used for the analysis UV operating within the UV range ($\lambda = 180 - 400 \text{ nm}$). If a source with more intensity is needed, a deuterium discharge lamp offers 3 - 5 times more intensity. In the visible region ($\lambda = 400 - 800 \text{ nm}$) a tungsten-filament lamp is employed in order study the absorption within this interval.
2. Monochromator – The objective of a monochromator is to disperse the radiations originating from source into their separate wavelengths. In the UV range a quartz prism is transparent, and is the most commonly used dispersing element. Glass is typically set in place for the visible region because it absorbs in the UV region and is therefore only applicable within the visible range. Once the radiation is dispersed, it is

divided into two parallel beams of equal intensity. The beam which passed through the transparent cell containing the sample solution is known as the sample beam. The other beam is passed through an identical cell containing the solvent and is called the reference beam.

3. Detectors – Detectors are composed of photocells or photomultiplier tubes which generate a voltage relative to the radiation inflicted upon them.
4. Amplifier – The purpose of the amplifier is to subtract the absorption of a solvent from that of the solution. This is done electronically by an electronic balancing amplifier.
5. Recorder – The recorder's main function is to automatically attain the necessary information required to produce a spectrum of the wavelengths of absorbed radiation against the absorbance A and the molar absorptivity ϵ [2.32].

2.3.5.5 Data Acquisition

All data pertaining to the UV-Vis spectroscopy was attained through the experimental set-up at the Department of Physics and Astronomy (UWC). Samples were irradiated by continuous beam of light of wavelength ($\lambda = 190 - 1200$ nm) generated by a deuterium (D) and tungsten (W) light source. Absorption of these films were analysed by comparing the intensity of the incident beam to that of the transmitted beam. The detector subsequently senses this ratio of intensities and converts this information into a digital signal, where a resultant spectrum is then produced [2.13].

References

- 2.1 Akhtar, K., Khan, S. A., Khan, S. B. and Asiri, A. M. (2018). Scanning Electron Microscopy: Principle and Applications in Nanomaterials Characterization. In: Sharma, S.K.1st Ed. Handbook of Materials Characterization. s.l: Springer International Publishing, 113 - 144.
- 2.2 Cullity, B. D. (1978). Properties of X-rays. In: M. Cohen, 2nd Ed. Elements of X-ray Diffraction. California: Addison-Wesley Publishing Company Inc., 3 - 29.
- 2.3 De Caro, C. and Haller, C. (2015). UV/Vis Spectroscopy. In: De Caro, C. and Haller, C. 1st Ed. UV/VIS Spectrophotometry - Fundamentals and Applications. Columbus: Mettler-Toledo, 6 - 7.
- 2.4 Dr. Gurumurthy.B. R and Dinesh Bhatia, D. (2017). Structural Analysis Of Merino Wool, Pashmina And Angora Fibers Using Analytical Instruments Like Scanning Electron Microscope And Infra-Red Spectroscopy. International Journal of Engineering Technology Science and Research, 4(8), 112 - 125.
- 2.5 EAG Laboratories. (2017). RBS Services | Rutherford Backscattering | EAG Laboratories. [Online] Available at: [https://www.eag.com/resources/appnotes/rutherford-backscattering-spectrometry-rbs-services/#:~:text=Rutherford%20Backscattering%20Spectrometry%20\(RBS\)%20is,to%20calibrate%20other%20analytical%20methods.](https://www.eag.com/resources/appnotes/rutherford-backscattering-spectrometry-rbs-services/#:~:text=Rutherford%20Backscattering%20Spectrometry%20(RBS)%20is,to%20calibrate%20other%20analytical%20methods.) [Accessed 25 May 2020].

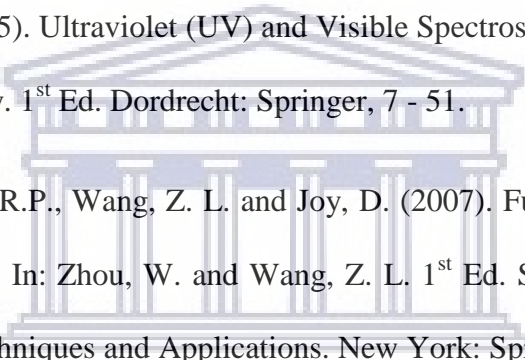
- 2.6 Hallén, A. (2012). Brief introduction to Rutherford Backscattering Spectrometry. [Online] Available at: <http://www.rzg.mpg.de/~mam/Version5.html> [Accessed 25 May 2020].
- 2.7 Hardinger. (2014). UCLA College. [Online] Available at: http://www.chem.ucla.edu/~harding/notes/notes_14C_IR.pdf [Accessed 3 April 2020].
- 2.8 Ikpo, D. (2018). Structural Tools in Nanochemistry, lecture notes, NSS 823, University of the Western Cape, delivered 13/3/2018.
- 2.9 IntechOpen. (2020). IntechOpen. [Online] Available at: [ntechopen.com/books/high-performance-concrete-technology-and-applications/microstructure-of-concrete](https://www.intechopen.com/books/high-performance-concrete-technology-and-applications/microstructure-of-concrete) [Accessed 29 4 2020].
- 2.10 Jaggi, N. and Vij, D. R. (2006). Fourier Transform Infrared Spectroscopy. In: Vij D. 1st Ed. Handbook of Applied Solid State Spectroscopy. Boston: Springer, 411- 450.
- 2.11 Khan S.A., Khan S.B., Khan L.U., Farooq A., Akhtar K., Asiri A.M. (2018) Fourier Transform Infrared Spectroscopy: Fundamentals and Application in Functional Groups and Nanomaterials Characterization. In: Sharma S. 1st Ed. Handbook of Materials Characterization. Cham: Springer, 317 - 344.
- 2.12 LCGC's Chromacademy. (2019). Introduction To Infrared Spectroscopy. [Online] Available at: <https://instapdf.in/infrared-ir-spectroscopy-complete-details/> [Accessed 5 March 2020].
- 2.13 Magubane, S. (2018). Metal Assisted Chemically Etched Silicon Nanowires For Application In A Hybrid Solar Cell. M.Sc. University of the Western Cape (UWC).

- 2.14 Martín-Palma, R. J. and Lakhtakia, A. (2013). Vapor-Deposition Techniques. In: P. S. U. Department of Materials Science and Engineering. 1st Ed. Engineered Biomimicry. Pennsylvania: Elsevier Inc., 383 - 398.
- 2.15 Moraes, L. G. P., Rocha, R. S. F., Menegazzo, L. M., Araújo, E. B. de, Yukimito, K. and Moraes, J. C. S. (2008). Infrared spectroscopy: a tool for determination of the degree of conversion in dental composites. *Journal of Applied Oral Science*, 16(2), 145 - 149.
- 2.16 MTI KJ Group. (2013). MTI Corporation. [Online] Available at: <https://www.mtixtl.com/furnacecontroller.aspx> [Accessed 28 May 2020].
- 2.17 MTI KJ GROUP. (2013). MTI Corporation. [Online] Available at: <https://www.mtixtl.com/1100CCompactSplitTubeFurnace-OTF-1200X-SNT.aspx> [Accessed 28 May 2020].
- 2.18 Oliphant, C. (2008). Filament Carburization During The Hot-Wire Chemical Vapour Deposition Of Carbon Nanotubes. MSc. University of the Western Cape (UWC).
- 2.19 Owen, T. (2000). Principles and applications of UV-visible spectroscopy. In: Owen, T. 2nd Ed. *Fundamentals of Modern UV-visible spectroscopy*. Germany: Agilent Technologies, 1 - 28.
- 2.20 Palmeshofer, L. (2011). Rutherford Backscattering Spectroscopy (RBS). In: Friedbacher, G. and Bubert, H. 2nd Ed. *Surface and Thin Film Analysis: A Compendium of Principles, Instrumentation, and Application*. Weinheim: Wiley-VCH Verlag GmbH & Co. KGaA., 191 - 202.

- 2.21 Panchal, N., 2011. Study And Characterisation Of Some Hexa - Ferrite Systems. Ph.D. Gujarat University Ahmedabad.
- 2.22 Shahidi, S., Moazzenchi, B. and Ghoranneviss, M. (2015). A review-application of physical vapor deposition (PVD) and related methods in the textile industry. The European Physical Journal Applied Physics, 71(3), 31302 (1 - 13).
- 2.23 Slinger, J. (2017). Post - Deposition Doping Of Silicon Nanowires. MSc. University of the Western Cape (UWC).
- 2.24 Stuart, B. H. (2004). Introduction. In: Ando D. J. 1st Ed. Infrared Spectroscopy: Fundamentals and Applications. Chichester: John Wiley & Sons, Ltd, 1 - 13.
- 2.25 The LibreTexts libraries. (2019). Infrared: Theory. [Online] Available at: <https://chem.libretexts.org/link?1847> [Accessed 5 March 2020].
- 2.26 The LibreTexts libraries. (2019). The LibreTexts libraries. [Online] Available at: <https://chem.libretexts.org/link?1846> [Accessed 2 April 2020].
- 2.27 Theophanides, T. (2012). Introduction to Infrared Spectroscopy. In: Theophanides, T. n.k. Infrared Spectroscopy - Materials Science, Engineering and Technology. Athens: ResearchGate, 1 - 9.
- 2.28 Thiele, S. and Salzer, R. (2002). Optical Spectroscopy. In: Gauglitz, G. and Vo-Dinh, T. 1st Ed. Handbook of Spectroscopy. Weinheim: WILEY-VCH Verlag GmbH & Co. KGaA, 39 - 37.
- 2.29 Tullin, C. and Amand, L. (1999). The Theory Behind FTIR Analysis Application Examples From Measurement At The 12 MW Circulating Fluidized Bed Boiler At

Chalmers, lecture notes, Measurement Technology, The Centre of Combustion Science and Technology, n.d.

- 2.30 University of Florida, n.d. Thermal Evaporation. [Online] Available at: <http://ww2.che.ufl.edu/unit-ops-lab/experiments/semiconductors/evaporation/Evaporation-theory.pdf> [Accessed 25 5 2020].
- 2.31 Waseda, Y., Matsubara, E. and Shinoda, K. (2011). Fundamental Properties of X-rays. In: n.k. 1st Ed. X-Ray Diffraction Crystallography. Berlin: Springer, 1 - 6.
- 2.32 Yadav, L. D. S., (2005). Ultraviolet (UV) and Visible Spectroscopy. In: Yadav, L. D. S. Organic Spectroscopy. 1st Ed. Dordrecht: Springer, 7 - 51.
- 2.33 Zhou, W., Apkarian, R.P., Wang, Z. L. and Joy, D. (2007). Fundamentals of Scanning Electron Microscopy. In: Zhou, W. and Wang, Z. L. 1st Ed. Scanning Microscopy for Nanotechnology. Techniques and Applications. New York: Springer-Verlag New York, 1 - 39.



UNIVERSITY of the
WESTERN CAPE

CHAPTER 3

RESULTS AND DISCUSSION

3.1 Introduction

Nano-sized SnO₂ thin films may be applied in a number of devices such as a window layer in solar cells, heat reflectors in solar cells, various gas sensors, transparent conductive electrodes, photochemical and photoconductive devices in liquid crystal devices, gas discharge displays, and in lithium-ion batteries [3.40, 3.1]. Being favourable amongst many metal oxides due its aforementioned superior optical, structural, and electrical properties; is the reason why novel, relatively easy and feasible methods for manufacturing SnO₂ thin films are in such high demand [3.40, 3.1]. Such characteristic properties are highly related to the composition (concentration of Sn atoms), extent of contaminations, microstructure (adsorption of oxygen on the surface or grain boundaries), and most importantly, point defects (oxygen vacancies and interstitial Sn atoms) and stoichiometry of the material [3.8, 3.16]. As it is now known, there are a number of existing ways in which SnO₂ films may be generated [3.8]. In this study, a cheap and more reproducible route for thermally oxidised metallic Sn thin films was opted for in comparison to using other highly complicated and costly procedures.

Thermally produced metal oxides are controlled by the diffusion process of metallic cations, anions coupled with electron transfer throughout the metal and metal oxide scale [3.37]. As a result, characteristic properties such as the electrical conductivity associated with the oxidized metallic thin films may vary under ambient environmental conditions placed during

fabrication procedures [3.23]. The resulting type of non-stoichiometric crystal metal oxide (n-type or p-type semiconductor) is dependent on the flux of ion diffusion and mass transfer throughout the metal oxide scale [3.37].

Thermal oxidation of metallic Sn thin films has been reported by a number of researchers [3.11, 3.19]. This work aims to find the perfect conditions in which SnO₂ thin films can be manufactured without the use of excessive high temperatures and external oxygen gas supplies placed a high vacuum. In the previous chapter (chapter 2), a detailed description of the environment that prompted for the adsorption of oxygen molecules on the films surface and subsequent diffusion of metallic Sn⁺² cations, O⁻² anions facilitated by a mass transport process. As formerly mentioned, such ambient experimental conditions have an influence on the characteristic properties on the now post oxidation Sn_xO_y thin film.

In this chapter, the experimental outcomes of the various characterisation analytical techniques as listed in chapter 2 from section 2.3.1 - 2.3.5 are given and discussed. The morphological section (3.2.1) investigates the microstructural surface changes Sn_xO_y films underwent during fabrication. This includes an average film thickness evolution studies, roughness and particle formation. Section 3.2.2 examines crystalline structural formation and stoichiometry of the various Sn_xO_y molecules present within the film. The compositional section 3.2.3 makes use of the absorbance and the characteristic vibrational properties of molecules via FTIR to detect the functional groups of films residing in the film. In addition, thickness and relative oxygen content (concentration) of the film was given by RBS surface analysis. In the final experimental results section 3.2.4, optical properties such as absorption and transmission advancement of films in the UV to visible region is scrutinised.

3.2 Experimental Results

3.2.1 Morphology

This section entails information pertaining to the morphological transformations that the Sn_xO_y thin films underwent as a function of increasing temperature. The scanning electron microscope (SEM) planar micrographs provided a means of physically visualizing topographical changes, while the Dektak 6M instrument was employed to evaluate the thickness evolution of presumably oxidized films. From there, energy dispersive x-ray spectroscopy (EDS) analysis was able to confirm whether in fact oxygen atoms had permeated through the metallic Sn thin film surface by bestowing elemental composition of selected regions. In addition, this segment also includes further discussions relating to these various characteristic techniques and their analytic results with regard to the study.

Morphological transformations of Sn thin films deposited on Si (100) and FTO substrates as a function of increased temperatures can be seen in Figure 3.1 and 3.5, accordingly. As-deposited and annealed metallic Sn thin films ranging from 200 - 400 °C can be viewed in the Figures 3.1 and 3.5 from (a) - (f) respectively. By observing the micrographs of the films deposited on the Si substrates, it is clear that the microstructural morphology of the thin films were not uniform. This can be deduced by observing the deep cracks and fractal-like structures such as nano-grains which were evident in both as-deposited and annealed samples after the deposition of Sn had taken place. In a similar manner to Laghrib et al. study, topographical features also display two distinct regions such as lighter areas in the form of grains presumably corresponding to the forms of the amorphous or crystalline structure of Sn_xO_y phases present in the film, and in contrast to this, darker areas found between the boundaries of the grain interfaces assigned to the exposed Si substrate [3.28]. This was

verified by the EDS results of spot analysis performed on all films and will be discussed in more detail later (see Figure 3.2).

From Figure 3.1.(a) - (c), Sn_xO_y films possess compact, randomly arranged, irregular sized and 'island-like' shaped grains with the exposed Si substrates between grain surface boundaries. Little to no microstructural changes can be seen for samples ranging from the as-deposited to the annealed 250 °C film. This indicates that the film retains its metallic phase after annealing for temperatures ≤ 250 °C. These observations agree with that reported by Chung et al. [3.13]. At 300 °C (Figure 3.1 (d)), a striking difference in the film's surface can be observed in comparison to the as deposited and annealed samples at lower temperatures. A more defined and well-pronounced mixture of randomly organised 'ellipsoid-like' and small 'spherical-like' grains are visible as they seem to nucleate directly on the substrate surface. In addition to these changes, it is apparent that Ostwald ripening had taken place since the exposure of the substrate along the grain surface boundaries are more pronounced, where agglomeration had progressed and is in agreement with the outcomes given by Abdullah et al. [3.1]. These morphological transformations reveal that the conversion from the metallic Sn to Sn_xO_y phases had occurred as a result of thermally induced oxidation. As annealing temperature advanced from 300 - 400 °C (figure 1.1 (d) - (f)), signs of mass transfer diffusion and coalescence between grains are obvious since grain boundary interfaces begin to merge and the amount of individual grains in the frame of the micrograph had significantly decrease as oxidation temperature increases. This evolution in morphological behaviour is once again in accordance to that reported by Chung et al. while Çakmak et al.'s study reveals that grain interface reactions are related to the existence of interference and defects along the grain boundaries which are responsible for the merging process, resulting in larger grains [3.12, 3.13].

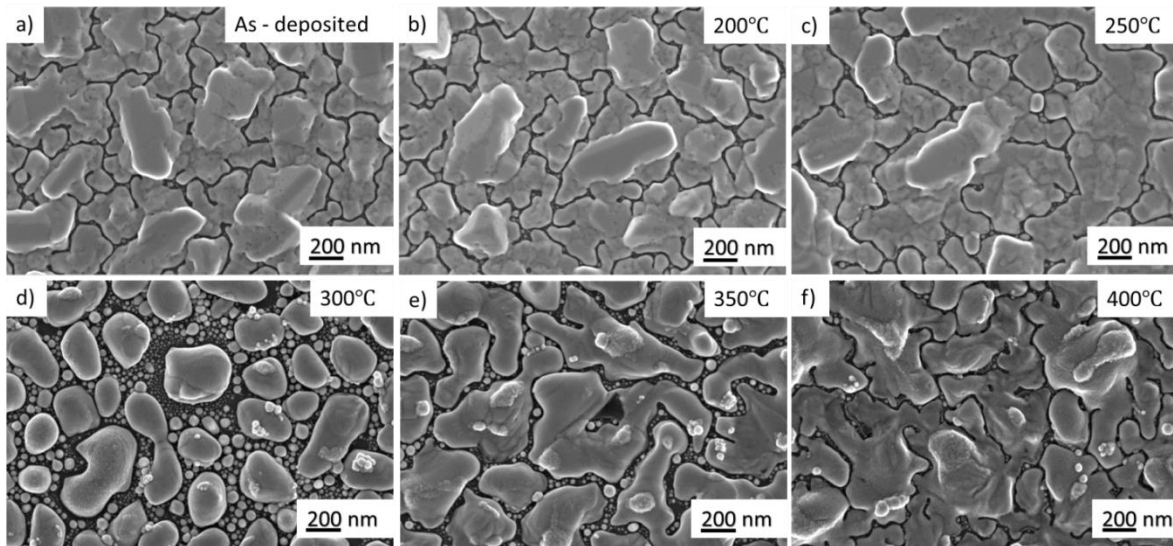


Figure 3.1: SEM planar micrographs of the deposited metallic Sn thin films on Si (100) substrates. (a) As-deposited, (b) film annealed at 200 °C (c) film annealed at 250 °C, (d) film annealed at 300 °C, (e) film annealed at 350 °C and (f) film annealed at 400 °C.

EDS was performed on all annealed Sn thin films, excluding the ones deposited on FTO substrates. This meticulous decision was executed because FTO substrates contain atoms of both Sn and O, which in turn, will impair the integrity of qualitative and quantitative results from EDS. In Figure 3.3 (a) - (d), EDS spot analysis was used to reveal the atomic percentage of constituent elements within the grains belonging to the film annealed at 300 °C. Qualitative and quantitative EDS results show that the selected grain in Figure 3.2 (a) attained an atomic % = 3.23 (Sn) and 68.58 (Si), while the spot in Figure 3.2 (b) acquired an atomic % = 0.48 (Sn) and 80.42 (Si). Even though, both designated spot areas in sample suggests that Si is a major constituent and that Sn is minor constituent, the relative variation in atomic % of both elements corroborates that the Si substrate had been exposed in the form of cracks between grain boundaries even after thermal deposition had taken place. In Figure 3.2 (f) a grain size distribution study of the sample annealed at 300 °C deposited on a Si (100) substrate revealed that the average grain size was found to be 303.71 ± 77.02 nm.

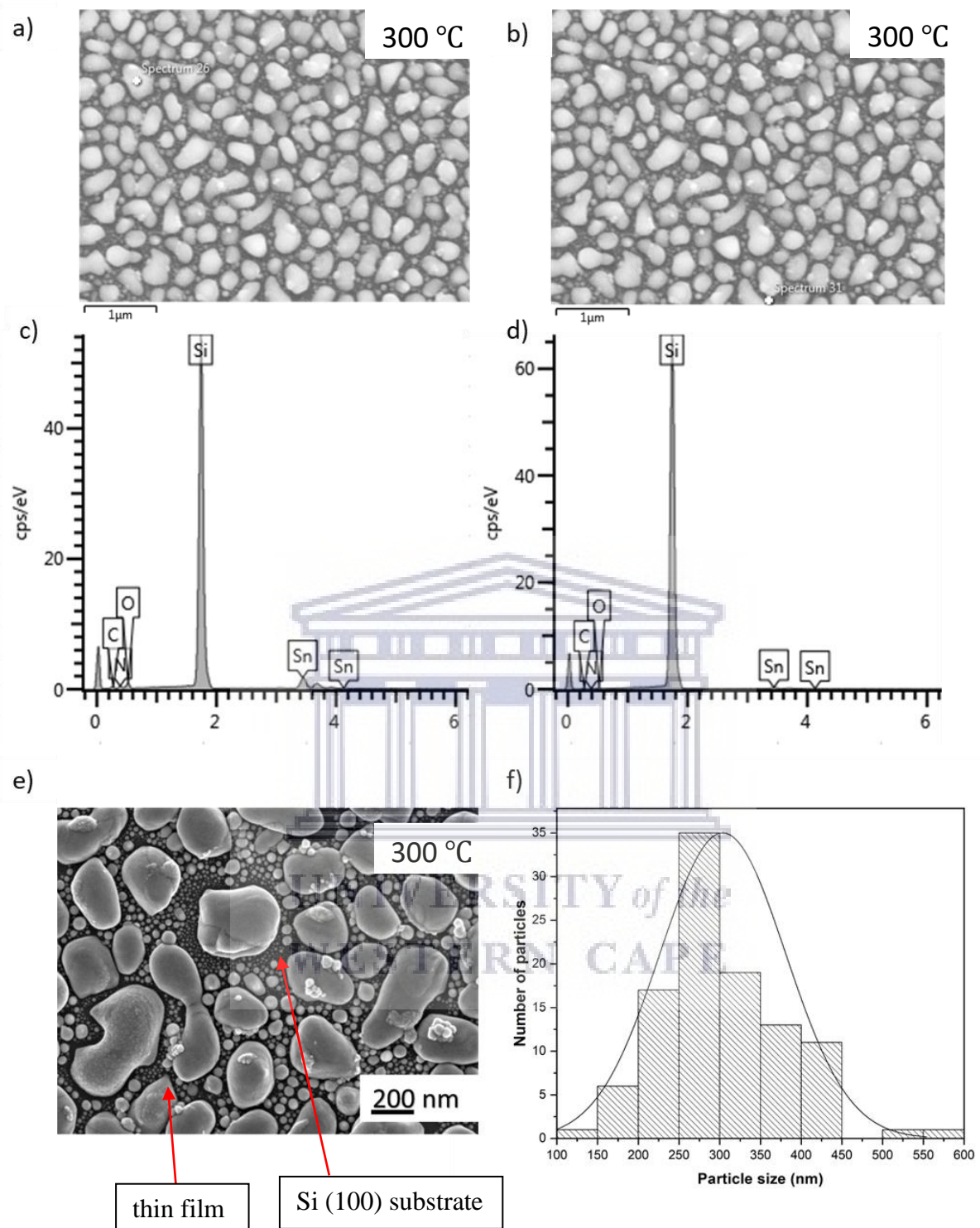
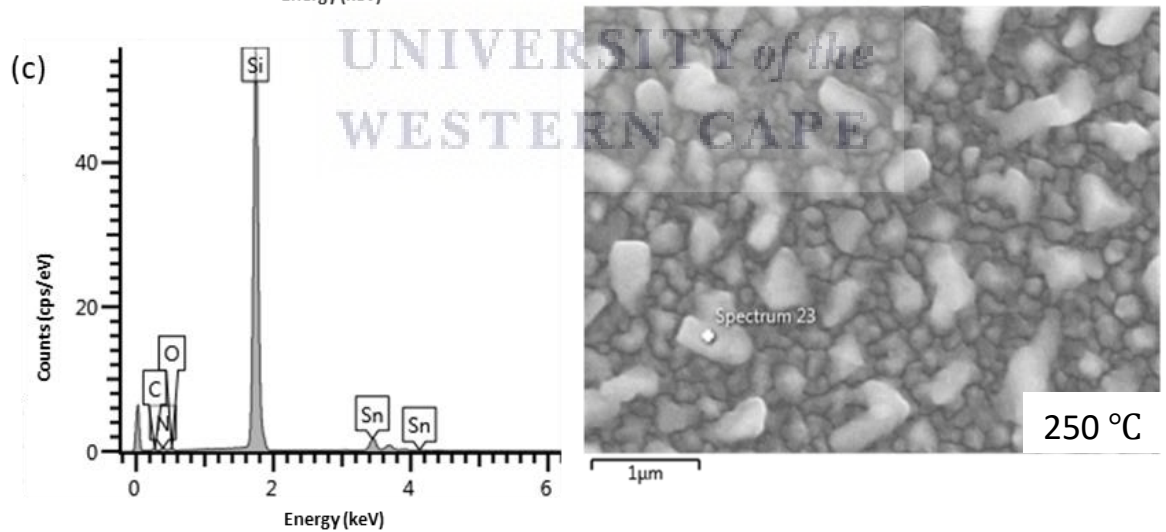
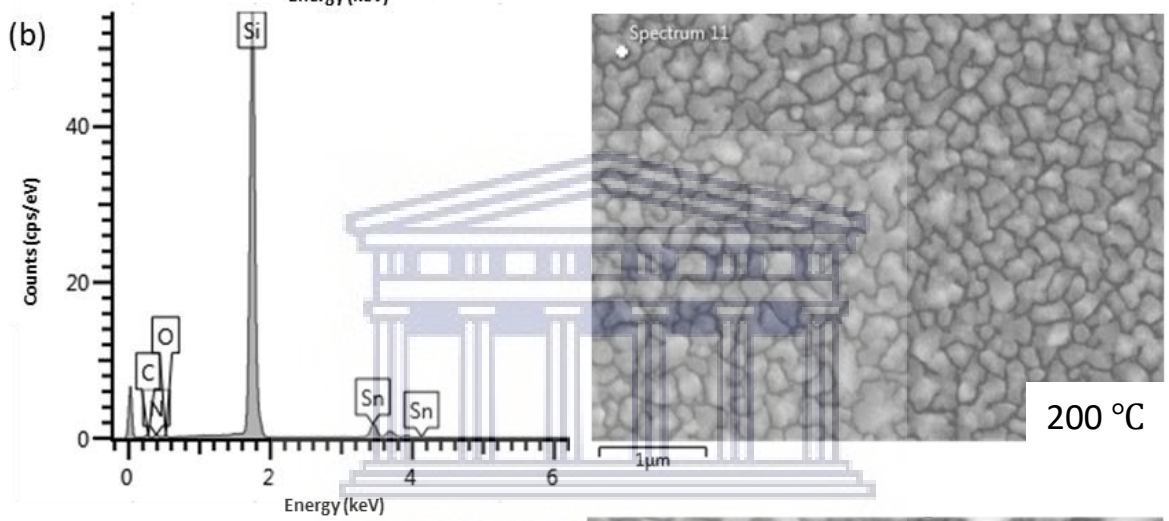
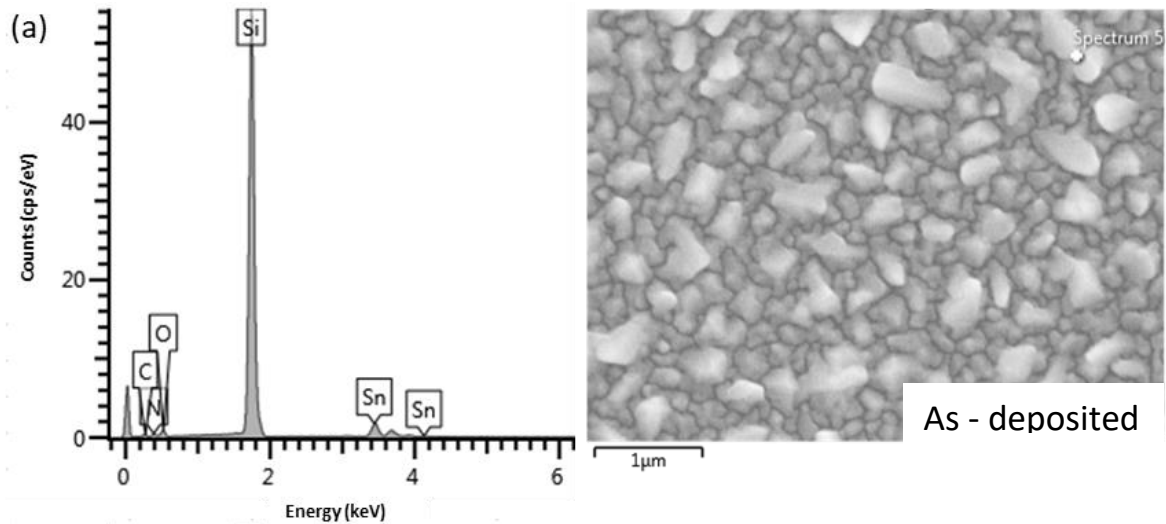


Figure 3.2: (a) and (c) EDS spot analysis of lighter grains on sample annealed at 300 °C, while (b) and (d) EDS spot analysis of lighter grains on sample annealed at 300 °C. From (e) - (f) Sn_xO_y phase grain size distribution for the thin film deposited on Si (100) and annealed at 300 °C.

In Figure 3.3 (a) - (f), the elemental composition of thermally oxidised Sn films deposited Si (100) substrates are given. In all samples shown in Figure 3.3, selected spots located on grains attained a predominance of Si and (carbon) C with an overall average in atomic percentage of approximately 69% and 22%, respectively. The high percentage of C may be attributed to the contamination found within the internal walls of the vacuum chamber of the microscopic system. Figure 3.4 relates the atomic percentage of Sn and O as a ratio of O/Sn with respect to annealing temperatures. By studying the image, it is clear that increasing amounts of O presents itself within selected grains with reference to increasing annealing temperatures. This indicates that O atoms had indeed permeated through the metallic Sn film as a function of increasing temperature. However, it is worth mentioning that quantitative microanalysis of lighter elements below sodium (Na, where $Z < 11$) like C, N, O, and F are difficult to quantify due to limited sensitivity [3.34]. In addition to sensitivity limits, it should be noted that EDS results are susceptible to surface contamination. Since oxygen (O_2) molecules are readily found in the atmosphere, it can thus easily be detected on the sample surfaces, and hence does not necessarily accurately indicate the concentration of O within the voluminous spot size selected during EDS analysis. With this said, the outcomes presented in Figure 3.4 should only be regarded as a qualitative measure and further analysis regarding the films stoichiometry will be investigated in section 3.2.3.



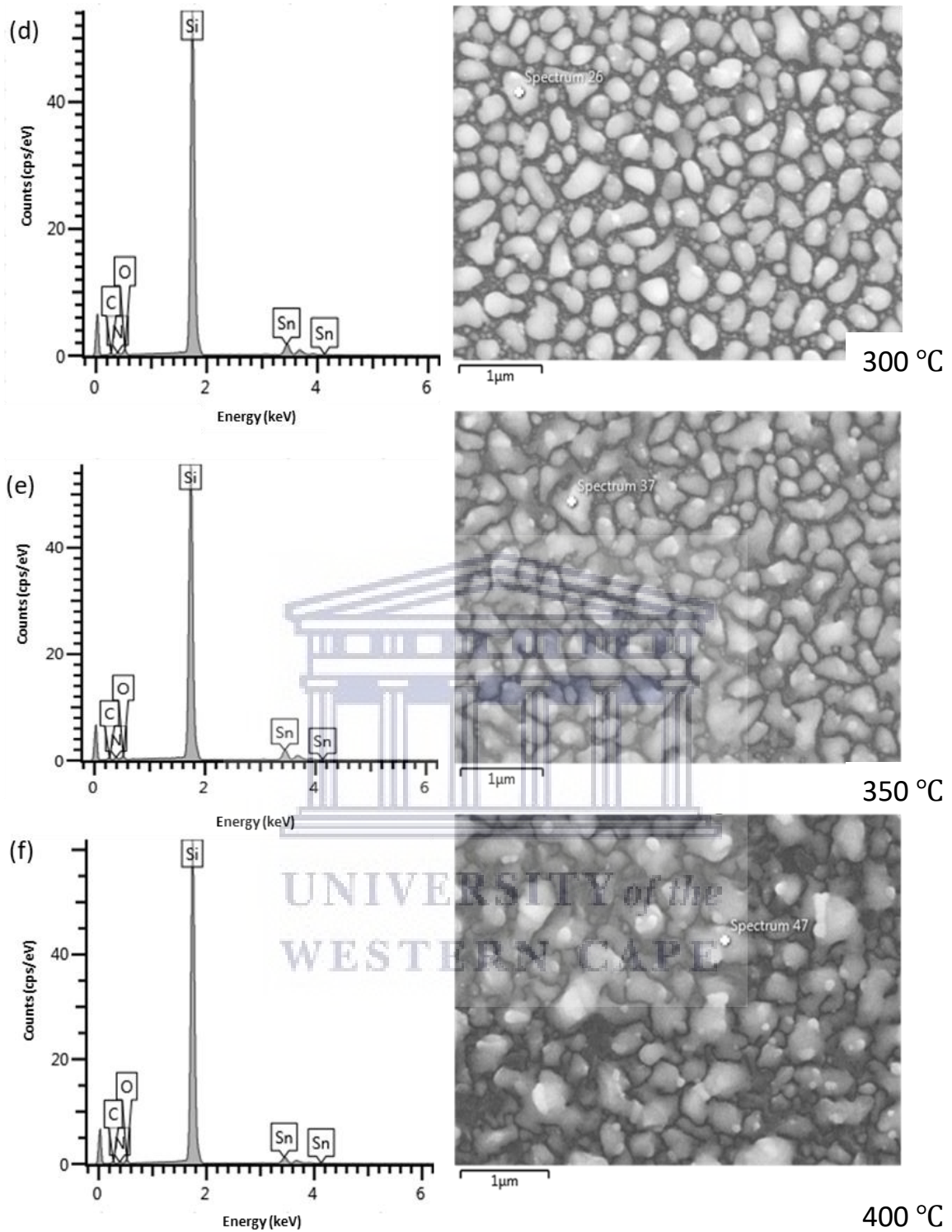


Figure 3.3: EDS elemental analysis (right) of selected grains belonging to various Sn_xO_y films (left), where (a) - (f) represent that annealed temperatures of the thin films such that: (a) as-deposited metallic Sn film, (b) 200 °C, (c) 250 °C, (d) 300 °C, (e) 350 °C and (f) 400 °C.

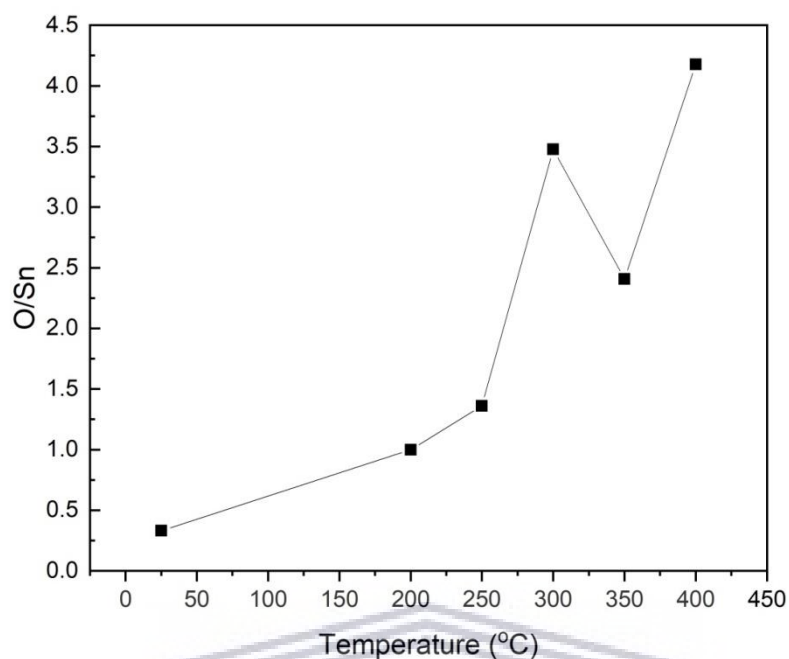


Figure 3.4: Presence of O and Sn atoms within Sn_xO_y grains as a function of the increasing temperature.

Similar to the behaviour of the film annealed at 200 °C which was layered onto a Si (100) substrate, the film annealed at 200 °C (figure 3.5 (b)) on the FTO substrate displays minimal amounts of grain-structure and morphological change in comparison to the as deposited metallic Sn sample. The film annealed at 250 °C (Figure 3.5 (c)), however, shows more defined grain structures in the form of smaller ellipsoids and circular-like shaped structures in comparison to the grains found in the 300 °C thin film deposited on the Si (100) substrate (see Figure 3.1 (d)). Furthermore, in addition to the smaller grain sizes to that of the ones formed on the Si (100) substrate, it is evident that the grains formed on the FTO substrate are more compactly arranged, and hence, less signs of substrate exposure can be seen. This variation in grain size and their distribution on the two types of substrates (FTO and Si (100)) may be attributed to multiple nucleation factors such as the substrate's crystallinity, chemical nature

of the substrate, imperfections in the substrate, and substrate surface cleanliness [3.33]. However in a similar manner, the evolution in surface morphology as a function of increasing annealing temperatures suggests that the change of the structural grains is due to the oxidation of the metallic Sn thin films. The grain size for the film annealed at 250 °C distribution is given by Figure 3.6 where an average size was determined to be 144.72 ± 58.18 nm. For annealing temperatures > 250 °C (figure 1.2 (d) - (f)), mass transfer diffusion is once again evident with an increased grain size structural features as annealing temperatures proceed.

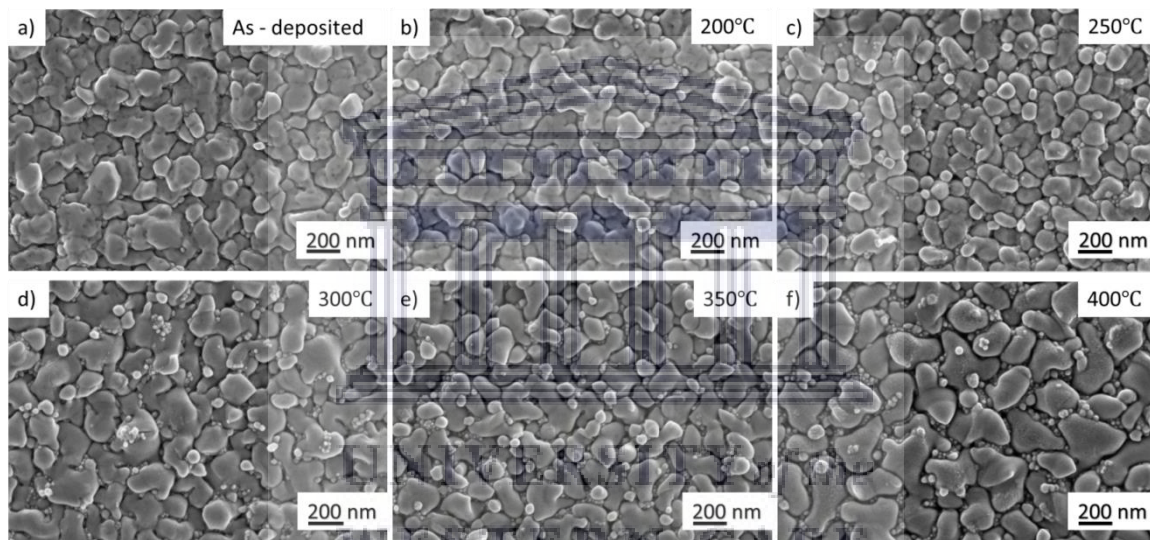
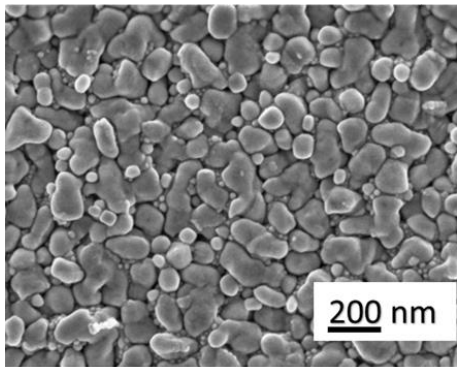


Figure 3.5: SEM planar micrographs of the deposited metallic Sn thin films on FTO substrates. (a) As-deposited , b) film annealed at 200 °C (c) film annealed at 250 °C, (d) film annealed at 300 °C, (e) film annealed at 350 °C and (f) film annealed at 400 °C.

a)



b)

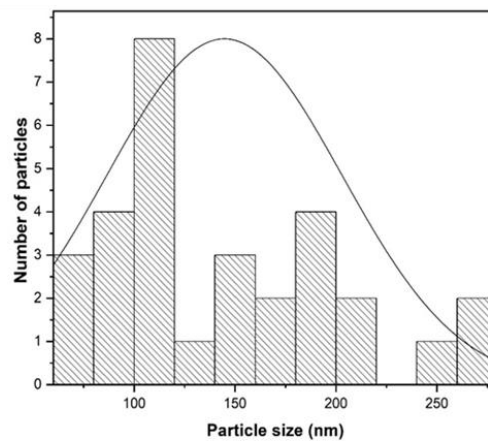


Figure 3.6: Sn_xO_y phase grain size distribution for the thin film deposited on FTO and annealed at 250 °C.

Figures 3.7 and 3.8 displays the average thickness (t_a) and roughness (r_a) for all Sn_xO_y thin films deposited on Si (100) substrates as a function of the annealing temperature. Throughout Figure 3.1 and 3.5 it is evident that surface morphology had changed as oxidation developed. Features such as grains and discontinuity are visible as previously stated. By analysing the progression of the film surface in relation to the thickness and roughness presented Figure 3.7 and 3.8, it is clear that oxidized films exhibit forms of recrystallization that ultimately gives rise to a greater film thickness and surface roughness for increased annealing temperatures. For oxidation temperatures ≥ 250 °C, a rapid increase in both t_a and r_a is observed, where each display a thickness from 47.37 - 103.92 nm and roughness of 3.03 - 5.48 nm variation under annealing conditions from as - deposited to 250 °C. This indicates that surface thickness and surface roughness are both influenced by the coalescence and migration of grains presented on the films surface. This observation is in agreement with Sefardjella et al. where they proposed that cracks along islands and grain boundaries which exposes the substrates acts as pathways that aid in the penetration of oxygen molecules via the film surface [3.43].

Moreover, Sefardjella et al. and Ko et al. both mention that the change in the film thickness is related to the oxidation process in which, both tin cation (Sn^{+2}) and oxygen anions (O^{-2}) diffused at the metal/oxide and, or oxide/gas interfaces. Furthermore, both studies mentioned that an increase in thickness suggests an enhancement of Sn^+ ion migration at higher annealing temperatures had taken place in the samples [3.27, 3.43]. Therefore, one may conclude that grain size and grain boundary grooving induces amplification in thickness as well roughness for elevated annealing temperatures [3.4].

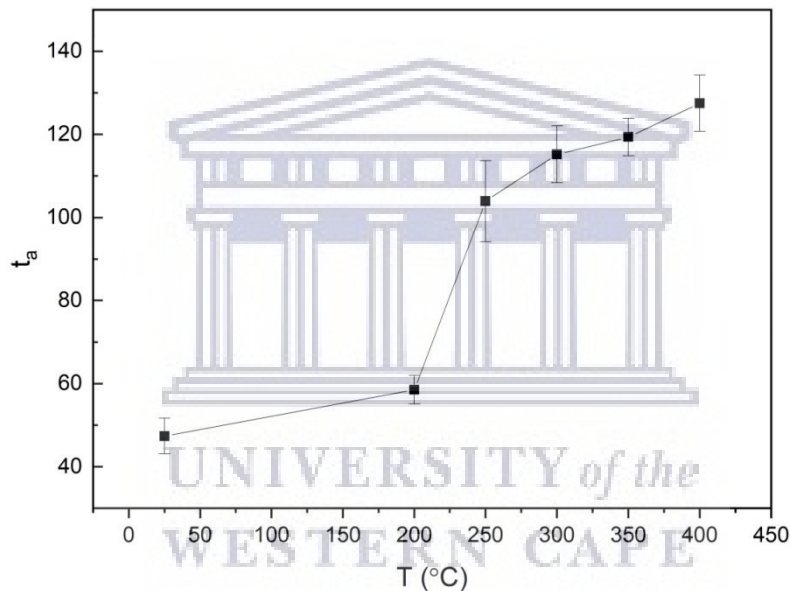


Figure 3.7: Thickness of all thin films deposited on Si(100) as a function of annealing temperature.

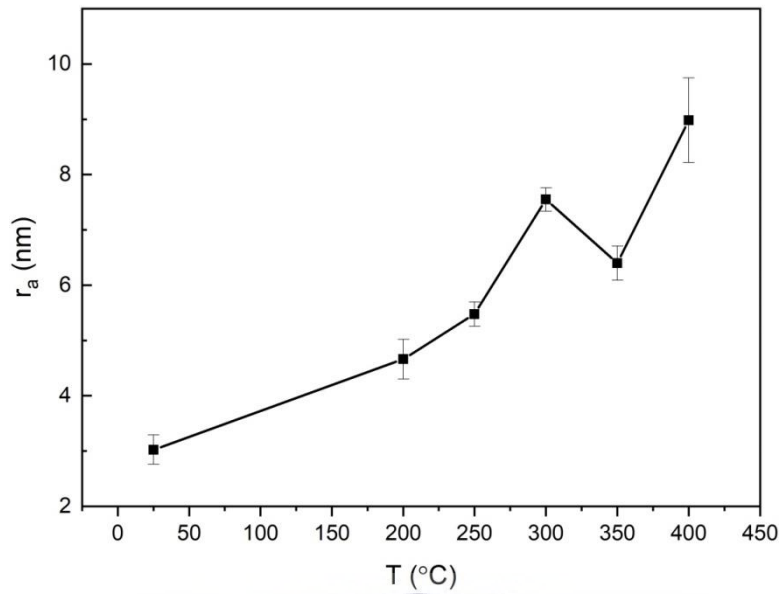


Figure 3.8: The average surface roughness of the thin films deposited on Si (100) as a function of annealing temperature.

From Figures 3.1 and 3.5 it can be observed that all Sn_xO_y thin films seem to exhibit the Volmer-Weber form of film growth, which is distinctively identified by the bond between the film and the substrate being weaker than the bonding between adatoms [3.4]. For films annealed 300 °C and 250 °C deposited and Si and FTO substrates respectively, the onset of nucleation growth is proposed to be controlled by the adatom - adatom interaction. Therefore, it can be deduced that diffusion of some form of O within Sn films had progressed as a function of increasing annealing temperatures, since earlier in this section it was mentioned that discontinuity (voids) between the grains of the thin films are clearly visible. Such discontinuity between grains of the thin film consequently exposes the substrates, where this phenomena is more distinctive for films deposited on Si(100) substrates [3.9, 3.4]. According

to Birks et al. these apparent grains and voids that expose the substrate surface, are all indicative of growth stresses experienced by the oxide during the oxidation process [3.9].

As outlined by Perez et al. and Andersson et al.: when adatoms like O diffuse, the surface film behaviour becomes more complex as small particles merge to form larger grains [3.37, 3.4]. In the process of surface diffusion, the coalescence and morphological rearrangement as shown for films oxidized $> 300\text{ }^{\circ}\text{C}$, is suggestive of relaxation of tensile stresses formed upon grain boundary formation [3.18]. It must however, be noted that such morphological rearrangement cannot independently relieve the compressive stresses related to the emergence surface stress effects due to island growth independently [3.8]. Tensile stresses caused by the formation of grain boundaries are then alternatively relieved by the diffusion of adatoms on the free surface of the film. Subsequently, these adatoms are then trajected downwards into the grain boundary by the process of diffusion. This diffusion creeping behaviour is analogous to that of the Coble creep mechanism in bulk polycrystals [3.18, 3.21]. The Coble creep process is regulated by grain boundary diffusion in conjunction with low temperature power creep law caused by dislocation of pipe diffusion [3.31]. In this instance, surface coble creep of the oxidized Sn thin film relieves tensile stress by merging in a grain boundary zipping configuration as a means to adhere to the Sn metal interface [3.9, 3.18, 3.21]. On the other hand, if the aspect grain ratio of the greater than that of 3:1, the creeping is unable to relieve other stresses such as capillary-induced growth stresses situated within the central region of the grain, unless some interfacial shear occurs [3.18].

In addition, Asgarya et al. noted that diffusion along linear and planar surface defects is often faster than diffusion in a lattice, since they permit easy diffusion paths. This is due to atoms being more mobile at grain boundaries than through the crystal lattice. Fast diffusion along grain boundaries acts as a crucial component in most metallurgical processes especially in

one involving net mass is transported along boundaries. Asgarya et al. also states “that this movement in net mass acts as sources and sinks for the fluxes of atoms. Lattice diffusion generally requires the highest activation energy and is the slowest path for mass transport, while the activation energy for diffusion along grain boundaries and interfaces are relatively less” [3.6].

3.2.2 Phase Transitions

The structural properties, crystallinity and phase transitions of the thermally oxidized Sn thin films were investigated and verified by x-ray diffraction (XRD). Figure 3.9 displays the XRD spectra for the as-deposited and annealed metallic Sn thin film samples on Si (100) substrates. Identification of crystal patterns regarding the structure of the thin films were mainly emphasised on those that were deposited on Si (100) substrates for the same reason as that mentioned in section 3.2.1. Diffraction patterns were recorded from $2\theta = 10^\circ - 100^\circ$, albeit that no crystallinity information is present in the range from $2\theta = 45^\circ - 110^\circ$. Therefore, only results from $2\theta = 15^\circ - 45^\circ$ is shown. All XRD peaks were identified by the Inorganic Crystal Structure Database (ICSD). By observing the spectra as a function of increasing temperature in Figure 3.9, notable signs of thermal oxidation of Sn are present since multiple Sn_xO_y phases were formed in every sample. In addition to Si peaks present, these Sn_xO_y multiphases also suggests that the thin films are composed of a polycrystalline nature.

Strong peaks predominantly visible in the as-deposited thin film and films annealed at 200 °C and 250 °C are located at positions $2\theta = 30.87^\circ$ and $2\theta = 32.26^\circ$, and were indexed to the (200) and (101) diffraction planes. These peaks belong to the Sn body centred tetragonal (I41/amd) crystal structure and was verified by obtaining lattice parameter values of a =

5.798 Å and $c = 3.164$ Å. A drastic decrease peak in the intensities belonging to these Sn phases takes place for annealing temperatures ≥ 300 °C. This is an indication that thermal oxidation had commenced at these temperatures, and therefore, substantiates the presumption made in the morphological section 3.2.1 that films remained in their metallic state ≤ 250 °C. Phases of SnO, SnO₂ and C₂O₄Sn appear to co-exist in the sample annealed at 300 °C indicating the initiation of pure Sn_xO_y phases being formed. Eventhough carbon bonded related impurities of the C₂O₄Sn (tin oxalate) phases are evident, they are more prevalent at temperatures ≤ 250 °C, and are no longer visible for annealing temperatures > 300 °C. This demonstrates that impurities had diminished as higher annealing temperatures had progressed. Furthermore, in Kitabayashi and Koga's study, they report that formation of SnO₂ structures may be achieved by the oxidative decomposition of tin oxalate [3.26].

Phases present at 300 - 400 °C are assigned to the SnO tetragonal (P4/nmm) crystal structure where diffraction pattern peaks appeared at $2\theta = 18.55^\circ$, 29.95° and 37.36° , accordingly. This corresponds to the (001), (101) and (002) diffraction planes. Additionally for the same samples, the SnO₂ tetragonal (P4₂/mmm) crystal structure's miller indices of the (110) and (101) are indexed to the positions $2\theta = 27.00^\circ$ and $2\theta = 33.55^\circ$, respectively. Lattice parameters are calculated to be $a = 3.816$ Å and $c = 4.782$ Å for the SnO phase, and $a = 4.668$ Å and $c = 3.256$ Å for the SnO₂ phase by using Eq 2.9. Verification of crystallographic phase structures are confirmed by the theoretical lattice parameters presented in Table 3.1.

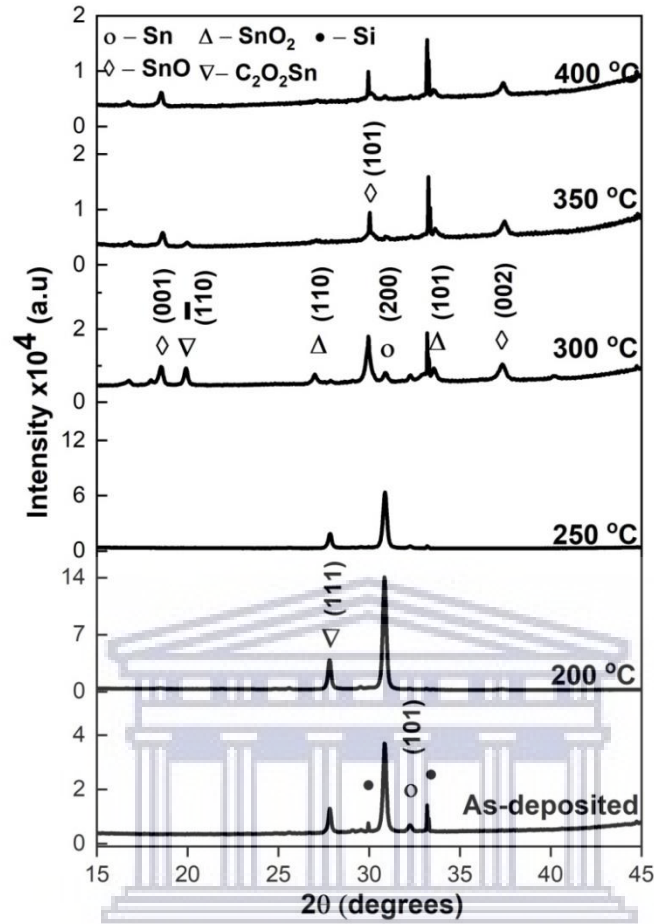


Figure 3.9: XRD of the as-deposited thin film and the annealed samples from 200 - 400 °C.

Table 3.1 provides the lattice parameters for all Sn_xO_y phases found within the XRD spectra presented by Figure 3.5. Lattice parameters denoted with a subscript “e” and “t” represent the experimental and theoretical values provided by the ICSD respectively. All Sn_xO_y phases belong to the tetragonal crystal structure and can be calculated by using the relation as follows (see Table 2.2):

$$\frac{1}{d} = \left(\frac{h^2 + k^2}{a^2} \right) + \frac{l^2}{c^2} \quad (\text{Eq.3.1})$$

Table 3.1: Sn_xO_y phase lattice parameters present in thin film samples.

Crystal Structure	hkl	a_e (Å)	c_e (Å)	a_t (Å)	c_t (Å)	$(c/a)_e$	$(c/a)_t$
Sn	(200)	5.798	3.164	5.819	3.175	0.545	0.545
	(101)						
SnO	(001)	3.816	4.782	3.780	4.790	1.250	1.267
	(101)						
	(002)						
SnO ₂	(110)	4.668	3.256	4.720	3.170	0.697	0.671
	(101)						

According to literature listed by Guo et al.: during oxidation, the transformation from Sn to SnO₂ does not transpire directly, but passes through the SnO phase first. Since diffraction patterns belonging to Sn and SnO are still apparent in the films from 300 - 400 °C, this implies that oxidation within the films are incomplete [3.19]. This therefore gives the reasoning behind the poor crystalline nature of the phases present in the film including that of SnO₂. Nevertheless, given that the aim of the study revolves around the formation crystalline SnO₂, the rest of the analysis from this point onwards will be concentrated around the diffraction patterns corresponding to that of SnO₂. Since the (101) diffraction peak belonging to SnO₂ is the only one available throughout the films annealed from 300 - 400 °C, the Williamson-Hall analysis cannot be performed, and therefore the examination of the

crystallite size will centre around this plane. Strain and crystallite size of a given phase within a crystal may be determined by the Debye Scherrer equation such that:

$$D = \frac{k\lambda_{CuK\alpha}}{\beta \cos\theta} \quad (\text{Eq. 3.2})$$

Where D is the crystallite size in nm, k is a constant equal to 0.90, $\lambda_{CuK\alpha}$ is the wavelength of radiation 1.54056 Å, β is the full peak width at half-maximum intensity and θ is the peak position [3.20, 3.25]. The lattice strain ε_s in the film also causes broadening of the diffraction peak and is calculated by the relation:

$$\varepsilon_s = \frac{\beta}{4 \tan\theta} \quad (\text{Eq.3.3})$$

Table 3.2 provides the SnO₂ crystallite sizes formed within Sn_xO_y films from 300 - 400 °C. By observing the values given in table 3.2, it can be reported that the crystallites belonging to the formation of the SnO₂ phase orientated in the (100) direction residing in the Sn film annealed at 300 °C experiences the most amount of lattice strain. Such strain experienced by the crystal lattice can be brought on by the introduction of new phase transformations that occur during oxidation. Therefore such a result is expected since the resultant Sn_xO_y film oxidized at 300 °C consists of the most crystalline phases in comparison to those annealed at 350 and 400 °C. Reduced strain for films Sn_xO_y oxidized under 350 and 400 °C thermal conditions is an indication of film relaxation as suggested by the morphology section. In addition, the reduction in β resulting in a larger crystal size is suggestive of an improvement of crystalline formation.

The crystal growth can generally be expressed by the following parabolic equation:

$$D^m - D_0^m = k_r e^{\left(\frac{-Q}{RT}\right)} t \quad (\text{Eq.3.4})$$

Where D is the crystallite size at a specific time t , D_0 is the initial crystallite size, k_r is a constant, T is the absolute temperature, Q is the activation energy for a diffusion process, and m is the growth exponent, which can be assigned various values from 2 - 4 based on the microstructure and the growth mechanism. For a growth mechanism where crystal growth is governed by grain boundary mobility, $m = 2$; while conditions where crystal growth is controlled by pore mobility, $m = 3$ and $m = 4$. In the latter crystal growth, the mechanism is specifically allocated for diffusion and gas transport for $m = 3$, while the mechanism denoted for surface diffusion is for $m = 4$. It should be noted that Eq. 3.4 is only applicable based on the assumption that the crystal size distribution function is time invariant under circumstances of normal growth. As the oxidation process in this study is isochronal, Eq.3.4 may be reduced in the following manner [3.11]:

$$D^m - D_0^m = k_0 e^{\left(\frac{-Q}{RT}\right)} \quad (\text{Eq.3.5})$$

Such that k_0 is a constant that is dependent on the oxidation time. Figure 3.10 (a) displays the growth of SnO_2 (101) oriented crystallite size D as a function of increasing oxidation temperature, T , i.e. from 300 - 400 °C. From Figure 3.10 (c) - (d) the evolution of D^m is given as a function of $1/T$ for values of $m = 2, 3$ and 4.

Table 3.2: SnO_2 crystallite (101) orientated diffraction peak properties.

Annealing T (°C)	T(K)	Position θ (°)	FWHM (°)	D (nm)	Strain ($\times 10^{-3}$)
300	573.15	33.55	0.21926	37.842	3.173
350	623.15	33.62	0.18484	44.897	2.670
400	673.15	33.55	0.17336	47.861	2.509

Table 33: Arrhenius equation fit parameters for the formation so SnO₂ (100) crystallites.

Arrhenius equation fit	a	B	Error in fit R ² (COD) (×10 ⁻¹)
m = 2	3.024×10 ⁻²	1.72279	9.511
m = 3	4.630×10 ⁻³	2.50225	9.504
m = 4	6.524×10 ⁻⁴	3.22825	9.509

By using the coefficient of determination R^2_{COD} for the variation of D^m as function of $1/T$, from fit in the form of $y = ae^{(-bx)}$, it is then possible to establish what growth mechanism was mainly responsible for the crystallite sizes. The interpolated values of R^2_{COD} for $m = 2$, $m = 3$, and $m = 4$ were computed to be 0.9511, 0.9504, and 0.9509, accordingly. This suggests that the crystal growth mechanism responsible for the formation of SnO₂ was a combination of $m = 2, 3$ and 4 since they all obtain a similar value of ≈ 0.95 . However, the best approximation for crystallite growth is $m = 2$ which is indicative of grain mobility within the Sn thin films and was induced by an activation energy of $Q = 14.32 \text{ kJ.mol}^{-1}$. Boulainine et al. performed a similar study and obtained a result of $Q = 112 \text{ kJ.mol}^{-1}$, under the conditions where $m = 4$ was established to be the driving force behind the formation of SnO₂ (101) orientated crystallites [3.11]. This result provided by Boulainine et al. investigations suggests that the crystallite growth was governed by that of pore surface mobility corresponding to $m = 4$ [3.11].

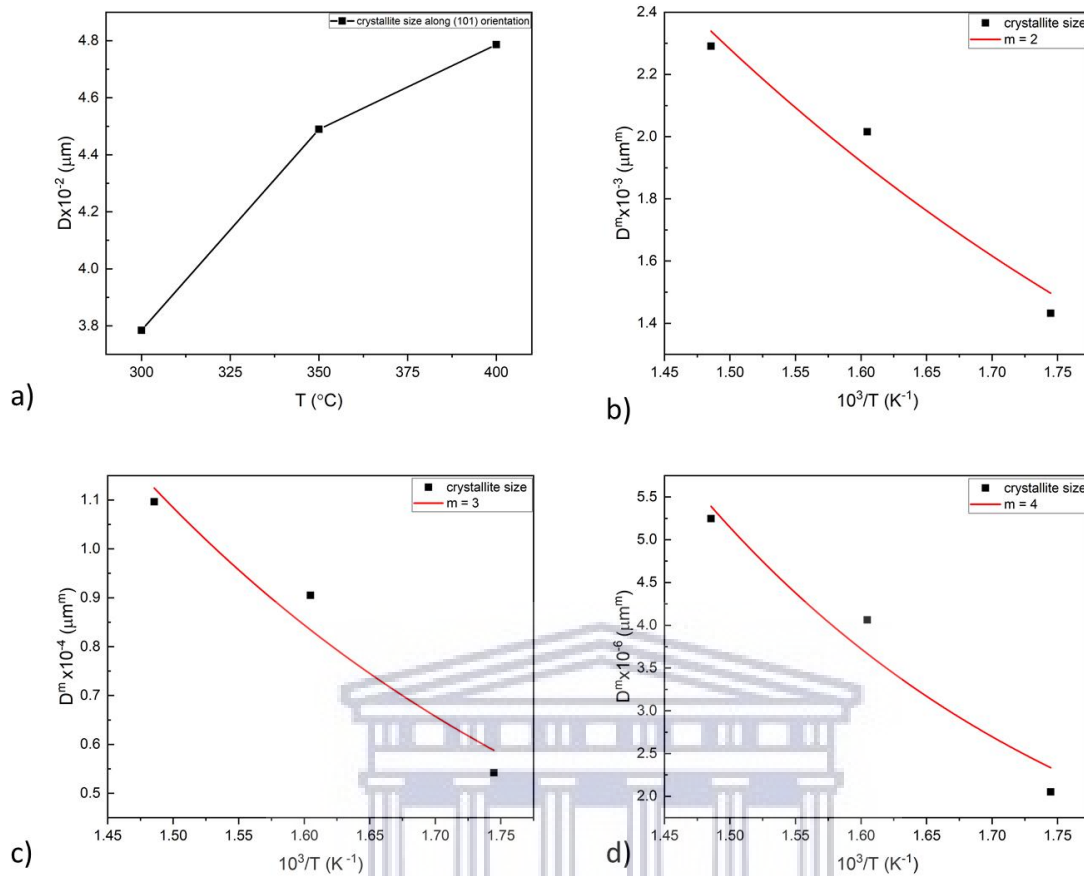


Figure 3.10: (a) Formation of SnO_2 crystallite sizes along the (101) direction residing in 300, 350 and 400 °C annealed Sn_xO_y films. (b) - (d) Arrhenius fit on crystallite sizes for diffusion mechanisms $m = 2, 3,$ and 4.

Interestingly, it is quite obvious that the diffusion through grain mobility falls in line with the Coble creep mechanism. Coincidentally, this is the exact same mechanism used to describe the evolution of the oxidized Sn thin films morphology (see Figures 3.1 and 3.5), and therefore, this deduction falls well in agreement to what is proposed in the morphological section 3.2.1. As previously mentioned, Coble creep behaviour is brought on by the tensile and compressive stresses experienced by the film when migrating from equatorial regions of grains to polar regions. Tensile stresses generate hydrostatic compression in equatorial

regions due to volume conversions, coupled with hydrostatic tension in polar regions [3.15]. Generally, in Coble creep diffusion, the activation energy of grain boundary diffusion is low, and the cross-sectional area available for diffusion along grain boundaries are outweighed by diffusion of the bulk. Therefore, it is for this reason that this mechanism is predominant at relatively low temperatures and form samples with fine grain sizes [3.15].

3.2.3 Compositional Properties

3.2.3.1 Fourier Transform Infrared Spectroscopy (FTIR)

The FTIR technique was used to scrutinize the chemical bonding status and functional groups present in the Sn_xO_y thin films. In transmission mode, functional groups may be identified effortlessly by the absorption peaks and their associative band positions at certain frequencies. In this manner, information relating to the structure of a material is then consequently revealed. Band positions and numbers of the absorption peaks are influenced by the crystalline structure, chemical composition as well as the morphology of the material [3.41].

Figure 3.11 exhibits the absorption coefficient of annealed thin films as a function of wavenumber frequency from $4000 - 400 \text{ cm}^{-1}$. By examining the overall spectra, one is able to observe the existing functional groups and their characteristic vibrational absorption peaks located at their corresponding IR bands. For all the thermally oxidized Sn films from $200 - 400 \text{ }^\circ\text{C}$, a weak broad band is evident in the range of $3946 - 2765 \text{ cm}^{-1}$. These vibrations are assigned to the O – H stretching hydroxyl group belonging to water molecule absorbed on the surface [3.41, 3.39, 3.26]. Furthermore, situated at 2337 cm^{-1} , a stretching O = C = O band

can be detected in samples from 200 - 350 °C and is ultimately formed as a result of the adsorption of carbon dioxide molecule present within the atmosphere while samples were either being handled or in the process of being annealed [3.42]. The bands located at 1467 cm^{-1} , 1231 cm^{-1} and 1033 cm^{-1} correlate to the C – H, C – O and C – N bonds associated with the alkane (methane), alkyl aryl ether and amines compound class, respectively [3.42, 3.46]. All the above mentioned molecular bonds are present in the films and are naturally occurring organic compounds. In addition, the disappearance of the O = C = O peaks and reduction of intensities belonging to the molecular vibrations of O – H, C – H, C – O and C – N from 200 - 400 °C are indicative of purging at higher annealing temperatures. This reduction of band intensities is formally known as a hypochromic shift, and is associated with a decrease in concentrations belonging to impurity molecules within the annealed thin film samples.

Moving towards the region of longer wavelengths known as the fingerprint region (see Figure 3.12) of the spectrum, the major absorption peaks are associated with the formation of SnO and SnO₂ in the range 660 - 420 cm^{-1} . Three bands manifests around positions 659 cm^{-1} , 534 cm^{-1} and 420 cm^{-1} in the final sample annealed at 400°C due to the anti-symmetric stretching molecular vibrations of the Sn – O – Sn, Sn – OH and O – Sn – O bonds, respectively [3.39, 3.41, 3.26].

The appearance of the stretching modes of Sn – OH and Sn – O vibrations are present throughout all annealed samples. For samples 200 °C and 250 °C, the presence of Sn – OH bond can be detected at 556 and 514 cm^{-1} , accordingly. While, for samples 300 - 400 °C, the vibration of Sn – OH emerges at 534 cm^{-1} . In a similar way, Sn – O band also exhibits some slight change in vibrational band positions within the oxidized Sn film. For the thin films annealed at 200 °C and 250 °C, two peaks are detected around 420 - 500 cm^{-1} which may be

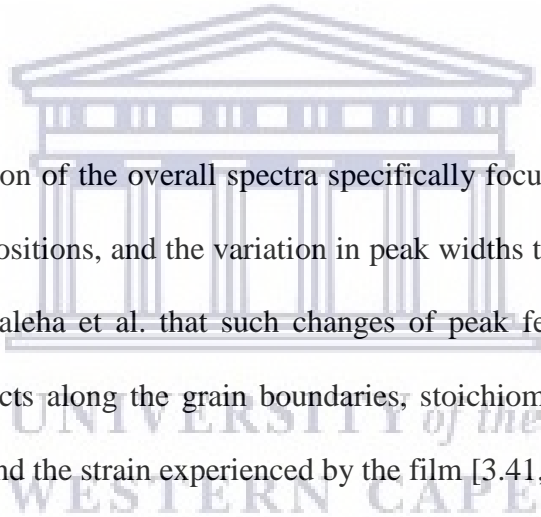
assigned to the vibrations belonging to the O – Sn – O bond, accordingly. For both films however, the most prominent peak that verified the presence of O – Sn – O bonds emerges at 495 cm^{-1} for the annealed sample at $200\text{ }^{\circ}\text{C}$, and at 446 cm^{-1} for the film annealed at $250\text{ }^{\circ}\text{C}$. The same bond frequency apparent for the film oxidized at $300\text{ }^{\circ}\text{C}$. Above these temperatures, more pronounced peaks associated with O – Sn – O vibrations were ultimately situated around 420 cm^{-1} in both annealed film films at $350\text{ }^{\circ}\text{C}$ and $400\text{ }^{\circ}\text{C}$.

Residing in the final Sn_xO_y thin films annealed at $350 - 400\text{ }^{\circ}\text{C}$, new peaks presents itself by the anti-symmetric stretching vibration belonging to formation of the Sn – O – Sn bond. For the film oxidized at $350\text{ }^{\circ}\text{C}$, the bond is centred around 568 cm^{-1} , while for the film oxidized at $400\text{ }^{\circ}\text{C}$, the bond appeared around 660 cm^{-1} [3.41]. This vast shift in vibrational frequencies can be explained by the change in bond environment experienced by the film as disorder in the bonds lesson as a function of increasing annealing temperatures. The formation of the Sn – O – Sn bond within the films is an indication of interaction between cation and oxygen bond formed within the film, and according to Priya et al., is caused by the “surface-bridging oxide formed by hydroxyl groups.” Thus, implying the formation of SnO and SnO₂ bridge functional group present in the film annealed at $350 - 400\text{ }^{\circ}\text{C}$ [3.38].

Deconvoluted peaks within the region $700 - 400\text{ cm}^{-1}$ were successfully obtained using a Gaussian fit function, as given in Figure 3.13. In Table 3.2, vibrational band features such as FWHM, intensity, and the integrated area beneath the peaks pertaining to the development of SnO and SnO₂ bonds within annealed thin films are given. The rise of annealing temperatures is linked to a gradual decrease in FWHM in both Sn – OH and Sn – O bonds. For Sn – OH bands, an overall gradual decrease in FWHM is detected from $78.40 - 47.04\text{ cm}^{-1}$, as for Sn –

O bands, FWHM values are reduced from 78.40 - 25.61 cm^{-1} corresponding to films exposed to temperatures from 200 - 400 $^{\circ}\text{C}$, accordingly.

In conjunction to these variations in band widths, a change in band intensities are also visible. For Sn – OH peaks, intensities of 6518.40, 1589.68, 493.79, 158.90 and 570.60 cm^{-1} are identified for annealed films up to 400 $^{\circ}\text{C}$. Likewise for Sn – O molecular vibrations in samples leading up to 400 $^{\circ}\text{C}$, band intensities of 5922.07, 1633.74, 300.30, 264.80 and 499.38 cm^{-1} are listed for annealed samples. By examining the intensity of SnO and SnO₂ molecular vibrations, a dramatic decline in band intensity experienced by both Sn – OH and Sn – O modes from 200 - 350 $^{\circ}\text{C}$ is apparent, until a final increase in intensity for samples oxidized at 400 $^{\circ}\text{C}$ is noted.



As a complete interpretation of the overall spectra specifically focused on the hypochromic shift, the change in band positions, and the variation in peak widths that have been remarked. It has been reported by Saleha et al. that such changes of peak features are connected to disorders resulting in defects along the grain boundaries, stoichiometric changes, the grain size of the nanoparticles, and the strain experienced by the film [3.41, 3.3].

Overall, the occurrence sharper peaks, decrease in FWHM, and peak positions settling at higher temperatures explicitly in films from 300 - 400 $^{\circ}\text{C}$, signifies that more impurities, stresses and vacancies were present within films oxidized at lower temperatures ≤ 300 $^{\circ}\text{C}$. It should also be mentioned that the overall decrease of band intensities related to carbon bonds as a function of higher annealing temperatures suggests that concentration of carbon in the films had decreased and that higher temperatures had removed some impurities within the film. Similar behaviour has been reported in section 3.2, where carbon phases had diminished as a function of increased annealing temperatures. Then, by focusing on the bands which are

associated with SnO and SnO₂ formation, it can clearly be seen that at temperatures > 300 °C that an increase in band intensities was detected. This signifies that in the film annealed at 400 °C experienced an improvement of SnO and SnO₂ concentration within the film. By taking this observation into consideration, coupled with the decrease in characteristic SnO and SnO₂ band widths, it can then be deduced that a greater order of bond vibrations for samples annealed from 300 - 400 °C was present.

Based on the previous remarks within this section, it can be inferred that, as oxygen (O) atoms were introduced to the Sn lattice within the film through the process diffusion during oxidation. Defects along the grain boundaries instigated forces experienced by atoms in the lattice of the film. Such forces implemented in the crystal lattice manifested in the form tensile and compressive stresses. Consequently, these stresses triggered a change in bond positions. Eventually, once annealing temperatures progressed from 300 - 400 °C, compressive and tensile stresses became less pronounced due to the decrease in lattice energy belonging to film surface caused by a decrease in volume of inflicted by oxygen atoms. Subsequently, the film then began to renormalize and organized into a metal oxide, thus advocating film recrystallization [3.7]. This is phenomena is analogous to the deductions made in the morphological and phase transition section in 3.2 and 3.3, accordingly.

Table 3.4: Vibrational properties of Sn_xO_y films.

Sample	Frequency (cm^{-1})	Assignment	FWHM (cm^{-1})	Intensity (cm^{-1})	Error in fit R^2 (COD)
400 °C	420	Stretch O – Sn – O	24.38145	499.377	0.94953
	534	Stretch Sn – OH	45.33019	570.603	
	659	Stretch Sn – O – Sn	21.04343	171.119	
350 °C	420	Stretch O – Sn – O	22.29976	264.800	0.96086
	534	Stretch Sn – OH	31.90744	158.903	
300 °C	446	Stretch O – Sn – O	42.17302	300.297	0.991
	534	Stretch Sn – OH	32.20082	493.794	
250 °C	446	Stretch O – Sn – O	37.39425	1633.735	0.99319
	514	Stretch Sn – OH	135.64342	1589.684	
200 °C	495	Stretch O – Sn – O	66.652	5922.065	0.9987
	556	Stretch Sn – OH	99.597	6518.399	

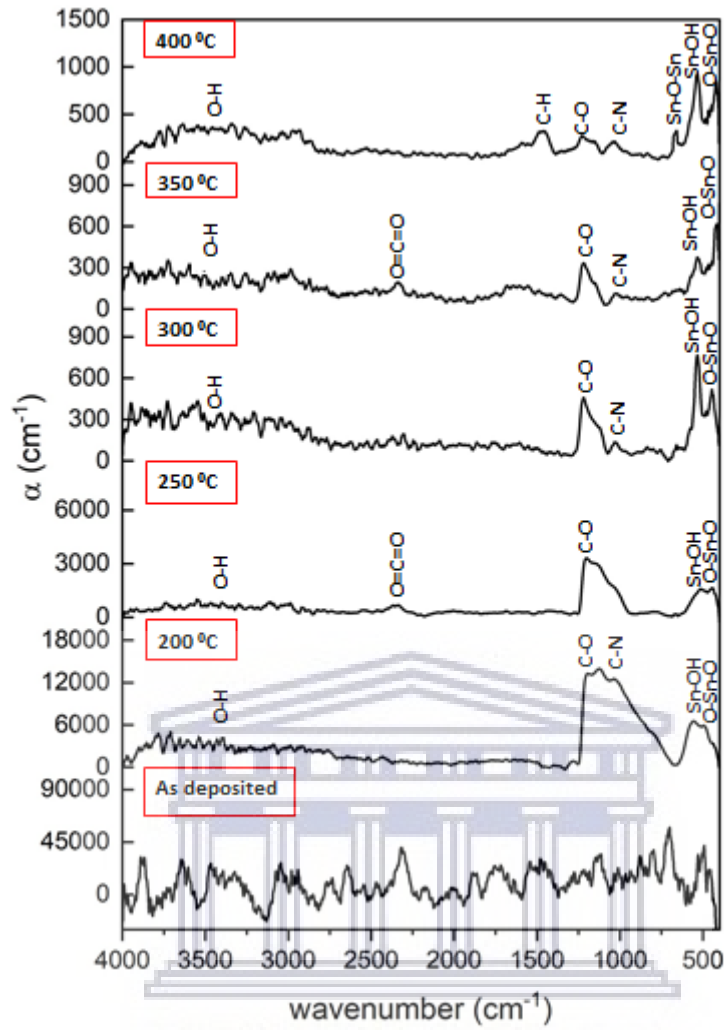


Figure 3.11: Overall FTIR spectra for as-deposited and annealed Sn_xO_y samples from 200 - 400 °C.

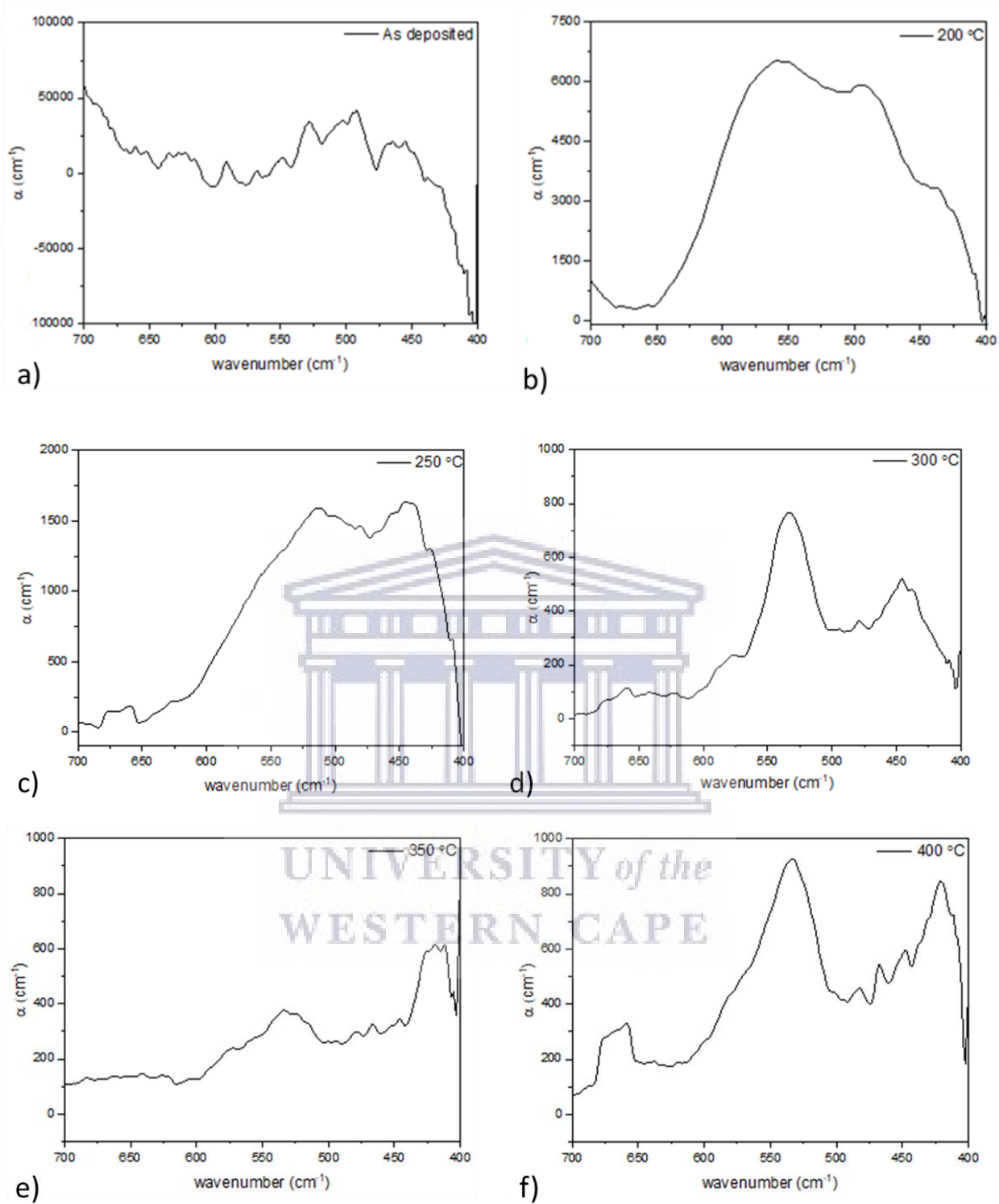


Figure 3.12: Overall FTIR spectra for as-deposited and annealed Sn_xO_y samples from 200 - 400 °C.

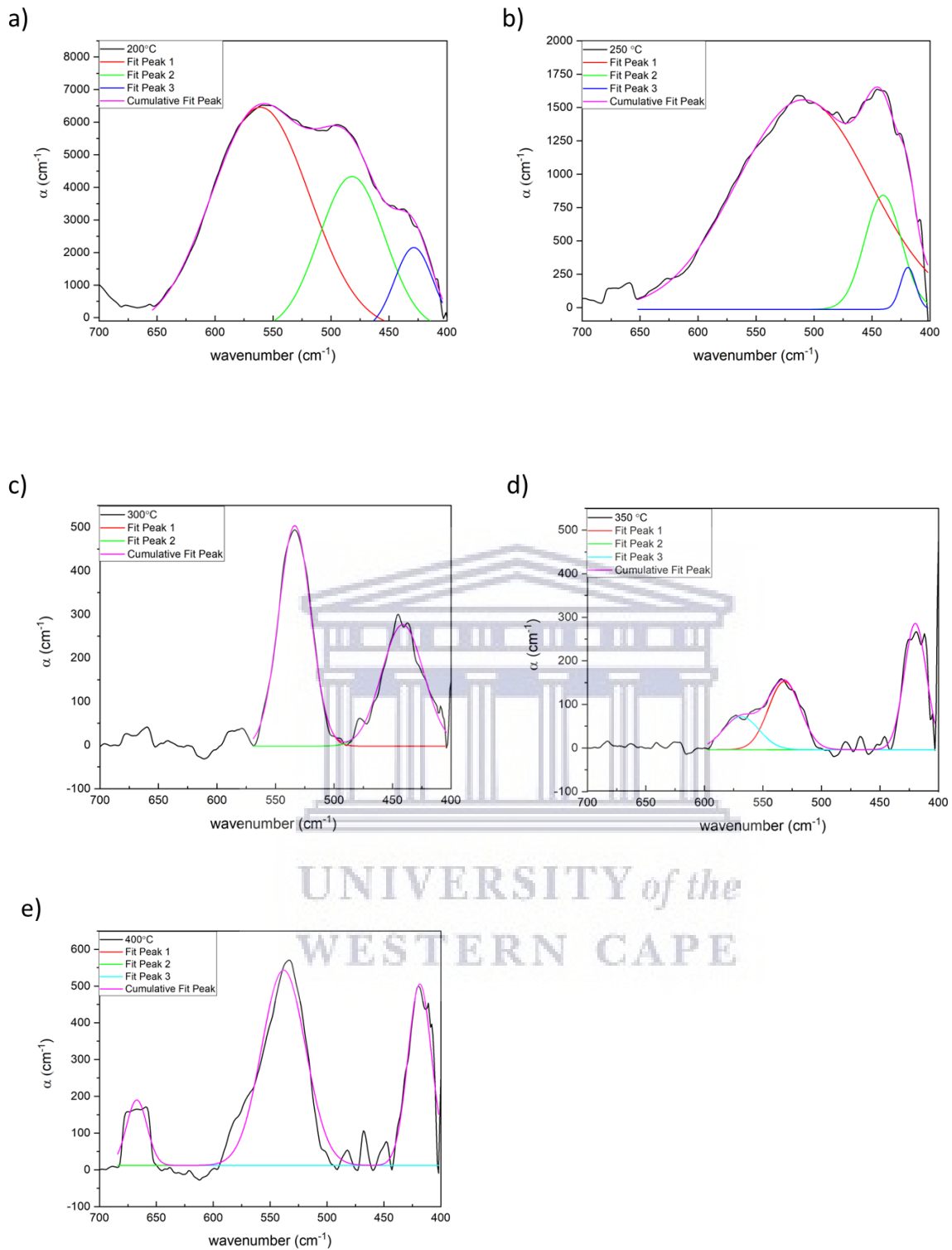


Figure 3.13: Baseline corrected Gaussian fits for samples annealed from 200 - 400 °C.

3.2.3.2 Rutherford Backscattering Spectroscopy

Characteristic properties such as the elemental composition, stoichiometry and thickness regarding Sn_xO_y thin films were all studied using the RBS technique. Figure 3.14 displays the RBS results obtained for both as-deposited and thermally oxidized Sn thin films annealed at temperatures ranging from 200 - 400 °C deposited on a Si (100) substrate. The SIMNRA *Simplex* code was employed to fit the simulated results to the experimental data in order to provide information pertaining to the stoichiometry and areal concentration. Adeoye et al. has stated that “a previous study has shown that composition of compound semiconductors has a strong influence on their properties” [3.2]. It is for this reason that meticulous management of composition and accurate examination of elements constituting these thin films are fundamental in producing excellent quality and chemical stable thin films [3.2].

In Figure 3.15, the stoichiometry of the film was described by the ratio of O/Sn atoms, and thickness is given as a function of annealing temperatures. Table 3.5, summarises all simulated fitting data outcomes concerning the composition, concentration, film thickness and surface roughness of all samples. Sn_xO_y atomic film thicknesses expressed in terms of atoms cm^{-2} were converted into geometrical film thickness (nm) by using the bulk density (6.95 g cm^{-3}) and molecular mass ($150.71 \text{ g mol}^{-1}$) of SnO_2 [3.34]. In a similar way, the roughness was determined by converting the FWHM of the thickness distribution expressed in 10^{15} atoms cm^{-2} into units of nanometres (nm).

By reviewing the RBS spectra in Figure 3.14, the most forthcoming observation is that of an improvement in O concentration within the film introduced by augmented annealing temperatures. This is verified by the compositional results in Table 3.5, and the atomic O/Sn

percentage shown in Figure 3.15. The second most prominent feature displayed in Figure 3.14, is the broadening of the Sn peak observed from the as-deposited sample - 400 °C. Kabir et al. has stated that this broadening of the Sn peak is suggestive of the diffusion of Sn atoms towards the Si substrate. For O atoms, however, it proves to be quite problematic to distinguish whether the O atoms diffuse through the Si substrate and those which combine with the Sn metal to form a Sn metal oxide. This is due to the multi-diffusion occurrence from the oxygen sublattice [3.24].

By now it is recognized that a complete stoichiometric SnO₂ crystal material having an O/Sn ratio of 2:1 will display properties of an insulator having a large amount of resistance. On the other hand the non-stoichiometric form of SnO₂ behaves like a semiconductor. By reviewing Figure 3.15, the O/Sn ratio obtains values of 0.110, 0.302, 0.602, 0.640 and 0.702 for films ranging from 200 - 400 °C. The optimum value obtained for O/Sn ratio was that of 0.702 at 400 °C. This value suggests that the oxidized Sn_xO_y film is composed of a non-stoichiometric crystal nature. Furthermore, the fact that O/Sn atomic ratio obtained is more closely related to a 1:1 ratio rather than a 2:1 ratio signifies that either majority of the metal oxide film is composed of SnO molecules rather than SnO₂ molecules, and or, that only a fraction of the film was converted into a tin metal oxide while the remainder remained in its Sn phase. This is in alignment with what was mentioned in the phase transitions section, which stated that oxidation within the films was incomplete.

In the morphological section 3.2.1, a similar study regarding the composition of Sn_xO_y was studied. By comparing the EDS results to those established by RBS, the values given via the RBS technique proves to be the most reliable quantitative study since the quality of the EDS quantitative analysis was hindered by the amount of oxygen and carbon impurities within the

system. On the other hand, as a qualitative study both EDS and RBS show a relative increase in O/Sn ratio as a function of increased annealing temperatures.

Coupled with the increase in O concentration within Sn_xO_y films, an increase in film thickness is displayed in Figure 3.15. In the morphological section 3.2.1, a measure of thickness as function of annealing temperatures was also conveyed in Figure 3.7, however, the results displayed by the Dektak presents different outcomes with respect to those listed in table 3.5 and displayed in Figure 3.15 given by RBS. The main reason that can be accountable for this variation in thickness results is that the Dektak profilometer 's stylus measured the average thickness of the film by possessing a longitudinal trajectory across the films surface until reaching a step down onto the substrate, thus, providing a change in height from the substrate to the films surface. On the other hand, the RBS thickness results were obtained by an in-situ technique located at one spot where the depth of the film was studied, and was able to provide a means of determining the thickness. Granted, that if the films had displayed a more homogeneous smooth and level surface, the variation between the RBS and dektak profilometer would have been closer in agreement to one another.

Once more, in Figure 3.15 the results implies that the process of the downward diffusion of O atoms and the upward diffusion of Sn atoms had occurred and subsequently caused an expansion in crystal lattice volume of a body centred tetragonal Sn unit cell of 53.18 \AA^3 morphing into Sn metal oxide crystal lattices i.e. 69.63 \AA^3 for SnO and 70.75 \AA^3 for SnO_2 [3.24, 3.32, 3.22]. In addition to the increased thickness of the film, it is worth noting that although the atomic concentration of O present in the films increases as a function of increasing temperature, the atomic ratio of O/Sn is a telling indication that the desired

stoichiometry of a non - stoichiometric SnO₂ was not attained since a 2:1 of O to Sn atoms was not evident and therefore, the results are suggestive of a polycrystalline Sn_xO_y thin film.

Table 3.5: Simulated RBS ion beam depth analysis of Sn_xO_y thin film samples.

Sample	Stoichiometry		Thickness		Roughness	
	Element	Concentration	10 ¹⁵ atoms.cm ⁻²	nm	1 ¹⁵ atoms.cm ⁻²	nm
400 °C	Sn	0.587	206	74.178	450	16.2
	O	0.413				
350 °C	Sn	0.610	205	73.818	380	13.7
	O	0.390				
300 °C	Sn	0.624	213	76.698	400	14.4
	O	0.376				
250 °C	Sn	0.768	164	59.054	300	10.8
	O	0.232				
200 °C	Sn	0.901	125.206	45.085	4.007	1.4
	O	0.099				
As-deposited	Sn	1	115.62	41.633	3	1.1

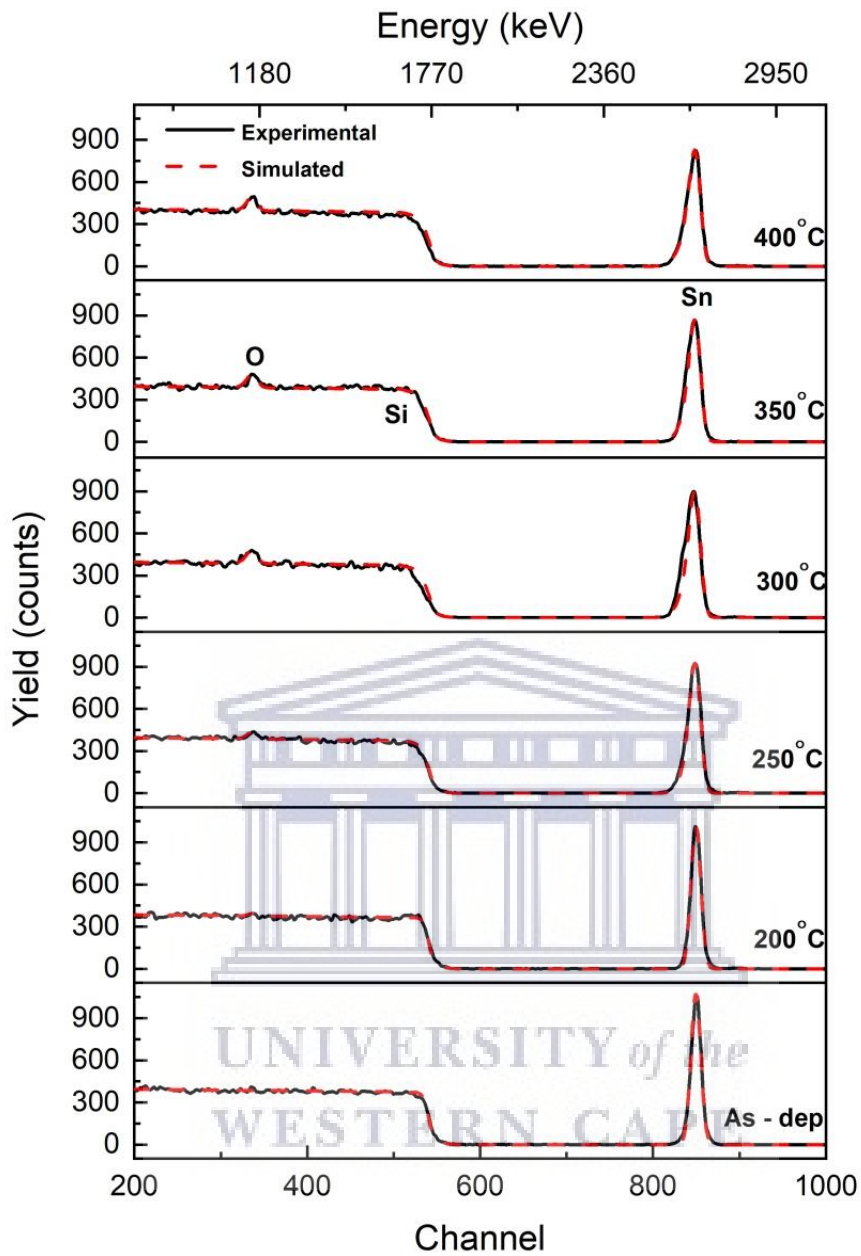


Figure 3.14: RBS spectra for as-deposited and annealed Sn_xO_y samples from 200 - 400 °C.

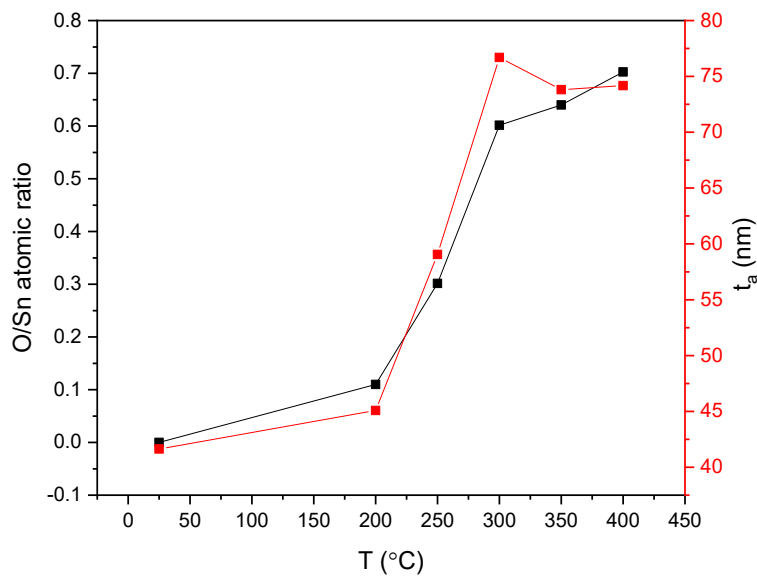


Figure 3.15: Atomic O/Sn ratio and with film thickness evolution as a function of annealing temperature.

3.2.4 Optical Properties

Interest in manufacturing novel optical materials is an ever growing occurrence in the research fields and industry [3.14]. Vital components in the industry of optics are thin films. Thin films are applied as coatings on eyeglasses, in solar cells and other electronic devices [3.36]. Therefore, optical properties of such films are required. Factors which influence optical properties of films are composition, thickness, surface morphology, conductivity and impurity centres [3.17]. High performance UV-Vis instruments are generally implemented for the characterisation of solid samples [3.44, 3.45]. Absorption spectroscopy is a non-destructive technique utilized to examine the optical properties of thin films [3.36, 3.17]. Absorption in a material can be associated with the photo-excitation of electrons from the valence band to the conduction band of the material [3.30]. As previously mentioned in

section 2.3.4, optical transmittance may be expressed in terms of absorption as shown in equation 2.4.1. The optical transmittance of Sn_xO_y thin films formed on FTO substrates under annealing conditions from 200 - 400 °C is depicted in Figure 3.16. In this instance, FTO films coated on glass substrates were selected to study the optical characterisation of thermally oxidized metallic Sn films due to its high transmission values of about 89.50% as opposed to the highly opaque crystalline Si (100) substrates in the visible region.

Optical transmittance of oxidized metallic Sn thin films produced at various temperatures were investigated to confirm whether the resultant Sn_xO_y thin films were able to meet the transmission requirements for an ETL in conjunction to whether the films had oxidized fully. In Figure 3.16 at first glance, it is quite evident that increasing the annealing temperature of the Sn_xO_y thin film samples had a positive influence on the average transmittance values. For samples 200 - 400 °C average transmission had transformed from around 7, 42, 51, 64.5, and 64% have been obtained accordingly, within the region of 550 - 900 nm (visible - near infrared region). By comparatively reviewing the transmittance of the film with respect to increasing annealing temperatures, the increase in transmission values suggests that the films annealed at higher temperatures like 350 and 400 °C possessed higher concentrations of O than that of films annealed ≤ 300 °C. Therefore, indicating that the transformation of pure metallic Sn to Sn_xO_y had progressed. Previous studies performed by Liang et al. showed that p-type SnO thin films were able to achieve average transmittance value of about 85%, while Erken et al. proved that n-type SnO_2 were able to obtain a 90% average transmittance [3.29, 3.16]. The drop in transmittance within a film may be affected by a number of parameters. In this particular case, one of the most influential factors may be that the films were not completely oxidized. Unfortunately, this cannot be pin-pointed with full confidence as the main reason to why the average transmittance of the films obtained in this study values are

lower than those provided by literature. However, this statement does fall in line with what was proposed in the phase transition section (section 3.3) and the composition section (section 3.4), where metallic Sn films were deposited on Si (100) substrates and was oxidized under the exact same conditions as Sn oxidized films placed upon FTO substrates.

Furthermore, a radical decrease or discontinuity in transmission for all samples may then be observed within the range 300 - 500 nm. Such discontinuities in transmittance are formally referred to as the absorption edge of a material and in this study manifests at about 300 nm for all films. This is an indication of the minimum energy required to free electrons from the subshells within constituent atoms residing within Sn_xO_y film structure. Furthermore, the number of interference fringes shown in all Sn_xO_y transmittance spectra is related to the thickness of the thin film [3.47.]. It is therefore evident that the increase in temperature results in the increase of the film thickness, in agreement with the RBS and profilometry measurements.

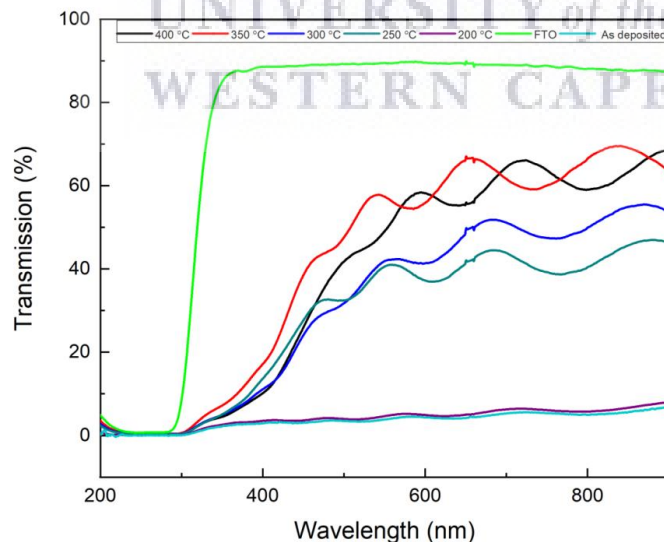


Figure 3.16: Transmission spectra for Sn thin films annealed 200 - 400 °C.

Tauc et al. provided a technique in which the band gap of a semiconductor may be determined by means of utilizing its optical absorbance [3.49]. This method was then later advanced through Davis and Mott's work on amorphous semiconductors, where the method proposes that the optical absorption strength is dependent on the difference between the photon energy and the band gap in the following manner:

$$(\alpha h\nu)^{1/n} = A (h\nu - E_g) \quad (\text{Eq. 3.35})$$

Where h is Planck's constant, ν is the photon's frequency, α is the absorption coefficient, E_g is the band gap, and A is a proportionality constant. The nature of the electronic transition is given by the exponent n , such that:

$n = 1/2$; for direct allowed transitions,

$n = 3/2$; for direct forbidden transitions,

$n = 2$; for indirect allowed transitions,

$n = 3$; for indirect forbidden transitions.

General Tauc analysis entails plotting the $(\alpha h\nu)^{1/n}$ versus $(h\nu)$ in order to compare which fit best suites the transition type. These type of plots are called Tauc plots, where the band gap of a given semiconductor may be extrapolated [3.49].

Figure 3.17 displays the Tauc plots for a direct allowed transition using optical absorbance Sn_xO_y thin films deposited on FTO oxidized from 200 - 400 °C. By evaluation of every plot given in Figure 3.17, the obtained band gap values for films annealed from 200 - 400 °C are 3.83, 3.78, 3.77, 3.75 and 3.73 eV, respectively. The shift towards decreasing band gap energy values as a function of increasing oxidation temperature from 200 - 400 °C may be linked to the increase in amplitude of the atomic vibrations caused by the increase of thermal

energy. This behaviour leads to an expansion in atomic spacing, which in turn weakens the bonds within the semiconducting crystal lattice. As a result, less energy is required to break these bonds. Hence, the promotion of electrons from the VB to the CB necessitates less energy and therefore the band gap size decreases [3.5]. Applying tensile and compressive stress causes direct modulation of the interatomic spacing and hence alters the band gap. The relation between the energy band gap E_g as a function of temperature T is expressed as follows:

$$E_g(T) = E_g(0) - \frac{\alpha T^2}{T + \beta} \quad (\text{Eq. 3.36})$$

Where $E_g(0)$ is the band gap value at 0 K, and α and β are material constant commonly determined by a best fit to experimental data [3.5, 3.48].

These experimental band gap values are highly comparable bulk SnO₂ band gap of 3.6 - 4.0 eV as proposed by literature.

The overall range in which the band gap for every film obtained falls slightly within a higher range than that of the bulk SnO (2.5 - 3.4 eV), but is well within the range of the bulk SnO₂ (3.6 - 4.0 eV). By now, it is quite evident that a polycrystalline film had developed as an outcome of the experimental procedures delineated by this study. Therefore, it is clear that a completely pure metal oxide thin film consisting of only SnO or SnO₂ had not formed, but rather a mix of both these phases coexisting in one film (see section 3.2.2). With that said, structural defects and impurities contributed by these mixed phases may also have an impact on the obtained band gap values for films oxidized from 200 - 400 °C. Furthermore, as previously stated, the inferior transparency (64.5%) compared to that obtained by literature indicates that Sn phases are still present within the polycrystalline Sn_xO_y thin film since they had not fully oxidized [3.43].

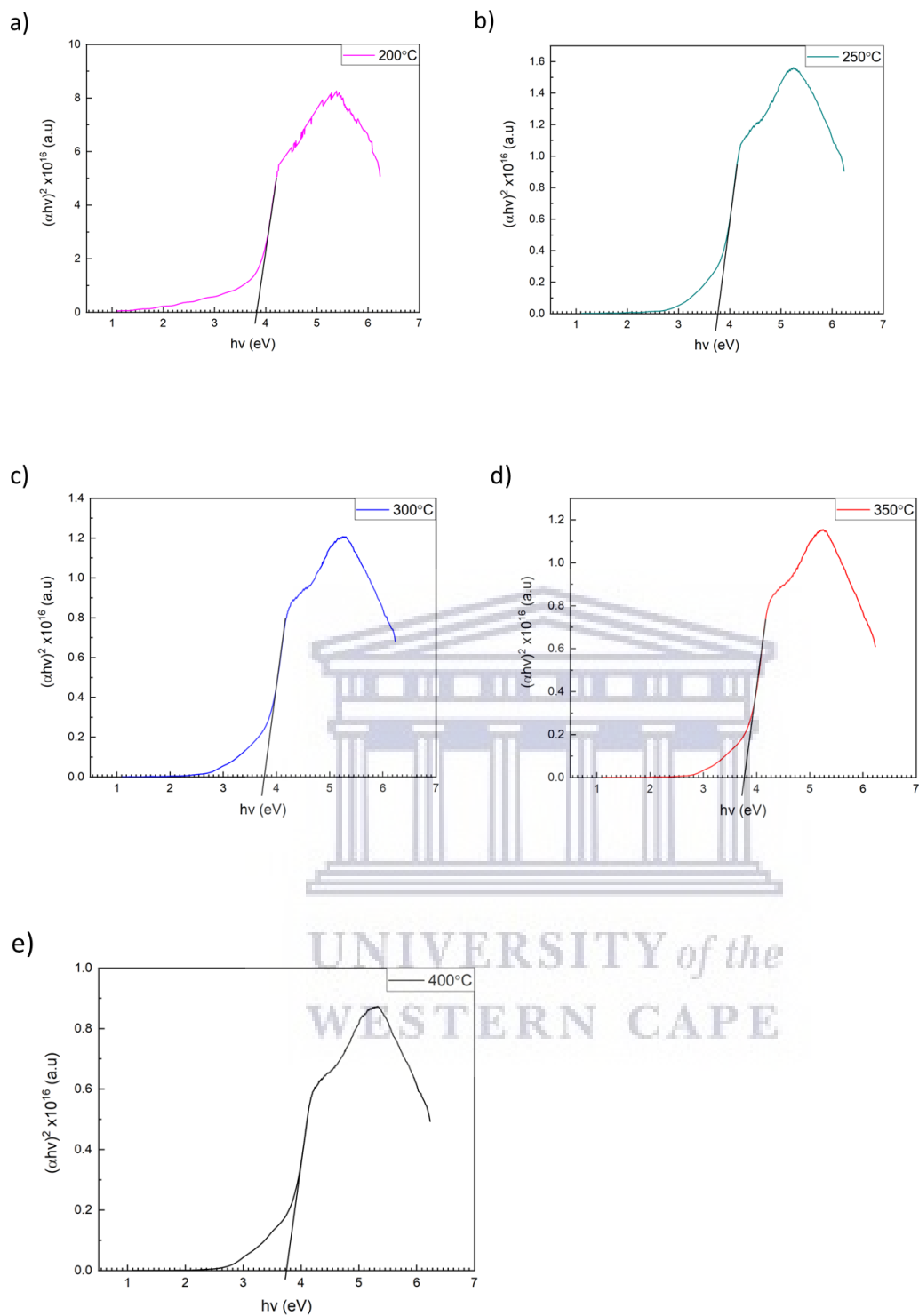


Figure 3.17: (a) - (e) Tauc plots for Sn_xO_y thin films oxidized from 200 - 400°C, respectively.

3.3 Overview and Discussion

In order to fully summarise and conclude on the experimental results and analysis regarding Sn_xO_y films, all characteristic aspects such as the morphological, crystalline, compositional and optical properties associated with respect to every sample needs to be overviewed. In this study metallic Sn films were deposited on both Si (100) and FTO substrates by means of thermal evaporation of 10 mg 99.9% Sn powder, where they were subsequently oxidized to produce Sn_xO_y films.

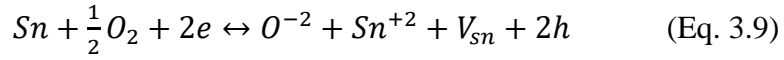
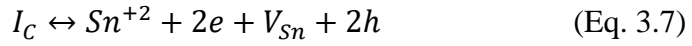
Enlightenment with regards to the diffusion process that took place in this study was brought on by reviewing all characteristic aspects of the oxidised Sn_xO_y . Such properties were provided by the employment of analytical techniques such as the SEM, the dektak profilometer, XRD, FTIR, RBS and finally, the UV-Vis instrument. By now it is known that a number of factors influences conductance within a film like microstructure, crystallinity and stoichiometry. In the morphological section of this study, the topographical BSE images displayed in Figure 3.1 and 3.5, both suggested morphological changes had progressed as a function of annealing temperatures. These microstructural surface changes were then related to the diffusion of O adatoms along the Sn grain boundaries situated upon substrates. Furthermore, the overall evolution of the microstructural surface behaviour of Sn films after being annealed from 200 - 400 °C was suggestive of the Coble creep diffusion mechanism. The phase transition section conveyed information pertaining to the crystal phases present within every sample. It was found that at 300 °C, that the annealed film was composed of multiple crystalline phases such as Sn, SnO and SnO_2 . This aligned with what was proposed in the morphological section that oxidation was initiated at 300 °C. Hence, the formation of ‘ellipsoid-like’ and small ‘spherical-like’ grains, indicating tensile and compressive stresses was due to the multitude of tin oxide phases co-existing in one film. Overall, it was found in

section 3.2.2 that majority of the oxidised crystal phases associated with Sn_xO_y formation was that of SnO rather than SnO_2 . In the compositional section characteristic vibrational properties were studied combined with in-situ depth analysis performed by RBS. In section 3.2.4, the stoichiometry of the Sn_xO_y films was given by the atomic ratio of O/Sn. The film which possessed the highest amount of O concentration was the film annealed at 400 °C, where the stoichiometry of the film was 0.702. This indicated that majority of the film was composed of SnO molecules, and or, that the film had not completely oxidized.

Lastly, the highest average transmission for films was that of approximately 65% for films annealed at 350 and 400 °C. Conclusive to the results listed mainly from the phase transition section and the stoichiometry given by RBS, it can be deduced that the films produced in this study was of a multiphase polycrystalline structure, where majority of the Sn_xO_y phases in the films was majority of that belonging SnO . However, the obtained band gap values displayed in Figure 3.17 for Sn_xO_y thin films annealed between 200 - 400 °C accordingly are indicative that the formation of defects and SnO_2 phase was enough to influence these values since they are not with the range for an SnO band gap of 2.5 - 3.4 eV but rather in SnO_2 range (3.6 - 4.0 eV). By analysing all results obtained by this study, it is clear that a polycrystalline Sn_xO_y thin film consisting of both SnO , SnO_2 and Sn phases were formed.

However, since the majority of the polycrystalline structure are composed of SnO phases rather than SnO_2 , the rest of the discussion will be based on a p-type SnO film formation during oxidation. Non-stoichiometric SnO materials are p-type semiconductors. According to Boggs et al., since SnO is a p-type semiconductor with cation vacancies (V_{Sn}), the semiconductor model and the interface equilibrium equations for p-type non-stoichiometric crystals may be expressed as follows:





Where V_{Sn} is a tin cation vacancy, h is a positive hole, and I_C represents a stoichiometric crystal [3.10]. According to Eq. 3.6, the initiating stages of oxidation begins when Sn cations (Sn^{+2}) are generated at the metal/oxide interface and diffuse towards the oxide/gas interface via a hopping gradient mechanism i.e. by exchanging places with the V_{Sn} (see Eq. 3.7) [3.10,3.37]. Eq. 3.8 shows how oxygen reacts with tin and removes two electrons from Sn at the oxide/gas interface. Therefore, leaving $2h$ and a V_{Sn} within the crystal lattice (see Eq. 3.9). The positively charged holes then migrate through the CB, where mass transfer serves as a result of tin vacancies [3.37].

Since the growth exhibited by a p-type semiconductor such as SnO emanates from the oxide-gas interface; this implies that Sn^{+2} diffuse faster than oxygen ions O^{-2} within the metal oxide. Therefore, the diffusion flux of Sn^{+2} given by $J_{Sn^{+2}}$, is greater than the the diffusion flux of O^{-2} denoted by $J_{O^{-2}}$ ($J_{Sn^{+2}} > J_{O^{-2}}$). According to Perez et al., in such a metal oxide growth conditions where $J_{Sn^{+2}} > J_{O^{-2}}$, the stress concentration experienced by the film is eventually relieved, and therefore, the oxide layers remains attached to the metal surface protecting it from further oxidation [3.37].

3.4 Conclusion

In this chapter the experimental results and analysis of thermally oxidized metallic Sn thin films placed under conditions of annealing from 300 - 400 °C in atmosphere were discussed. For the sample annealed at 200 °C, it was evident that little to no oxidation had taken place. This deduction was made since the morphology of the films showed no change in comparison to the as-deposited film, exhibited strong Sn peaks belonging to the Sn body centred tetragonal (I41/amd) crystal structure, obtained a stoichiometry of 0.110 for O/Sn through RBS, and finally the transmittance was 7%. These results were expected since the boiling point of Sn is at 232 °C, and therefore influencing the amount of oxygen atoms from penetrating the film surface. At 250 °C, it was clear that no some morphological changes were found for the Sn_xO_y film deposited on the FTO substrate, while for the film deposited on the Si (100) substrate displayed none. Crystal properties still showed similar behaviour as to the film deposited at 200 °C, however the intensity of these peaks had decreased. The stoichiometry at this point was 0.302 for O/Sn, and transmittance increased to 42%. This signalled the onset of oxidation. The first signs of pure tin oxide formation manifested in the film annealed at 300 °C since XRD crystal analysis displayed phases which were fitting to the formation of SnO and SnO₂ crystals. In the films from 300 - 400 °C signs of coble creep mechanism had formed. This movement is linked to the recrystallization through the penetration of oxygen adatoms within the films lattice, and as a consequence tensile and compressive stresses are experienced by the bonds the within films. Furthermore, the films annealed within this temperature range vibrational bands such as O – Sn – O, Sn – OH and Sn – O – Sn FWHM values had decreased and appeared more pronounced as a function of increasing temperature. This concurred that recrystallization within the film had taken place

verifies that SnO and SnO₂ molecules had indeed been formed. The Stoichiometry as well as film thickness had increased and was linked to the volume lattice expansion associated with the transformation from Sn to SnO and SnO₂. The highest transmittance was that of approximately 65% which falls short of what was proposed by literature which indicated that the film had not oxidized fully. With that said, it is clear that within this study that the conditions of the experiment were successful in producing a tin oxide thin film. However, these films were of a polycrystalline nature and hence a monocrystalline SnO₂ thin film was not fabricated.



References

- 3.1 Abdullah, N., Ismail, N. M., and Nuruzzaman, D. M. (2018). Preparation of tin oxide (SnO_2) thin films using thermal oxidation. In: IOP Conference Series: Materials Science and Engineering, 319(2018), 012022(1 - 6).
- 3.2 Adeoye, E. A., Ajenifuja, E., Taleatu, B.A., Fasasi, A.Y. (2015). Rutherford Backscattering Spectrometry Analysis and Structural Properties of $\text{Zn}_x\text{Pb}_{1-x}\text{S}$ Thin Films Deposited by Chemical Spray Pyrolysis. Hindawi Publishing Corporation. Journal of Materials, 2015(215210), 1 - 8.
- 3.3 Ali, S.M., Hussain, S.T., Bakar, S.A., Muhammad, J., Rehman, N. (2013). Effect of doping on the Structural and Optical Properties of SnO_2 Thin Films fabricated by Aerosol Assisted Chemical Vapor Deposition. Journal of Physics, 493(012013), 1 - 10.
- 3.4 Andersson, T. (1982). The initial growth of vapour deposited gold films. Gold Bulletin, 15(1), 7 - 18.
- 3.5 Anon., (2020). Carriers - Temperature Dependence Explained. [online] Ece.utep.edu. Available at: <http://www.ece.utep.edu/courses/ee3329/ee3329/Studyguide/ToC/Fundamentals/Carriers/explain.html> [Accessed 15 November 2020].
- 3.6 Asgarya, S., Hantehzadeh, M. R. and Ghoranneviss, M. (2017). Temperature Dependence of Copper Diffusion in Different Thickness Amorphous Tungsten/Tungsten Nitride Layer. Physics of Metals and Metallography, 118(11), 1191 - 1201.

- 3.7 Babar, A.R., Shindea, S.S., Moholkar, A.V., Rajpure, K.Y. (2010). Electrical and dielectric properties of co-precipitated nanocrystalline tin oxide. *Journal of Alloys and Compounds*, 505(2010), 743 - 749.
- 3.8 Barreira, E., Pedrini, L., Boratto, M. and Scalvi, L. (2020). A dynamic time-temperature-dependent process for thermal oxidation of Sn leading to SnO_x thin films: Impedance spectroscopy study. *International Journal of Modern Physics B*, 34(19), 2050184(1 - 13).
- 3.9 Birks, N., Meier, G. and Pettit, F. (2009). Oxidation of pure metals. In: Birks, N., Meier, G. and Pettit, F. 2nd Ed. *Introduction to the High –Temperature Oxidation of Metals*. New York: Cambridge University Press, 75 - 99.
- 3.10 Boggs, W. E., Trozzo, P. S., Pellissier, G. E. (1961). The Oxidation of Tin: III. The Mechanisms of Oxidation of Pure Tin and Their Dependence on Time and Oxygen Pressure. *Journal of The Electrochemical Society*, Volume 108(2), 13 - 24.
- 3.11 Boulainine, D., Kabir, A., Bouanane, I., Boudjema, B. and Schmerber, G. (2016). Oxidation Temperature Dependence of the Structural, Optical and Electrical Properties of SnO₂ Thin Films. *Journal of Electronic Materials*, 45(8), 4357 - 4363.
- 3.12 Çakmak, H., Çetinkara, H., Kahraman, S., Bayansal, F., Tepe, M., Güder, H. and Çipiloğlu, M. (2012). Effects of thermal oxidation temperature on vacuum evaporated tin dioxide film. *Superlattices and Microstructures*, 51(3), 421 - 429.
- 3.13 Chung, Y., Hubenko, A., Meyering, L., Schade, M., Zimmer, J. and Remmel, T. (1997). Morphology and phase of tin oxide thin films during their growth from the metallic tin. *Journal of Vacuum Science & Technology A: Vacuum, Surfaces, and Films*, 15(3), 1108 - 1112.

- 3.14 Desforges, J., Robichaud, L., Gauvin, S. (2017). Determination of optical properties of thin films from Ketteler – Helmholtz dispersion relations: Application to the case of ultraviolet irradiated zirconium oxide. *Advances in Materials Science and Engineering*, 2017(8285230), 1 - 9.
- 3.15 Doitpoms.ac.uk. (2020). Doitpoms - TLP Library Creep Deformation Of Metals - Creep Mechanisms. [online] University of Cambridge. Available at: <https://www.doitpoms.ac.uk/tlplib/creep/mechanisms.php> [Accessed 21 October 2020].
- 3.16 Erken, O., Ozkendir, O., Gunes, M., Harputlu, E., Ulutas, C. and Gumus, C. (2019). A study of the electronic and physical properties of SnO₂ thin films as a function of substrate temperature. *Ceramics International*, 45(15), 19086 - 19092.
- 3.17 Felcia, E., Gnanam, K. (2017). Synthesis and Characterization of SnO₂ Nanoparticle by Microwave Assisted Hydrothermal Method. In: National Conference on Current Advancements in Physics. Tamilnadu: IOSR Journal of Applied Physics, 98 - 104.
- 3.18 Floro, J., Hearne, S., Hunter, J., Kotula, P., Chason, E., Seel, S. and Thompson, C. (2001). The dynamic competition between stress generation and relaxation mechanisms during coalescence of Volmer-Weber thin films. *Journal of Applied Physics*, 89(9), 4886 - 4897.
- 3.19 Guo, W., Fu, L., Zhang, Y., Zhang, K., Liang, L., Liu, Z., Cao, H. and Pan, X. (2010). Microstructure, optical, and electrical properties of p-type SnO thin films. *Applied Physics Letters*, 96(4), 042113(1 - 3).
- 3.20 Hajiabadi, M. G., Zamanian, M. and Souri, D. (2019). Williamson-Hall analysis in evaluation of lattice strain and the density of lattice dislocation for nanometer scaled ZnSe and ZnSe:Cu particles. *Ceramics International*, 45(11), 14084 - 14089.

- 3.21 Hazzledine, P. and Schneibel, J. (1993). Theory of coble creep for irregular grain structures. *Acta Metallurgica et Materialia*, 41(4), 1253 - 1262.
- 3.22 Hicks, D., Mehl, M., Gossett, E., Toher, C., Levy, O., Hanson, R., Hart, G., Curtarolo, S. (2019). The AFLOW Library of Crystallographic Prototypes: Part 2. *Computational Materials Science*, 161(2018), S(1 - 1011).
- 3.23 Jiang, Y., Xu, C. and Lan, G. (2013). First-principles thermodynamics of metal-oxide surfaces and interfaces: A case study review. *Transactions of Nonferrous Metals Society of China*, 23(1), 180 - 192.
- 3.24 Kabir, A., Boulainine, D., Bouanane, I., Schmerber, G., Boudjema, B. (2017). Physical properties of SnO₂ thin films prepared by isothermal oxidation of vacuum evaporated Sn. *Journal of Materials Science: Materials in Electronics*, 28(3), 2481 - 2486.
- 3.25 Khorsand Zak, A., Abd. Majid, W. H., Abrishami, M. E. and Yousefi, R. (2011). X-ray analysis of ZnO nanoparticles by Williamson-Hall and size-strain plot methods. *Solid State Sciences*, 13(1), 251 - 256.
- 3.26 Kitabayashi, S. and Koga, N. (2015). Thermal Decomposition of Tin(II) Oxyhydroxide and Subsequent Oxidation in Air: Kinetic Deconvolution of Overlapping Heterogeneous Processes. *The Journal of Physical Chemistry C*, 119(28), 16188 - 16199.
- 3.27 Ko, Y., Kim, Y. R., Jang, H., Lee, C., Kang, M. and Jun, Y. (2017). Electrodeposition of SnO₂ on FTO and its Application in Planar Heterojunction Perovskite Solar Cells as an Electron Transport Layer. *Nanoscale Research Letters*, 12(498), 1 - 7.

- 3.28 Laghrib, S., Amardjia-Adnani, H., Abdi, D., Pelletier, J. and Lakhdari, D. (2010). Thermal oxidation of tin layers and study of the effect of their annealings on their structural and electrical properties. *Materials Science in Semiconductor Processing*, 13(5-6), 364 - 370.
- 3.29 Liang, L., Liu, Z., Cao, H. and Pan, X. (2010). Microstructural, Optical, and Electrical Properties of SnO Thin Films Prepared on Quartz via a Two-Step Method. *ACS Applied Materials & Interfaces*, 2(4), 1060 - 1065.
- 3.30 Magubane, S. (2018). Metal Assisted Chemically Etched Silicon Nanowires For Application In A Hybrid Solar Cell. M.Sc. University of the Western Cape (UWC).
- 3.31 Maruyama, K. (2008). Fundamental aspects of creep deformation and deformation mechanism map. In: Abe, F., Kern, T. and Viswanathan, R. 1st Ed. *Creep-Resistant Steels*. Cambridge: Woodhead, 265 - 278.
- 3.32 Mehl, M. J., Hicks, D., Toher, C., Levy, O., Hanson, R. M., Hart, G., Curtarolo, S. (2017). The AFLOW Library of Crystallographic Prototypes: Part 1. *Computational Materials Science*, 136(2017), S(1-828).
- 3.33 Morosanu, C.E. (1990). Nucleation and Growth of CVD Films. In: n.k.1st Ed. *Thin Films by Chemical Vapour Deposition*. Amsterdam: Elsevier, 163 - 176.
- 3.34 Newbury, D. E. and Ritchie, N. W. M. (2014). Performing elemental microanalysis with high accuracy and high precision by scanning electron microscopy/silicon drift detector energy-dispersive X-ray spectrometry (SEM/SDD-EDS). *Journal of Materials Science*, 50(2015), 493 - 518.

- 3.35 Niinisto, H., Niinisto, L. (1994). Controlled growth of tin dioxide thin films by atomic layer epitaxy. *Thin Solid Films*, 249(1994), 144 - 149.
- 3.36 Paint and Coating Industry. (2014). Thin-Film Analysis Using UV-Vis Spectrophotometry. [online] ePublishing. Available at: <https://www.pcimag.com/articles/99448-thin-film-analysis-using-uv-vis-spectrophotometry> [Accessed 11 October 2020]
- 3.37 Perez, N. (2005) High-temperature Corrosion. In: Perez, N. 1st Ed. *Electrochemistry And Corrosion Science*. Boston: Kluwer Academic Publishers, 301 - 338.
- 3.38 Priya, S.M., Geetha, A., Ramamurthi, K. (2016). Structural, morphological and optical properties of tin oxide nanoparticles synthesized by sol-gel method adding hydrochloric acid. *Journal of Sol-Gel Science and Technology*, 78(2), 365 - 372.
- 3.39 Sagadevan, S., Podder, J. (2015). Optical and Electrical Properties of Nanocrystalline SnO₂ Thin Films Synthesized by Chemical Bath Deposition Method. *Soft Nanoscience Letters*, 5(2015), 55 - 64.
- 3.40 Saleh, A. M, Bakr, N. A., Khodair, Z. T. (2018). Effect of oxygen flow rate on structural and optical properties of SnO₂ thin films prepared by apcvd technique. *Digest Journal of Nanomaterials and Biostructures*, 13(3), 603 - 608.
- 3.41 Saleha, S.A., Ibrahim, A.A., Mohamed, S.H.(2016). Structural and Optical Properties of Nanostructured Fe-Doped SnO₂. *Acta Physica Polonica*, 129(2016), 1220 - 1225.
- 3.42 Samourganidis, G., Nikolaou, P., Gkovosdis-Louvaris, A., Sakellis, E., Blana, I.M., Topoglidis, E. (2018). Hemin-Modified SnO₂ /Metglas Electrodes for the

- Simultaneous Electrochemical and Magnetoelastic Sensing of H₂O₂. *Coatings*, 8(284), 1 - 21.
- 3.43 Sefardjella, H., Boudjema, B., Kabir, A. and Schmerber, G. (2013). Characterization of SnO₂ obtained from the thermal oxidation of vacuum evaporated Sn thin films. *Journal of Physics and Chemistry of Solids*, 74(12), 1686 - 1689.
- 3.44 Sethi, R., Ahmad, S., Siddiqui, A. and Aziz, A. (2015). Structural, Optical and Electrical Properties of Tin Oxide Thin Films for Application as a Wide Band Gap Semiconductor. In: *AIP Conference Proceedings*. Longowal: American Institute of Physics, 030039(1 - 6).
- 3.45 Shimadzu Excellence in Science. (2020). UV-Vis Frequently Asked Questions - Solid Sample Transmission. [online] Shimadzu Scientific Instruments. Available at: <https://www.ssi.shimadzu.com/products/uv-vis-spectrophotometers/faqs/solid-sample-transmission.html> [Accessed 11 October 2020]
- 3.46 Sigma-Aldrich. (2020). IR Spectrum Table & Chart. [online] Merck. Available at: <http://www.sigmaaldrich.com/technical-documents/articles/biology/ir-spectrum-table.html> [Accessed 15 September 2020]
- 3.47 Tripathy, S. and Prabhakar Rao, T. (2015). The Influence of Annealing Temperature on Optical Properties of Tin Oxide (SnO₂) Thin Films Prepared by Thermal Evaporation Process. *International Journal of Science and Research (IJSR)*, 5(5), 591 - 596.
- 3.48 Van Zeghbroeck, B. (2011). Temperature Dependence Of The Energy Bandgap. [online] Ecee.colorado.edu. Available at: <https://ecee.colorado.edu/~bart/book/eband5.htm#:~:text=The%20energy%20bandgap>

[%20of%20semiconductors,to%20the%20increased%20thermal%20energy.](#) [Accessed 15 November 2020].

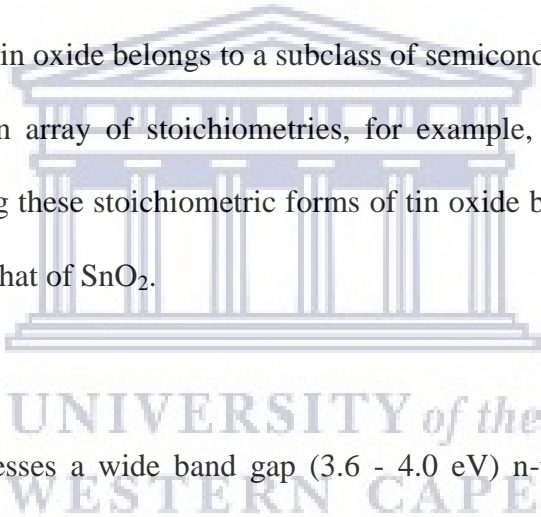
- 3.49 Viezbicke, B., Patel, S., Davis, B. and Birnie, D. (2015). Evaluation of the Tauc method for optical absorption edge determination: ZnO thin films as a model system. *physica status solidi (b)*, 252(8), 1700 - 1710.



CHAPTER 4

CONCLUSION AND FUTURE WORK

Semiconducting metal oxide materials are constituted of a wide variety of electrical properties ranging from wide band gap insulators to superconductors. Nano-scale metal oxide semiconductors are included in many research fields. This owed to their unique physical and chemical properties. Such physical and chemical properties are outlined by the shape and size of these nano-scaled semiconducting metal oxides, where it is then applied to an assortment of technological devices. Tin oxide belongs to a subclass of semiconducting materials that are capable of emerging in an array of stoichiometries, for example, SnO, SnO₂, Sn₂O₃ and Sn₃O₄ and so forth. Among these stoichiometric forms of tin oxide based materials, the most abundant form on earth is that of SnO₂.



SnO₂ nanostructures possesses a wide band gap (3.6 - 4.0 eV) n-type semiconductor and exists within a collection of sizes and geometries, such as nanorods, nanowires, nanotubes, nanospheres and nanosheets. In conjunction to its alluring optical, morphological, chemical and electrical properties, SnO₂ is also revered for being environmentally friendly and relatively inexpensive. Due to its inherent superior conductance and high optical transmittance features associated with nano-scaled SnO₂, it is only natural that they are employed as catalysis, gas-sensors, lithium batteries, and ETL's in perovskite solar cells.

In this study, oxidation of metallic Sn thin films were thermally induced in temperatures from 200 - 400 °C placed under ambient conditions with the aim of generating an SnO₂ film as a final product. As a result, Sn_xO_y films were subsequently produced where their morphological, crystalline, compositional and optical nature was investigated.

The morphological properties such as the microstructure of the resultant Sn_xO_y films surface were scrutinized by means of the scanning electron microscope (SEM). The x-ray diffractometer was employed to study the phase transitions and crystallinity of the films. Compositional analysis was brought on by the use of a Fourier transform infrared spectrophotometer which conveyed information pertaining to the vibrational properties of functional groups residing within the thin film sample. In addition, the Rutherford backscattering spectrophotometer (RBS) unveiled details with regards to depth analysis of oxidized films. Finally, optical properties such as transmission were examined through the use of the UV-visible spectrophotometer (UV-Vis).

The outcomes of the mentioned analytical techniques listed in chapter 2 used on oxidized Sn thin films were given in the experimental results section in chapter 3 and are summarized below:

- 200 °C - 250 °C: Little to no morphological microstructural surface changes were detected for Sn_xO_y compared to the as-deposited Sn thin film deposited Si (100). For the film annealed at 250 °C layered onto FTO substrates however, signs of Ostwald ripening and coalescence had emerged. This new grain formation was related to the onset signs of oxidation caused by stresses and strain experienced by the film on the FTO substrate. The XRD phase transitions study of films deposited on Si (100) substrates revealed strong crystalline Sn peaks with no sign of any pure tin oxide formation was present. Furthermore, compositional information displayed presence

the of broad Sn – O and Sn – OH vibrations which were suggestive of disorder in the bond vibrations ,while the stoichiometry given by RBS results were 0.110 and 0.302 for 200 and 250 °C, respectively, showed that oxygen concentration within the films at this stage was minimal. Additionally, optical transmittance enhanced from 7.5 - 44.5% within this temperature range. In addition, both crystalline and compositional properties revealed that strong carbon related impurities were constituents within films during analysis. Results within this temperature region suggested that minimal oxidation had taken place for metallic Sn thin film samples.

- 300 °C: At this stage migration and grain formation were evident for Si(100) samples. Once again this change in grain microstructure was indicative on the initiating stages of oxidation had commenced within films. XRD phase transformation results concurred with the deduction made in the morphological section by revealing a multi-phase polycrystalline film composed of both SnO and SnO₂ was formed. Majority of the phases residing within the polycrystalline Sn_xO_y films belonged to SnO formation instead of SnO₂. FTIR peaks belonging to O – Sn – O and Sn - OH vibrations had experienced a decrease in FWHM values, suggesting that a change in bond environment. This change in bond environments suggested that an improvement of bond order belonging to Sn_xO_y characteristic vibrations within the fingerprint region had taken place. The drastic increase in film thickness and roughness measurements given by the dektak profilometer and RBS coupled with the stoichiometric results of the atomic ratio of O/Sn revealed that an increase in oxygen concentration was present and a change from Sn to SnO and SnO₂ crystal unit cell volume had evolved.

- 350 - 400 °C: In this temperature range coalescence of Sn_xO_y surface microstructure was the most prominent feature. This kind of behaviour was indicative of relaxation of the films deposited on both substrates. At this point SnO and SnO_2 related phases were still present within the film. SnO_2 crystals orientated in the (101) diffraction peaks exhibited a decline in FWHM. Thus, illustrating a more crystalline phase formation at higher temperatures. In addition, at this stage of the oxidation process, resultant Sn_xO_y films showed no signs of any carbon related impurities. This was supported by the compositional results which displayed a decrease in concentration in band allocated to carbon related bonds. This revealed that purging of the films had taken place at elevated temperatures. An overall decrease in FWHM for Sn – OH, and O – Sn – O bonds was displayed once more, thus suggesting that more order of these bond vibrations were present. The emergence of the Sn – O – Sn also indicated that a bond related to a SnO molecule had formed. These results were analogous to the morphological section, since they indicate once more that SnO and SnO_2 bonds were present within the film. The highest stoichiometry related to the atomic ratio of O/Sn and film thickness at this point was that of 0.702 and 127.46 nm, accordingly, and was once again related to the unit cell volume expansion from Sn to SnO and SnO_2 . The final optical average transmittance was 65%.

Hence, it may be concluded that oxidation of metallic Sn films annealed 200 - 400 °C lead to a polycrystalline Sn_xO_y structure containing phases of both SnO and SnO_2 . However, in accordance with phase transitions and stoichiometric studies, it can be deduced that the dominant crystal phase formation of the film was that of SnO. Since SnO is a p-type semiconductor, it suggests that the diffusion flux within the oxidation process was dominated by that of cation Sn^{+2} diffusion resulting in oxide growth to mainly form at the

oxide/gas interface. With that said, analytical techniques reveal that the ideal film formed within this study was the film annealed at 400 °C.

Future optimization on the thermally induced oxidation of metallic Sn should include the use of atomic oxygen gas during sample processing. Inclusion of atomic oxygen may increase the probability of oxygen permeating through metallic Sn film surface. In addition, a further investigation of an isothermal oxidation study would reveal details pertaining to the growth kinetics governing the film whilst diffusion takes place.

Further insight revolving around the electrical conductance of the film by means of the Hall Effect instrument would be a great asset to this study.

